12-2012

Development of MEMS-based Corrosion Sensor

Feng Pan
University of Arkansas, Fayetteville

DEVELOPMENT OF MEMS-BASED CORROSION SENSOR

DEVELOPMENT OF MEMS-BASED CORROSION SENSOR

A dissertation submitted in partial fulfillment
of the requirements for the degree of
Doctor of Philosophy in Mechanical Engineering

Feng Pan
Shandong University
Bachelor of Science in Mechanical Engineering, 2005
University of Arkansas
Master of Science in Mechanical Engineering, 2010

December 2012
University of Arkansas

Abstract

This research is to develop a MEMS-based corrosion sensor, which is used for monitoring uniform, galvanic corrosion occurring in infrastructures such as buildings, bridges. The corrosion sensor is made up of the composite of micro/nano metal particles with elastomers. The mechanism of corrosion sensor is based on the mass transport of corrosive species through the sensor matrix. When the metal particles in the matrix corrode, the electrical resistivity of the material increases due to increasing particle resistances or reduction of conducting pathways. The corrosion rate can be monitored by detecting the resistivity change in sensing elements. The life span of the sensor can be ensured due to the barrier effect of polymeric matrix without losing sensor's sensitivity. The mechanism of corrosion sensor relies on the diffusion process, through which diffusive species penetrate into sensor and react with embedded particles to increase its resistivity. The diffusion process couples the chemical reaction which is described according to concentration rate gradient and collision theory with the diffusion which is usually governed by Fick's diffusion theory.

In this research project, three objectives are achieved:

1. Micro-fabrication approach to fabricate corrosion sensor in terms of developed DPPOST techniques
2. Study of the fundamental mechanism of diffusion through the metal particle PDMS polymer composites and diffusion coefficients
3. Characterization of the electric properties of the composites before and after etching oxide layers of metal particles. Two approaches have been posted to investigate the oxide removal: etching first and mixing first.

This dissertation is approved for recommendation
to the Graduate Council

Dissertation Director:

Dr. Adam Huang

Dissertation Committee:

Dr. Matthew Gordon

Dr. Douglas Spearot

Dr. Uchechukwu Wejinya

Dr. Linfeng Chen

Dissertation Duplication Release

I hereby authorize the University of Arkansas Libraries to duplicate this thesis when needed for research and/or scholarship.

Agreed _____
Feng Pan

Refused _____

Acknowledgements

I would like to thank my advisor Dr. Adam Huang for his support, advice and guidance throughout this work. I would also like to thank Drs. Linfeng Chen, Matthew Gordon, Douglas Spearot and Uchechukwu Wejinya for serving on my dissertation committee.

I would like to thank my research group mates John Lee, Mark Center and Matthew McMullen for their constructive discussion with me.

I would like to thank National Science Foundation (NSF) CMMI-0800718 (Sensor and Sensing Systems SSS-Dr. Shih C. Liu) for its partial financial support to this project in addition to the University of Arkansas start-up fund provided through my advisor.

I want to express my deepest appreciation to my parents. Five years, ups and downs, they are always standing on my side, supporting me, helping me, encouraging me. Even when I felled down, they convinced me to get over and never give up. Their endless love as the sunshine to the grass warms me up but without requiring anything repaid.

Table of Contents

List of Tables

List of Figures

Chapter 1 Corrosion, Inspection and Monitoring

1.1 Corrosion Impact

In the development of infrastructure construction, more and more attentions are paid to the prevention of corrosion failures that cause personal injuries, fatalities, unexpected turnoffs and environmental contamination. Corrosion can result in failures in plant infrastructure and machines that are expensive to maintain, repair and replace. A recent (2009) estimate of the worldwide direct cost of corrosion—for prevention as well as repair and replacement exceeded $1.8 trillion, which is approximate 3-4% of the gross domestic product (GDP) of industrialized countries [1]. Moreover, corrosion failures cause damages regarded to human safety and environment. Hereby several examples are described to demonstrate that how corrosion could result in severe devastations that cause human being fatality and property damage.

On, December 15, 1967 the "Silver Bridge', which is the U.S. highway 35 bridge connecting Point Pleasant West Virginia and Kanauga, Ohio collapsed into the Ohio River [2]. 31 vehicles on the bridge fell down to the river and 46 people were killed and 9 were seriously injured. Constructed in 1928, as the first aluminum painted (that is why it is called silver bridge) and the first eye-bar suspension bridge in U.S, it was designed with some unique engineering technologies such as high tension eye-bar chains, anchorage system, and "Rocker" towers. 11" pins were passed through eye-bars (2"X12") to link them together as a way of chain. The eye bar was made of high strength carbon steel occupying ultimate strength 105 kpsi and maximum working stress 50 kpsi, which allowed eye bars to share $4X10^6$ 1bf load of the bridge equally. The failure of the bridge was attributed to a cleavage fracture in the lower limb of eye-bar 330 at joint C13N, which was caused by a minute crack formed during casting of carbon steel. And this crack was growing over years due to stress corrosion cracking and corrosion fatigue. At the time

of construction, stress corrosion and corrosion fatigue were unknown defect factors and miniature crack was not cable of notice. During bridge's life span, there was no available technique to detect the fracture without dissembling eye-bars.

In 1985, Switzerland, a collapse of swimming pool, which had only been used for 13 years, caused a serious accident and 12 people were killed [3]. The roof was sustained by stainless steel rods in tension. A zipper-like crack was found from the broken section of these rods. The following investigation pointed out that these zipper-like damages were caused by chloride stress corrosion cracking (SCC) that resulted in weakness of the stainless steel unable to support the celling load. Chloride came from either its existence in concrete or water vapor present in the swimming pool. Although the stainless steel rods were passivated before installation, the gather of chloride on the surface of stainless steel could etch the passive film and pit on the surface and thus undermined the stainless steel rod. Corrosion occurs not only on infrastructure but also on transportation vehicles, such as airplanes and tankers.

The destructive power of corrosion is not only displayed on the field of infrastructures, but also on that of large vehicles, such as airplanes and ships.

In 1992, an EL AL 747 freighter crashed in Amsterdam. 4 people were killed on board and more than 50 on ground [4]. The crash of the airplane resulted from the loss of No. 3 and No. 4 engines from the wing. The reason for the number 3 engine separation was a breakage of the fuse pin. The pin was designed to break when an engine seizes in flight, producing a large amount of torque. Both of the engines were stripped off the right wing causing the Boeing 747-200 Freighter to crash as it maneuvered toward the airport. It is believed that the inboard fuse pin failed due to corrosion cracking and fatigue, causing the breakage of the outboard fuse pin which had been weakened by crack.

In 1999, a tanker, Erika, carrying 30,000 tons of heavy fuel oil broke adjacent to French coast off Brittany. 19,000 tons of oil were spilled, which was equal to the total amount of oil spilled worldwide in 1998. The leakage of oil cause huge disaster of regional environment. The Brittany beach was contaminated and the tourism dropped down stunningly. Thousands of millions of fishes, oysters and crabs had been killed in the devastation. The corrosion problem had been apparent on the Erika since at least 1994, with details available to port state control authorities and potential charterers. In addition, there were numerous deficiencies in its firefighting and inert gas systems, pointing to an explosion risk on the tanker. Severe corrosion had been even discovered by class just weeks before the incident. Holes damages had been found in the main deck coaming; pin holes leaks remained in the fire-main as well. However, all deficiencies were ignored until the disaster occurred [5].

Besides above tragic results in infrastructures and vehicles, there exists corrosion damage even in electronic industry--the industry of making product in small size. This problem refers to the growth of corrosive dendrites across circuit channels, as indicated in Figure 1. Due exposing the circuit board on corrosive environment such as sulfur or hydrochloride atmospheres, the metallic corrosion can be created in the form of creeping dendrites. Although the initial conductivity of the dendrites between two electrical poles is relatively small, failure occurs finally once the dendrites grow to certain thickness on which it is conductive enough to short the circuit. This corrosion rate depends on variables such as applied voltage, metals, surface moisture, as well as contamination extent. The corrosion growth between two pins will make the circuit board short and may lead to the failure of the whole device [6, 7].

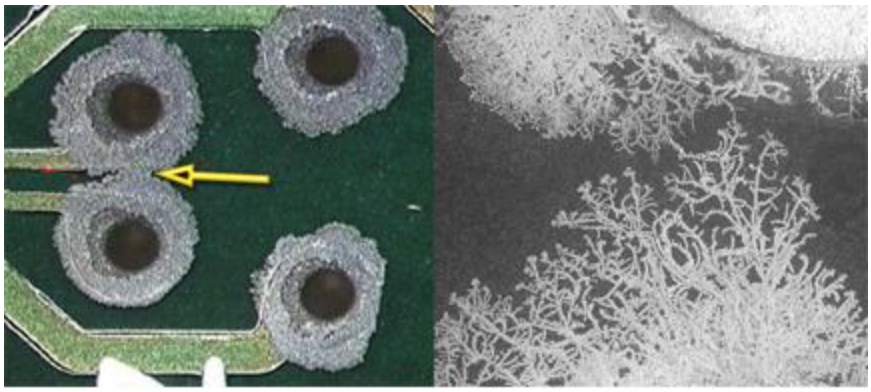

Figure 1 Dendrites (Cu_2S) creep on copper via pads (Courtesy Randy Schueller, Dell Inc.)

These huge devastations and considerable cost caused by corrosion expel scientists and engineers to study the corrosion and its mechanism, and effective approaches that are able to inspect and prevent corrosion occurrence. The lifetime of infrastructure can be prolonged by complete understanding the fundamentals of corrosion and its progressing so that appropriate control measures can be employed to overcome these problems [8, 9]. Therefore, understanding corrosion mechanism and its forms is essential in order to find the optimal methods of corrosion inspection and prevention.

1.2 Corrosion Mechanism and Forms

1.2.1 Corrosion Mechanism

Corrosion is related to chemical processes breaking chemical bonds through chemical reaction. Meanwhile, fracture is related to mechanical process breaking bonds physically through separation. These are separate considerations, but they are interconnected. Chemical environments aggravate fracture and fracture processes can permit one component to contaminate another. Corrosion is defined as the destructive and unintended attack of a metallic material, which is associated with electrochemical reactions and starts at the surface of the metal material [10]. The measure of a material to oxidize or lose electrons is demonstrated as oxidation potential. A difference between the oxidation potentials of two metals or sites gives rise to

corrosion that will 'eat' the metal. It is the potential difference as a driving force to cause metal corrosion subjected to a natural consequence of electrode potentials of various elements. Table 1 shows the standard oxidation potential values of various elements. The values of the oxidation potential in this table are used relative to each other, to determine the tendency of a metal to become a cathode (or anode) with respect to another metal.

Standard Oxidation-Reduction Potential at 25°C		
More Active	Reaction	Eo (volts)
	$Na \rightarrow Na^{+} + e^{-}$	-2.71
	$Mg \rightarrow Mg^{++} + 2e^{-}$	-2.38
	$Al \rightarrow Al^{+++} + 3e^{-}$	-1.66
	$Zn \rightarrow Zn^{++} + 2e^{-}$	-0.763
	$Fe \rightarrow Fe^{++} + 2e^{-}$	-0.409
	$Ni \rightarrow Ni^{++} + 2e^{-}$	-0.250
	$Pb \rightarrow Pb^{++} + 2e^{-}$	-0.125
	$H \rightarrow 2H^{+} + 2e^{-}$	0.00 Reference
	$Cu \rightarrow Cu^{++} + 2e^{-}$	+0.34
	$4OH^{-} \rightarrow O_2 + 2H_2O + 4e^{-}$	+0.401
	$Fe^{+2} \rightarrow Fe^{+++} + 2e^{-}$	+0.771
	$2Hg \rightarrow Hg_2^{++} + 2e^{-}$	+0.905
	$Ag \rightarrow Ag^{+} + e^{-}$	+0.799
	$2Br^{-} \rightarrow Br_2 + 2e^{-}$	+1.06
	$2H_2O \rightarrow O_2 + 4H^{+} + 4e^{-}$	+1.23
	$2Cl^{-} \rightarrow Cl_2 + 2e^{-}$	+1.36
	$Pt \rightarrow Pt^{++} + 2e^{-}$	+1.2
More Noble	$Au \rightarrow Au^{+++} + 3e^{-}$	+1.498

Table 1 Standard Oxidation-reduction Potentials taken from Ref. 3

In this table, the potential of hydrogen electrode is defined as zero and all other metal elements' potentials are refereed against the potential of hydrogen electrode. Metal elements whose standard potentials' values on this table are negative are reserved as anode half-cells. In contrast, metal elements having positive potentials are regarded as cathode half-cells, which means they are relatively passive in the oxidation-reduction reaction [11].

The corrosion process that occurs for metals is normally based on the formation of metal oxides and the subsequent degradation of such oxides that then lead to further oxidization of the

metal. The process that metal atoms lose electrons is regarded as the oxidation part of the reduction-oxidation reaction. The electrons generated from the oxidation of the metal atom are then transferred to a reducing reaction, typically generating negative ions of oxidizing elements. These reactions are often more volatile in acidic or oxygen-dissolved solution due to the enriched oxidizers in the solution, as well as the enhanced mobility of these oxidation ions over the immersed surface. An example (Fig. 2) of the electrochemical corrosion for metal is given by considering the iron metal. In the diluted chloride acid solution, iron atoms become positive charged by the oxidation process, while providing the excess electrons needed for the reduction process of the hydrogen molecules. The resulting ionic reaction is `the formation of the ferric iron on the surface of the metal. The overall "oxidation" reaction of the iron to form its oxide is presented as:

$$Fe + 2HCl \rightarrow FeCl_2 + H_2 \quad (1)$$

The oxidation reaction of iron atoms is,

$$Fe \rightarrow Fe^{2+} + 2e \quad (2)$$

with the complimentary reduction reaction of

$$2H^+ + 2e \rightarrow H_2 \quad (3)$$

which refers to hydrogen evolution and mostly occurs in acid condition.

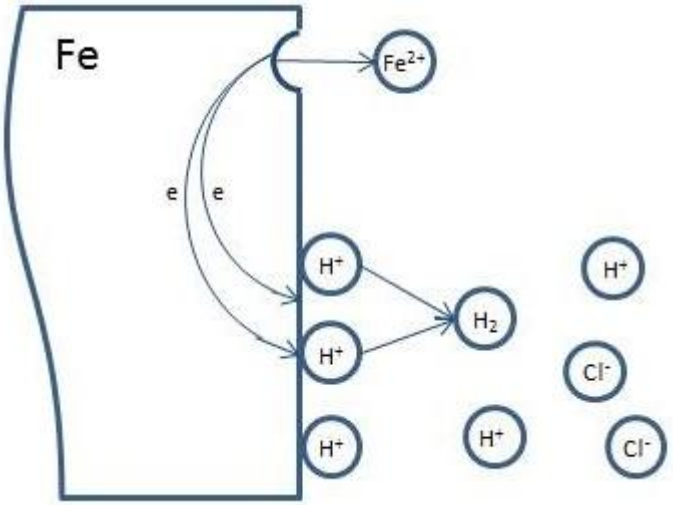

Figure 2 Illustration of oxidation reduction reaction

In some cases of metal materials, the formation of the oxidation film often provides itself as a protective barrier, such as sulfurate copper. However, this is not the case for most other metals (such as iron, zinc, etc.) where the corrosion of metallic material causes material loss, stress concentration, and structural damage. An oxidation or anodic reaction is remarked by the increase in valence or production of electrons. A lessening in valence charge or reduction of electrons is signified as a reduction or cathodic reaction. These two separated reactions are used to simplify and clarify the electrochemical of the process in cells. It must be noticed that, based on the principle of electrochemistry of corrosion, the rate of oxidation equals to that of reduction, which refers that both reactions have to occur simultaneously and at the identical rate on the metal surface. After discussing about the mechanism of corrosion, let's move on to the topic of corrosion forms that in general categorize corrosion into nine different types for study convenience.

1.2.2 Corrosion Forms

Since the large cost of corrosion, it is suggested that study of corrosion formation and methods of identifying corrosion's forms are crucial. The damage from corrosion can take many

forms. There are several different methods to categorize the types of corrosion. In general, there exist nine most common types of corrosion forms.

1.2.2.1 Uniform Attack

Uniform attack causes the metal to be consumed uniformly over the entire surface exposed or large area, which causes metal becoming thinner and eventually failure. The penetration of metal by corrosion at any point on the surface is no greater than twice of the average rate. This form of corrosion is less great concern from the standpoint of technique, since the life span of the attached machine can be estimated by relatively simple test—usually immersing specimens in the fluid involved. However, uniform attack is the most common corrosion form in reality, such as the internal corrosion of pipeline, the corrosion of the buried or immerged steel structures, and the corrosion of copper alloy under seawater. From the point view of measurement, uniform attack is detectable and its effect is predictable. Therefore, monitoring uniform attack is less challenging comparing with other types of corrosion. Figure 3 shows the uniform attack on a water tank.

Figure 3Uniform attack on the outside of water tank (Courtesy NASA Corrosion Technology Laboratory)

1.2.2.2 Galvanic Corrosion

There usually exists a potential difference between two different metals when they are immersed in corrosive or conductive solution. The potential difference generates electron flow between these two metals if they contact or electrically contact each other. The driving force (electromotive force or emf) that produces electron motion is the potential developed between two different metals and is governed by relative positions of the metals in the galvanic series. In general, the less resistant metal becomes anodic and tends to corrode at accelerated rate; while the more resistant metal becomes cathodic and tends to protectively resist corrosion. As shown in fig. 4, carbon steel is less resistant to corrosion than brass, so galvanic corrosion occurs on carbon steel pipe as it is connected to brass valve.

Galvanic corrosion does not occur when metals are exposed in completely dry environment, because there exits not electrolyte to carry current between the two electrode areas [12]. It is recognized that galvanic corrosion is considerably affected by the ratio of the cathodic to anodic areas. For a given current flow in the cell, the current density is greater for smaller electrode than for a larger one. The larger the current density is in the anodic area the larger the corrosion rate. Therefore, the unfavorable area ratio is formed of a large cathode and a small anode.

Figure 4 Galvanic corrosion in the connection of carbon steel pipe and brass valve (Courtesy CorrView International Inc.)

1.2.2.3 Crevice Corrosion

This kind of corrosion frequently occurs in crevices and other shielded areas on metal surfaces where small volumes of stagnant solution can retain, such as gasket surface, lap joints, and space under bolt and rivet heads. Also, crevice corrosion appears on locations on which deposits of sand, dirt and other solids perform as shield and form stagnant conditions. For corrosion sites, crevices with tens of micrometer are wide enough to allow liquid entry and stagnation, but they rarely occur within wide 1/8-in since stagnant liquid could be left by flow. The mechanism of crevice corrosion is based on the oxygen depletion in the crevice which results in the increase of positive charged metal irons creating from oxidation reaction in solution and thus these positive charges are balanced by the migration of chloride irons, therefore accelerating the dissolution of metal surface. The corrosion in crevice increases the oxygen reduction rate on adjacent surface and thus cathodically protects the external surfaces. This is the reason why during crevice corrosion, the attack is localized within shielded areas (Figure 5).

Figure 5 Crevice corrosion (beneath a seal) on a stainless steel flange exposed to a chloride-rich medium (Courtesy Multimedia Corrosion Guide)

1.2.2.4 Pitting Corrosion

In principle, pitting corrosion is the same as crevice corrosion, with the only distinction that it is self-initiating and does not need a crevice. Pits (Fig. 6) created by this corrosion have surface diameter approximately identical or less than its depth, and can cause perforation on the metal surface and lead to the failure of the entire system. On the point of view of devastation, pitting corrosion is regarded as more dangerous than uniform corrosion. To estimate pitting damage, it is more important to inspect the deepest pit rather than average pit depth for the consideration of the failure of the engineered system. Because of pitting corrosion associated with stagnant condition as that of crevice corrosion, the increase of flow rate is able to reduce the pitting corrosion and the formation of pits [14].

Figure 6 Pitting corrosion occurs on the surface of cast iron bathtub (Courtesy J.E.I. Metallurgical Inc)

1.2.2.5 Intergranular Corrosion

Intergranular corrosion is defined as a localized attack adjacent to grain boundaries associated with relatively little corrosion of the grains. It is resulted from three factors including impurities at the grain boundaries, enrichment of one of alloy elements and depletion of one of these elements near grain boundary areas. As shown in Figure 7, Austenitic stainless steel (304 stainless steel) containing 0.08% carbon and more than 17% chromium can corrode during

impoverishment of chromium in the grain boundary areas. When the stainless steel is heat-treated at temperature range 950-1450°F, insoluble $Cr_{23}C_6$ precipitates out of solid solution and gives rise to removing of chromium adjacent to precipitation areas. Although chromium carbide in the grain boundary is not attacked by corrosion, the chromium-depleted zone near the grain boundary is corroded and intergranular corrosion is formed [16]. The appearance of corroded areas is observed as deep narrow tranches on the alloy surface. Not only in stainless steel, can intergranular corrosion occur in other alloys such as Aluminum-copper alloy (Duraluminum).

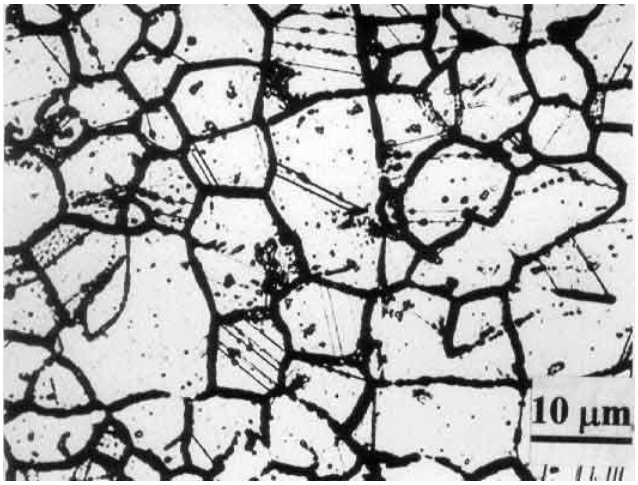

Figure 7 304 stainless steel susceptible to intergranular corrosion (Courtesy Corrosionclinic .com)

1.2.2.6 Selective Leaching (Dealloying)

Selective leaching is referred as the corrosion process by which one element is removed from a solid alloy; it is also called dealloying. To illustrate the mechanism of selective leaching, we use the dealloying of brass alloy as an example. Brass consists of 70% copper and 30% zinc and the dealloying corrosion can be recognized by rad or copper color appeared on the surface compared with its original yellow color. In brass, zinc is relatively reactive and thus dissolved in corrosive environment through oxidation reaction; while copper is noble and plates back on or forms copper oxide [17]. Therefore, in Figure 8, it can be observed that the dark area is where

zinc is leached out and that portion of alloy becomes weakened. In this process, since zinc is removed from the alloy, it is also named “dezincification”. But if other element (iron in cast iron) is leached rather zinc, the terminology would be changed to fit the specific process properly.

Figure 8 Dezincification of brass propeller blade (Courtesy Jim Aleszaka, Fracture Investigations Inc.)

1.2.2.7 Erosion Corrosion

Accelerating deterioration rate can be detected on a metal surface in the presence of relative movement between corrosive fluid and the attacked surface, which is referred to erosion corrosion (Fig. 9). From the definition of erosion corrosion, it is accepted that metal surface contacting with rapid corrosive flow tends to suffer the damage of erosion corrosion. Moreover, once the protective film on the metal surface is eaten or worn, the metal is exposed to the attack at a rapid rate. Consequently, for a specific metal or alloy, a critical velocity of a certain solution can be used to describe the value where attack increases at some rapid rate. For example, at 108°F, white fuming nitric acid solution can rapid attack 3003 aluminum at flow rate 4 ft/s. Turbulence flow causes more deteriorative damage on metal surface than laminar flow since because of its resulting of intimate contact between the environment and the metal. A special case of erosion corrosion is the cavitation damage, resulting from formation and collapse of

vapor bubbles in a liquid near a metal surface, where high velocity liquid flow and pressure come across.

Other than cavitation damage, fretting corrosion (Fig. 10) is another form of erosion corrosion, which occurs at contact areas between materials under the exposure of load subjected to vibration and slip. There are requirements for creating fretting corrosion: (1) the interface has to be under load. (2) repeated relative motion (~10^{-8}cm) between the two surfaces must exist. (3) the load and motion have to be enough to generate slip or deformation on the contacting surfaces.

Figure 9 Erosion-corrosion inside of copper alloy pipe (Courtesy Midland Corrosion Associates)

Figure 10 Fretting corrosion on the outer ring of bearing (Courtesy Maintenancebits, SKF group)

1.2.2.8 Stress corrosion cracking (SCC)

Stress corrosion refers to a mechanical chemical process that causes cracking by the simultaneous presence of tensile stress and a specific corrosive medium. It is possible to believe that there is no alloy being able to escape from stress corrosion cracking. Temperature, solution composition, metal composition and structure and stress are important variables that affect this corrosion, as shown in Figure 11, that stress corrosion of a stainless steel hanger results from applied tensile stress, while exposing in NaCl vapor environment. Typically, instead of the usage of alloy, pure metal (for instance 99.999% copper) can be applied to reduce the susceptibility of stress corrosion [18]. Although multiple theories have been posted on the study of the mechanism of stress corrosion such as dislocation coplanarity, stress-accelerated dissolution, hydride formation, film rupture and tunnel pitting and tearing, the involved mechanism still cannot be well understood due to the complexity of metal interface and environment properties.

Figure 11 Stress corrosion in the back of a stainless steel hanger (Courtesy TradgirlWiki photo taken from Cayman Brac)

1.2.2.9 Hydrogen Damage

Hydrogen damage is regarded as a mechanical damage of the metal leading from the presence of hydrogen or interaction with hydrogen. Atomic hydrogen is the only species that can diffuse into steel and other metal materials, but its molecular form cannot diffuse through metal since its size is bigger. These entrapped molecules result in weakness and damages of metals. A typical damage caused by hydrogen is called hydrogen blistering [19].

Hydrogen blistering is caused by the penetration of hydrogen into metal, which leads to loss of ductility and tensile strength of the metal material. As shown in Figure 12, when the interior surface of the steel is exposed to concentrated acid electrolyte, some of the hydrogen ions on the steel surface diffuse into the material instead of the combination of molecules. These diffused hydrogen can combine and form hydrogen molecules in a void into the steel, which is a common defect in rimmed steel. However, these gathered hydrogen molecules cannot diffuse out and thus lead to the increase of pressure interior of steel [20]. The pressure can reach to thousand atmospheres and is sufficient to rupture the steel.

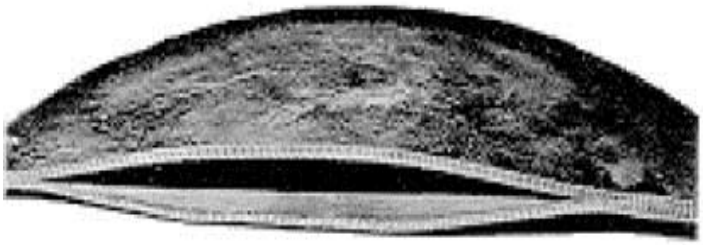

Figure 12 Hydrogen blistering in a carbon steel plate (Courtesy NASA Corrosion Technology Laboratory)

Overall, uniform and galvanic corrosion are the two fundamental types that reflect the single and multi-material electrochemical reactions described above. The proposed MEMS corrosion sensor aims to inspect, but not be limited to, these two forms of corrosion (they are also the most common corrosion forms found in infrastructure). This corrosion sensor is also expected to

extensively monitor other forms of corrosion such as crevice and pitting corrosion via signal analysis, data correlation and installation of sensor into gaps, etc. An excellent corrosion detection or monitoring system has the capability to inspect average corrosion over a wide range of operational structures as well as onset corrosion in any location. It is impossible to achieve the goal only relying on single corrosion sensor; multiple sensor arrays should be applied and thus cost-effective becomes a main consideration in selecting monitoring system. In addition, the monitoring system is also desired to have rapid response, accurate data acquisition, noisy filtration and real-time inspection, etc. Hereby, a review of widely used corrosion monitoring systems is presented to access to corrosion inspection and selection of proper types of monitoring techniques that are meaningful to the application of specific corrosion sensor.

1.3 Corrosion Monitoring

Corrosion monitoring refers to corrosion measurements performed under industrial or practical operating conditions. Corrosion monitoring may be described as acquiring data on the rate of material degradation. However, such data are generally of limited usage and need to be converted into useful information to be included in a corrosion management program. This requirement has led to the evolution of corrosion monitoring tools toward real-time data acquisition, process control tools, knowledge-based systems, and smart structures [21].

The important step of a corrosion monitoring program is to define the monitoring objective. If corrosion monitoring is done for corrosion control, the purpose is to assure that asset life is not threatened by too many high corrosion rate events. In this case, the main objective of corrosion monitoring is to limit the “corrosion events”, without completely using the corrosion allowance of a system before the end of its design life. The main factors that govern the design of a

monitoring system are available corrosion allowance [22]; uncontrolled corrosion rates; event rates; corrosion rate detection sensitivity and response rate; and required service life.

Although many types of monitoring devices can be chosen, the functionality of each monitoring technique is limited by conditions, in terms of cost, environment, durability, monitoring range, safety [23]. For example, coupons cannot achieve long test time which is needed for reducing measurement error, due to the limited ability to control the environment inspected. Hydrogen evolution technique is not suitable to indicate corrosion rates since the absolute correlation between hydrogen diffusion rates and corrosion rates is not known. The cost of the instrument for field signature measurement is very expensive. Other conditions also strictly limit the applications of monitoring techniques. For example, crevice corrosion is difficult to measure due to its narrow space and assembly requirement.

In simplest form of corrosion monitoring, it may be described as acquiring data on the rate of material degradation. For detecting and controlling the corrosion deterioration, the corrosion monitoring techniques must be developed and is actually considered as a mature field. However, it depends on what one would call maturity when the associated cost is still prohibitively high. In general, there are three types of corrosion monitoring techniques: offline, online, and real-time measurements [24]. The typical offline measurement is based on the application of material coupons that have composition similar to that of the interested process equipment. The measurement data usually come from measured change of metal thickness (such as from ultrasonic inspection on coupon components or electrical resistance measurement) or weight loss of coupons. It takes months, even years sometimes, to finish measurement and data collection by offline approach. Data collected indicate corrosion only after the deterioration has occurred.

Offline measurement can only provide average corrosion rate in the data collection period and does not provide any information of the peak corrosion rates and its associated conditions [25].

For online measurement, the probe used to monitor corrosion is connect to a data memory device that is able to record data of corrosion rate measurement automatically over weeks or months. However, the data acquired cannot be accessed or processed in real-time. Another disadvantage is the corrosion information only can be obtained after the damage has happened [26, 27].

In the above two approaches, problems are viewed after the corrosion damage and cannot directly link causes and effects immediately, thus preventing mitigation efforts. In order to continuously monitor the corrosion and obtain feedback data, real-time measurement techniques is used. The real-time measurement uses on-board memory of a single transmitter to transport corrosion data [28]. It often applies advanced electrical measurement techniques with analysis algorithms to provide higher corrosion rate reporting in real-time.

Real-time measurement techniques can monitor large process equipment by distributing sensors across the equipment. This often results in using a large amount of sensors for real-time measurement of large structures or infrastructures. Traditionally, a sensor probe is made by using the same or similar metal material to that of the monitored equipment. The sizes of these sensors are often on the order of centimeters and have long sensor time constants (from minutes to hours). For example, T. Prosek and M. Kouril's real time corrosion monitoring device in atmospheric conditions yields a time response of 1-2 hours [29, 30]. A recent report from Russell Kane reported a 7 minutes response time. However, the performance between sensitivity and life is often coupled (high sensitivity yields a short life sensor due to the design of the sensing element). Consecrations of sensitivity, life-span, cost-effect and sensor size have been taken in our

research of investigation of MEMS-based corrosion sensor. MEMS technology is a promising approach to solve these difficulties encountered in the traditional, industry-used corrosion sensor. Life-span can be prolonged without reducing sensitivity Decreasing sensor size can be achieved without increasing producing cost.

Both off-line and real-time monitoring techniques can be coupled with our MEMS-based corrosion sensor, depending on the monitored structures. The off-line system can be used to inspect corrosion of reinforcement in sound concrete as, with RFID power supply, sensor device is able to be embedded into concrete and attached to the steel framework [31]. The real-time monitoring system can be utilized to structures that are exclusively exposed to ambient environment without concrete placed around, such as bridge or signal emission tower.

1.4 MEMS Fabrication of Corrosion Sensor

Now we can discuss how to fabricate this corrosion sensor in terms of MEMS technology. The two key attributes of the proposed Micro-Electro-Mechanical System (MEMS) sensor are high sensitivity and long sensor life, in addition to other possible advantages typical of MEMS devices. MEMS technology has been successful in the physical sensing context and has yielded a range of small, rugged and inexpensive devices such as accelerometers, strain gauges, microphones, air mass flow sensors, pressure sensors, and more recently gyroscopes and yaw-rate sensors. Some MEMS sensors have been developed to meet the demanding needs of the automotive industry and are used by the millions in engine management systems, to trigger air bags and in anti-rollover, vehicle stability control, and GPS navigation systems [32]. In terms of chemical (gas) sensing, the predominant sensing material used in MEMS is based on metal oxide thin films. These are relatively simple chemo-resistive devices while several more complex MEMS-based gas sensors based on techniques such as NDIR (non-dispersive IR absorption),

thermal conductivity, and photo-acoustics, together with micro-spectrometers, have recently enjoyed a limited but growing degree of commercial success. However, the common problem in such devices is its degraded performance when compared to the benchmarking method of mass-spectroscopy [33]. For example, miniaturized NDIR sensors suffer from low sensitivities due to the necessarily short optical path-lengths involved, restricting their use to applications involving relatively high gas concentrations.

MEMS technology has exerted an impact on physical sensing and growing impact on gas sensing, but currently is of minimal impact on chemical sensing. MEMS technology is able to provide batch processing (low cost), lithographic alignment (high resolution), small device (decrease material weight, power and high sensitivity), and IC compatibility (smartness).

The development of MEMS fabrication depends on two major manufacturing technology, bulk micromachining and surface micromachining [34].

Bulk micromachining is usually defined as the technique to fabricate desired structures by selectively etching inside of the substrate. These structures from bulk micromachining can be various such as cantilever, bridge, membrane, trench, nozzle, cavity. The dimension of these structures can range from hundreds of micrometers to several millimeters. To fabricate desired devices, both wet etching and dry etching are employed and the etching thickness of both techniques can range from several micrometers to hundreds of micrometers. For wet etching, the structures can be isotropically, anisotropically and directionally etched, depending on the design requirements [35]. For example, silicon wafer is the most commonly used substrate due to its crystal orientation for anisotropically wet etching by KOH or TMAH solution. In advance, desired patterns can be transferred on silicon substrate through photolithography technique; and then the wafer can be selectively wet-etched by dipping into KOH solution. The etching

thickness can by controlled by etching time. Furthermore, more precise thickness can be achieved by alternative wet etching techniques such as doping selective etching or bias dependent etching. Comparing to wet etching, dry etching is regarded to have more application on a wider range of structure type, size and shape. Reactive ion etching (RIE) is a commonly used try etching approach in micro-fabrication. Besides etching, bonding technique (fusion and anodic bonding) is also applied by bulk micromachining. In practice, the majority of commercial micro-devices are made by bulk micromachining technique, such as pressure sensor, accelerometer etc. [36, 37].

Unlike bulk micromachining, where structures are formed by etching the substrates, surface micromachining is to build structures on top of the substrate using deposition and etching techniques. The structure dimensions from surface micromachining are much smaller than these from bulk micromachining, only ranging from hundreds of micrometers to submicrometers [38]. A key technical aspect of surface micromachining is the utilization of sacrificial layer which is under the building structure. To obtain the complete device, the sacrificial layer has to be etched out by either dry (plasma) or wet etching approach. For example, for some mechanical microstructures, silicon dioxide is usually applied as the sacrificial layer on top on poly-silicon substrate. However, it must be pointed out that applying wet etching approach to remove sacrificial layer may cause stiction between the structure layer and the substrate. But this problem can be solved using supercritical drying carbon dioxide or freeze drying. Since these structures are built on top on substrate, not inside, the quality of substrate is not as important as in bulk micromachining [39, 40]. Therefore, glass or plastic substrates sometimes can be utilized instead of expensive silicon substrate.

To successfully fabricate the corrosion sensor, surface micromachining would be mostly employed to pattern microstructures on the whole wafer and with high yield.

The mechanism of the corrosion sensor is based on the mass transport of corrosive species through the sensor matrix. When the metal particles embedded in the matrix corrode, the electrical resistivity increases, due to the increase of particle resistance. The resistivity change can be converted to electrical signal that can be detected to monitor corrosion rate. This type of sensor has high sensitivity due to its micro-size; it also has the ability to tailor the dimension of the composite material thanks to the MEMS-based fabrication technique. As mentioned above, to successfully fabricate the corrosion sensor, the fundamental parameters related to sensor element material (metal particle type, size, and mass percentage in composites), sensor electrical properties (electrical resistivity), and fabrication technique (MEMS-based polymer pattering technique) needed to be determined first.

The fabrication technique used to pattern the MEMS sensor element is called Direct Polymer Patterning On Substrate Technique (DPPOST), which was developed to pattern polymer (elastomers) based on lift-off technique [41]. As shown in the Figure 13, the DPPOST is similar to lift-off approach. It employs the Omnicoat™ as the sacrificial layer to remove the supporting wall surrounding the desired pattern. DPPOST has been proved to be a successful technique for fabricating polymer based materials that are difficult to etch or deposit. But due to our goal to achieve near 100% fabrication yield, a modified approach to DPPOST is based on forming a vertical Omnicoat™ layer to reduce the stiction between the polymer and the mold. The accomplishment of DPPOST technique provides the capability of micro-fabricating the normally inert polymeric materials and thus offers the possibility of functionalizing these inert polymers as active structures [42]. For example, by mixing conductive particles in elastomers, high elasticity

MEMS sensors and actuators can be achieved by switching to these materials on previously developed designs.

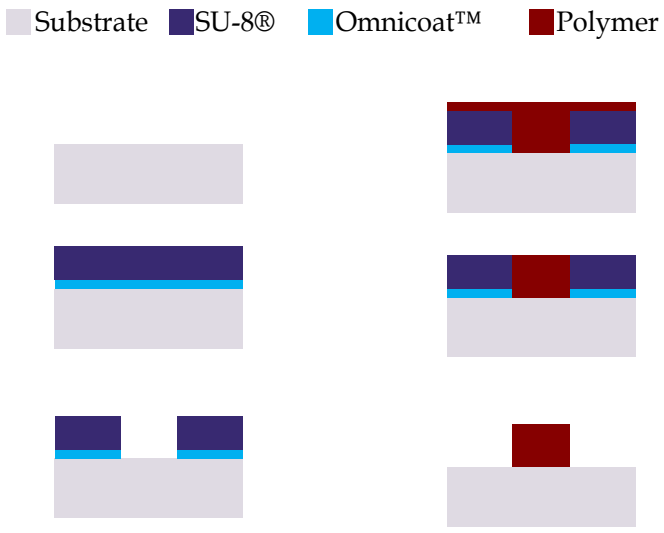

Figure 13 The process flow of DPPOST

1.5 Functional Matrix Material of Corrosion Sensor (Silicone and PDMS)

As mentioned above, using DPPOST technique, sensor elements with various dimensions can be successfully patterned on substrate and these elements are consisting of composites of metallic particles and polymeric materials (mostly elastomers). To better understanding the properties of sensing unit, it is necessary to discuss the polymeric materials.

Polymers are defined as the large molecules that are composed of repeating structural units--monomers. Polymer can be categorized of one of three solids (the rest two are metal and inorganic glass, respectively). In general, polymers are composed of constituent atoms such as carbon, oxygen or silicon, which are joined in linear structure by covalent bonds. In the chain structure, each atom provides two valence electrons to bond with its neighbor atoms in order to form the high molecule weight linear structure. Polymers can also be classified into two categories according to whether there exist side chains bonded to its backbone. In the first, the presented chains are all straight with little or no side chains. Such linear polymers can be melted

and re-melted without changing the basic structure (therefore, having fabrication advantage). This sort of polymer is called thermoplastic polymer; examples are Acrylonitrile butadiene styrene (ABS), Poly (methyl methacrylate) (PMMA). In the second, side chains are present and form crosslinks between chains. These polymers once formed by heating will not melt uniformly when reheated. These polymers are called thermosetting polymers and usually are strong with respect to intermolecular bonds (Epoxy Resin, Polyimides, Silicone, e.g.) [43].

Both thermoplastic and thermoset polymers have intertwined chains that result in amorphous structures of polymer. However, the bonds that form this structure are different. For a thermoplastic polymer, van der Waals bonding and hydrogen bonding associated with inter-chain entanglement are major proximity that is responsible for joining chains together. On the other hand, covalent bonds that are generated by crosslinking due to side chains can form 3D network structure in thermoset polymers. Since covalent bonds are much stronger than either van der Waals or hydrogen bonding, the thermosetting polymers are stronger than thermoplastic polymers and thus have higher strength and melting point [43].

Silicone belongs to the category of thermosetting polymer. Its backbone consists of repeating silicon to oxygen bonds; and also the silicon atoms bond to two adjacent organic groups such as methyl group. A typical chemical structure of silicone is presented in Figure 14, which is called difunctional Polydimethysiloxane (PDMS), due to its two oxygen bonds on both sides as the functional group [44].

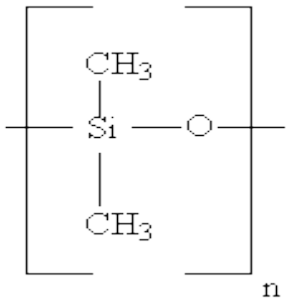

Figure 14 Molecular structure of PDMS

Besides the D formula for PDMS, there exist other three types of formula (Fig. 15), M (monofunctional), T (trifunctional) and Q (tetrafunctional), respectively, as follows (The PDMS product (from Dow Corning Co.) used for our research consists of dimethyl siloxane dimethylvinyl-terminated (>60 Wt.%) and dimethyvinylated and trimethylated silica):

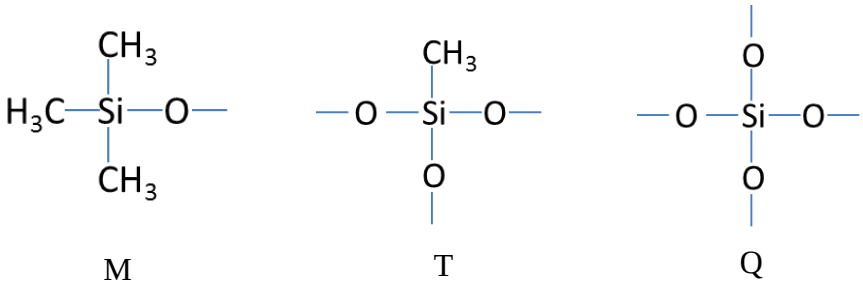

Figure 15 Molecular structures of M (monofunctional), T (trifunctional) and Q (tetrafunctional)

Silicone polymers can be easily crosslinked to form a 3D network (PDMS e.g.), by exposure to radiation, condensation or addition reactions. In addition, cure crosslink is attained by addition of vinyl terminated (endblocked) groups carried by functional oligomers. The advantage of this kind of crosslink is that shrinkage problem is eliminated since crosslinking can occur by an addition mechanism and crosslinked pieces can be controlled very accurately without providing by-product in the reaction.

PDMS exhibits many applications in as release agents, rubber molds, sealants, surfactants, water repellents, adhesives, processing aids, foam control agents, in biomedical devices, personal care and cosmetic products [44]. It is the combination of organic side groups and the inorganic

backbone that provides its exceptional physical and chemical properties. PDMS displays excellent stability under high temperature, UV light and severe weather and chemical resistance. The reason for this stability is because of the extremely high energy of silicon to oxygen bond (461kJ/mol) in its Si-O bond [45]. This bond length is 1.64+/-0.03A, with O-Si-O angle 140°C, which partially explains the low glass transition temperature Tg of about -123°C [46]. It has been interpreted that the low intermolecular force results in a large molar volume (75.5cm^3/mol), a low cohesion energy density, as well as its low surface tension, surface energy solubility parameter and dielectric constant [47].

In addition, the very strong hydrophobic character of the methyl groups due to the low rotational energy around the Si-O backbone leads hydrophobicity and moisture resistance [43]. Other useful properties of PDMS include good resistance to UV radiation, high permittivity to gases, excellent damping behavior. Different types of PDMS can be dissolved in benzene, toluene, ether and other solvents, and it is also partially soluble in solvents such as acetone, ethanol, isopropanol and butanol, but never soluble in water, methanol and paraffine oil [48, 49]. At 25°C temperature, its viscosity varies from 0.65cs to 60,000cs with respect to its molecular weight change from 162g/mol to 116,500g/mol [50, 51]. Moreover, the solubility of gases in PDMS membrane at 25°C/760mmHg are presented by Robb WL that the solubility of oxygen gas is 0.31ml/g, that of air is 0.33 ml/g and 0.57 ml/g for CH_4 [52]. Non-polar molecules are more soluble and easier to diffuse through comparing with polar molecules due to the non-polarization of PDMS. There are considerable studies have been done by both by experiments and simulations on the diffusion of small molecules through PDMS [53]. Additionally, different diffusion models have been developed to interpret the mechanism of diffusion through cross-linked polymer materials. In the general, fick's first and second laws are the major tools that are

used to describe the diffusion process. But the diffusion coefficient varies depending on the nature of polymers, the penetrants involved and fillers, etc. Since the mechanism of the corrosion sensor is based on the mass transport of corrosive species through the sensor matrix, in the following section, the common diffusion theories and their physical models will be discussed.

1.6 Diffusion Through Corrosion Sensor

1.6.1 Fick's Diffusion (Fick's First Law and Second Law)

Diffusion refers to the process of movement of matter from one portion of a system to another [54]. This process is mainly responsible to random molecular motion and thus it depends on temperature, pressure, solute size and solvent properties. Diffusion through a gas is fast (10cm/min) comparing with that through liquid (0.05cm/min) and solid (0.00001cm/min) [55]. Diffusion rates through polymers lie in between the value in liquid and solid, but the process is more complex and unpredicted. In decades, although many theories have been developed to describe diffusion in polymer and made great progress in understanding the transport mechanisms in polymers, there still exist many unknowns that awaits discovery. Overall these theories start over the fundamental of transport of small molecules through polymer membrane in terms of random molecular motion of individual molecule [54]. The force that drives molecules through membrane is generated from concentration difference in the phase interface separated by the polymer membrane [55]. This force involves sorption, diffusion and permeation that contribute to equilibrating the concentration difference. The process of transport is governed by Fick's first law [56], where the flux J (the number of molecules diffusing through unit surface area per unit time) in the direction of molecule motion, is proportional to the concentration C gradient.

$$J(x) = -D[\frac{\partial C(x)}{\partial x}] \tag{4}$$

where D is the diffusion coefficient. The minus sign on the right side of the equation indicates that the flux direction is opposite to concentration gradient, which means that molecules move toward to the direction of reducing concentration gradient.

In three dimensions, the first law can be presented in Cartesian coordinates as

$$J(x,y,z) = -D[\frac{\partial C(x,y,z)}{\partial x} i + \frac{\partial C(x,y,z)}{\partial y} j + \frac{\partial C(x,y,z)}{\partial z} k] = -D\nabla c(x,y,z) \quad (5)$$

where the last part of the equation uses gradient operator to simplify the notations.

The first law has very limited application in practice since the flux is more difficult to measure than concentration. Also, the first law can not be used in measurement under unsteady state (it is not a function of time) [56]. Therefore, Fick's second law was developed to express how diffusion causes the concentration to change with time, as

$$\frac{\partial C(x,t)}{\partial t} = D[\frac{\partial^2 C(x,t)}{\partial x^2}] \quad (6)$$

In three dimensions, this equation can be rewritten in terms of Cartesian coordinates:

$$\frac{\partial C(x,y,z,t)}{\partial t} = D[\frac{\partial^2 C(x,y,z,t)}{\partial x^2} + \frac{\partial^2 C(x,y,z,t)}{\partial y^2} + \frac{\partial^2 C(x,y,z,t)}{\partial z^2}] = D\nabla^2 c(x,y,z,t) \quad (7)$$

the last part of above equation, can be simplified and rewritten by a Laplace operator.

Equation (7) is a second order partial differential equation (PDE) and its solution can be found by several mathematical approaches. Hereby the key is not to solve the PDE mathematically but to find a solution that fits congruently with the physical system. Therefore, auxiliary functions such as boundary and/or initial conditions should be considered together as solving above equations. This procedure is tedious by hands, but fortunately some computational programs (Matlab®, Labview®) are applicable to solving these equations.

1.6.2 Diffusion Derived From Fick's Law

The below section describes the diffusion under condition where the diffusion coefficient of polymers is not a constant but relies on variables (concentration, interaction, and free volumes).

Based on the Fick's law, diffusion phenomena in polymer can be categorized to three cases: Fickian diffusion, Non-Fickian diffusion and anomalous diffusion, with respect to diffusion rate and polymer relaxation rate.

Fickian diffusion is used to describe solute transport through a rubbery polymer, which means polymer exists in temperature above its glass transition temperature (T_g). In this case, the amount of solvent absorbed per unit area of polymer at time t, M_t is presented by [57]

$$M_t = kt^{\frac{1}{2}} \tag{8}$$

where k is a constant. It indicates that diffusion rate R_d is less the rate of polymer relaxation R_r.

In the case of Non-Fickian diffusion, transport of solvent is for the study of glassy polymer indicating that the temperature is below T_g. Then M_t is described by the relationship:

$$M_t = kt \tag{9}$$

representing that the diffusion distance is proportional to time and thus the diffusion rate R_d is faster than polymer relaxation R_r.

For the cases in between Fickian and Non-Fickian diffusion, they can be interpreted by anomalous diffusion, in which

$$M_t = kt^n \ , \ \frac{1}{2} < n < 1 \tag{10}$$

Since Fick's law is the fundamental principle of studying diffusion, it is necessary to fully understand its principles. An important parameter in Fick's law is the diffusion coefficient D, defined as the concentration gradient of solvent along the cross section over which diffusion is

occurring. For the initial mixture of two pure species A and B, their diffusion coefficients are D_A and D_B, respectively and they are called intrinsic diffusion coefficients. For convenience, a diffusion coefficients related to both D_A and D_B can be described by the equation [58]

$$D_m = V_A C_A (D_B - D_A) + D_A \tag{11}$$

where D_m is defined as the mutual diffusion coefficient, C_A is the amount of A in the binary system and V_A is constant volume of component A.

Besides the initial state of mixture of two species, in equilibrium system such as polymer gels or solutions, the diffusion also occurs even without a concentration gradient. Therefore, the diffusion coefficient in this case can be defined as self-diffusion coefficient and the relation between self diffusion coefficient and intrinsic diffusion coefficient can be defined by

$$\frac{1}{D} = \frac{C_A}{D_A}\left(\frac{\partial \mu_A}{\partial C_A}\right) \tag{12}$$

where D is the self diffusion coefficient of component A. When the diffusant concentration in solution is very low, self-diffusion can be named tracer diffusion, such as the study of water vapor diffusion in polymer film [55].

Generally, researchers in the area of diffusion through polymer develop five major theories applied on the study of diffusion in polymer systems of solution, gel and solid by means of gravimetry, membrane permeation, fluorescence, dynamic light scattering and nuclear magnetic resonance (NMR).

Besides Fick's theory, mass transport through polymers can also be explained on the basis of the thermodynamics of solubility or swelling. As penetrants diffuse into polymer, the network is elongated and thus a restrictive force is developed to balance the penetration of solvents resulting from osmotic pressure, the system will reach eventually equilibrium as the elastic restoring force is equal to the exerted swelling in opposite direction. This is applicable to explain swelling in

lightly crosslinked rubber network rather than semi-crystalline thermoplastic resins below glass transition temperature.

Factors attributing to categorizing mass diffusion into these three types of models (Fickian, Non-Fickian and anomalous diffusion) are the nature of polymers, penetrants and fillers. The following section will discuss details of the three factors respectively.

1.6.3 Factors Contributing to Diffusion in Polymer

1.6.3.1 Nature of Polymer

Transport behavior in polymers is affected by free volume and segmental mobility of polymer chains. The increase of free volume in polymer is associated with increase of diffusivity, so as to segmental mobility of polymer chains. There are mainly five factors that influence segmental mobility: the extent of unsaturation, degree of crosslinking, structures of polymer chains, degree of crystallinity, and glass transition temperature, T_g of the polymeric system.

It is demonstrated that diffusivity decreases as the extent of unsaturation in polymer backbone is reduced by hydrogenation. For example, the diffusivity of octadecane through poloyisoprene decreases three times as the residual unsaturation is lowered from 100 to 37 percent [59]. The reason is that the unsaturation in polymer chains increases the segmental mobility and thus increases the diffusivity.

Crosslinking in a polymer restrict the segmental mobility of chains and thus hinders the penetration of diffusants, which has been proven by the study of diffusion of a series of alkanes through rubbers as reported by Barrer and Skirrow [60]. Their study also interpreted that the diffusivity depends on the extent of crosslinking. For low level crosslinking, the diffusivity decreases linearly with an increase of crosslink density; for high level crosslinking, the decreasing diffusivity moves toward stability. Diffusivity is also affected by the nature of

crosslinks. For example conventional cross-link system absorbs the highest amount of solvent, whereas the peroxide system takes the lowest.

The influence of polymer structures on diffusivity is attributed to the segment motion of backbone and availability of free volume. The Si-O backbone displays excellent mobility and permeability comparing to Si-CH_2 backbone. However, if a $(CH_2)_n$ sequence is insert in siloxane backbone, the permeability dramatically drops due to the reduce of backbone motion caused by $(CH_2)_n$ sequence. Similarly, the Si-O backbone substitution of methyl by more bulky groups (such as phenyl ring) decreases the permeability. Moreover, it seems that the substitution of bulky functional groups in side chains has greater effect on decreasing diffusivity than the substitution of these groups in the backbones [61, 62, 63]. In addition, an increase of chain ends in polymer networks results in the increasing sites for sobbing more diffusants into glassy polymer. Increasing chain ends can be accessible by reducing polymer molecular weight [64].

The induced crystallinity decreases the permeability by reducing the free energy of the mixture.

Polymers having low glass transition temperature usually possess great segmental mobility and thus have high diffusivity [65]. Besides the five major factors, the interactions (causing the cohesive energy of the polymer increase) between penetrants and functional groups presented in polymer chains can reduce the diffusivity as well [66].

1.6.3.2 Penetrant

Changing the size or shape of transport penetrant influences its diffusivity in polymer, especially in glassy polymers. Because in rubbery polymer, energy is necessary to generate sites for accommodating the molecules and larger permeants associated with increase of the heat of sorption leading to plasticization of the polymer chains. Therefore, it means that larger

penetrating molecules in rubbery polymer give rise to higher plasticization and sorption into the polymers. Overall the size of permeant does have great influence on their diffusivity in rubbery polymer. Decreasing penetrant's size or the chain length of the penetrated polymeric matrix that is related to the increase of the diffusivity has been reported by many investigators [67, 68, 69]. Additionally, it has been suggested that the flattened or elongated molecules have higher permeability than spherical molecules of the same volume [70].

1.6.3.3 Fillers

Diffusion in polymer composites considerably depends on the compatibility of fillers with the polymer matrix. If the inert fillers are compatible with polymer matrix such as rubber-fiber system, the diffusion rate will decrease with an increase of the filler's volume fraction, since fillers in the polymer take free volume space and create a tortuous path hindering the permeation of diffusants. On the other hand, if the fillers are not compatible with polymer, larger free volume (more holes) is generated and thus increases the permeability of the composite [71, 72].

1.6.4 Diffusion Theories Referred to Obstruction Effects

This type of model is based on the assumption that self-diffusion coefficient of polymer is much smaller than that of diffusant such as solvent molecules. Therefore, polymer chains are regarded as fixed and impenetrable in a solution. This assumption increases the mean path length of the diffusing molecules between two points in the system [73].

1.6.4.1 Maxwell-Fricke Model

The Maxwell-Fricke model, which is based on the obstruction theory, is represented by the equation (13) as

$$\frac{D(1-\varphi)}{D_0} = \frac{1-\varphi'}{1+\varphi' x} \tag{13}$$

where D is the diffusion coefficient, D_0 is the diffusion coefficient in pure solvent, φ is the volume fraction of polymer in solution, φ' is the volume fraction of the polymer and non-diffusing solvent bound to polymer, and x is a factor describing the shape of the solvent (its value ranges 1.5~2.0 for sphere shape). Cheever [74] studied the diffusion of water in a suspension of polymer latex at low concentration and found that the diffusion could be explained correctly by the Maxwell-Fricke model. However, by studying self diffusion of solvents (toluene, ethylbenzene, cumene, tert-butyl acetate et al.) in PMMA system at concentration between 0--50 wt%, Waggoner [73] reported that the Maxwell-Fricke model did not fit well with experimental results even in low concentrated system. From the above two studies, it can be seen that Maxwell-Fricke model wroks well for the low concentrated system with small diffusant size such as water molecules, but at medium or high concentration and large diffusants, the Maxwell-Fricke model is not applicable. The reason seems to be that Maxwell-Fricke model does not consider the molecular weight of polymer which is an important factor affecting diffusion processes.

1.6.4.2 Mackie and Meares Model

Mackie and Meares [75] evaluated the obstruction effect and developed a physical model based on the assumption that the diffusion in the polymer solution is dominated by the mobility of ions or water not that of polymer and sites occupied by polymers cannot be accessed by ions or water, so the path length for molecular motion is increased by the obstruction of the polymer chains. Thus, the penetrant diffusion coefficient can be described by

$$\frac{D}{D_0} = \left(\frac{1-\varphi}{1+\varphi}\right)^2 \tag{14}$$

All the notations in Eq. 14. are identical to those defined in Eq. 13. According to Zhu's experiments, this model provides satisfactory results for the diffusion of small diffusants into

cellulosic networks at concentrations up to 60 wt%. However, for large size diffusants, the Mackie and Meares's model does not fit well [77].

Both Maxwell-Fricke model and Mackie and Meares model, and other models such as Ogston's model [77], all based on consideration of sedimentation of proteins in hyaluronic acid solutions [78], Johansson's model [79] regarding to hard sphere theory. But all these models have more limitations in application than both the Maxwell-Fricke model and Mackie and Meares model. For example, Johansson's model can only be applied upon the condition that diffusant's hydrodynamic radius is less than 20 angstrom [80].

1.6.5 Hydrodynamic Theories

Hydrodynamic models are developed based on the hydrodynamic interactions among solvent, polymer and solute in the system. Among these interactions, the frictional interaction between solute and polymer is regarded as the most dominant factor.

1.6.5.1 Cukier Model

The Cukier model [81] was developed to elucidate the diffusion of Brownian sphere in dilute and semi-dilute polymer solutions. In contrast to the dilute polymer solution case, where the polymer monomers are inhomogenously dispersed in solvent and thus in the solution there still exists sites occupied only by pure solvent, Cukier consider semi-dilute polymer solution as a homogenous system in which polymer chains are homogenously distributed in solution and thus polymer chains can overlap. Different from obstruction model, Cukier model can be applied in the system where overlapping occurs. Due to the overlay of polymer chains, screening effect between polymer chains and solutes is carried out in analysis of diffusion. The diffusion coefficient of diffusant molecules D in semi-dilute solution can be presented by the equation (15):

$$D = D_0 \exp(-\kappa R_h) \tag{15}$$

where D_0 is diffusion coefficient in pure solvent (incompressible Navier-Stokes fluid), κ is the parameter characterizing screening hydrodynamic interactions between polymer and solute, and R_h is the hydrodynamics radius of the diffusant. For polymer molecules that are rod-like, $\kappa = \frac{3\pi L n_L}{\ln(L/b)}$, where L and b are the rod length and diameter, respectively, and n_L is the number density of polymer molecules. If polymer molecules are coil-like, $\kappa = 6\pi a n_a$, where a is the radius of coil-liker polymer molecules and n_a is the number density of polymer molecules.

Using Cukier's model, Mel'nichenko found the agreement with his experimental data for the study of diffusion of water in moderately concentrated hydrogels [82], polyacrylamide (PA) and silica gels [83]. However, Cukier's theory does not fit the diffusion of protein in PA gels [84], polystyrene (linear and star-branched) diffusing in poly(vinylmethyl ether) [85, 86] and the diffusion of abbumin in hyaluronic acid and dextran gels [87]. From these studies, one conclusion is that Cukier model fits well for small diffusant molecules in semi-dilute polymer solution, but may not be applicable for large size diffusant (such as protein) within a concentrated polymer solution. However, all these studies apparently indicate a correlation between screening parameter and solution concentration.

There is another hydrodynamic model, the Altenberger model [88], which is similar to Cukier's model, based on the assumption that dispersed polymer molecules in solution are regarded as rigid bodies that are immobile and impenetrable, and that solvent is considered as an incompressible Newtonian fluid. The hydrodynamic interaction between polymer chains and diffusant is described as friction with each other and the diffusion of diffusants depends on the concentration of these rigid bodies. The diffusion coefficient is predicted by $D = D_0 \exp(-\alpha c^{0.5})$, where α is the parameter related to diffusant and c is the concentration of

polymer in solution. Mathematically, Altenberger's model is identical to Cukier model, but the author suggested that it is applicable to higher concentrated solution system and strong interactions between diffusants and solvents.

1.6.5.2 Phillies' Model

To study self-diffusion of large size polymer molecules in solution, Phillies reported a model based on experimental data in wide range of concentrations [89]. The self-diffusion coefficient of polymer molecules is described by

$$D = D_0 \exp(-\alpha c^{\nu}) \tag{16}$$

where α and ν are scaling parameter that considerably depend on the molecular weight of diffusant. Since system concentration has great influence on self-diffusion coefficient, three concentration regimes have been taken into account in the study. The first regime is dilute solution where polymer molecules are able to move independently; the second regime is represented as semi-dilute solution in which polymer chains are overlapped and hydrodynamic interaction occurs; the last regime is regarded as concentrated solution where driving force of diffusion is dominated by frictional interaction between polymer and solvent. In addition, in Phillies' model, molecule weight of polymers is defined as critical factor that affect diffusion process. Therefore, for macromolecules, $\alpha \sim M^{0.9+/-0.1}$ and $\nu \sim 0.5$; for small molecules, $\alpha \sim R_h$ and $\nu \sim 1$. In between $\nu \sim M^{-0.25}$. Phillies model seems to be similar to Cukier model, but the difference between each other is that in Phillies model, polymer chains are characterized to be mobile and ratable, and polymer chains consist of spheres connected by rods that can rotate and move. Phillies also pointed out that the self-diffusion coefficient is related to drag (friction) coefficient f, defined by Einstein function $D = \frac{k_B T}{f}$, where k_B is Boltzmann constant and T represents temperature. From this equation, it can be seen that increasing drag coefficient retards

the diffusion without considering temperature. Good fitness with this model has been found from investigation of polystyrenes in tetrahydrofuran (THF)-hexafluorobenzene (HFB), poly(ethylene oxide) in water and in water-dextran [89]. Similarly, the diffusion of other large diffusants in dextran gels [90], PA gels [84] associative polymers [91] and PVME gels [92] has been published. However, another paper [93] presents the deviation of Phillies model with the diffusion of PS spheres in concentrated PVME solutions. Overall, Phillies model displays high agreement in dilute or semi-dilute polymer solutions but poor agreement in high concentration solutions.

It is necessary to point out that hydrodynamic theory is also applicable in investigation of other type of diffusion, such as drug delivery. Gao and Fagerness [94] reported drug (adinazolam) and water diffusion in hydroxypropyl methyl cellulose (HPMC) with viscosity-inducing agent (VIA), such as glucose, lactose; and described the function of diffusion coefficient as $D = D_0 \exp(-K_i c_i)$, where D_0 is the self-diffusion coefficient. Ki is a proportional constant for adinazolam, which is obtained by linear least square fit of the diffusion from binary systems. For instance, $K_{glucose}$ is observed from the diffusion of glucose-water binary solution; c_i is the concentration of VIA. Gao and Fagerness model is quite similar to these equations based on hydrodynamic theory, even though the authors did not rely on hydrodynamic arguments.

1.6.6 Models Based nn Free Volume Theory

Free volume is referred as the volume in polymer systems that is not occupied by matters. The formation and characteristics of free volume in solutions is affected by the presence of specific diffusant, solvent and polymer, but in general, creation of free volume increases the diffusion rate. Based on the free volume theory, the diffusion process is dominated by free volume existing in the polymer system.

1.6.6.1 Fujita Model

This is the firest diffusion model based on free volume theory [96]. It is derived from the investigation of a ternary system including solvent, polymer and penetrating molecules (plasticizer), but the plasticizer concentration remains low. Therefore, the system can be regarded as a binary system, consisting of a polymer and solvent. The probability of holes whose size is equal or larger than ν*, P(ν*) can be estimated by

$$P(\nu^*) = A\exp(-\frac{b\nu^*}{f\nu}) \tag{17}$$

In this equation, A is constant, b is a numerical factor of the order of unity, fv is the average free volume molecule, and thus bν* represents the measure of holes of size ν* required for diffusant displacement B. The probability P(ν*) can also be interpreted by the diffusant mobility, so that Eq. (17) can be rewritten by $m_d = A\exp(-\frac{B}{f\nu})$, where B depends on diffusant size only. The diffusion coefficient is defined in terms of m_d, by $D=RTm_d$, in which R is the gas constant, T represents temperature, respectively. Finally, the diffusion function can be addressed by

$$D = A\exp(-\frac{B}{f\nu}) \tag{18}$$

There are many successful applications of Fujita's diffusion model. For example, gas diffusion in polyethylene membranes as the penetrant volume fraction is less than 0.2, can be excellently curve-fitted by Eq. (18) [96]. In addition, self-diffusion of ketone and ester solvents in PMMA solutions can be described using Fujita model [97]. But there exists deviation from this model reported by Xia and Wang [98] that Fujita's model is valid only for low polymer volume fractions.

1.6.6.2 The Model of Vrentas and Duda

To expand the application of Fujita's model to concentrated polymer solutions and take temperature variation into account, Vrentas and Duda develoed a diffusion model for the binary polymer system with respect to solvent diffusion in polymer network, where

$$D = D_{01}\exp(-\frac{E}{RT})\exp(-\frac{\omega_1\hat{V}_1^* + \omega_2\xi\hat{V}_2^*}{K_{11}\omega_1(K_{21}-T_{g1}+T)/\gamma_1 + K_{12}\omega_2(K_{22}-T_{g2}+T)/\gamma_2}) \quad (19)$$

D_{01} is solvent self-diffusion coefficient, E is the activation energy for a solvent jump, ω_i is weight fraction of component i, $\hat{V}_i^*$ is the specific volume needed for a jumping unit of component i, ξ is the ratio of the volume of solvent jumping unit to that of the polymer jumping unit, γ_i is the overlap factor for the free volume for pure component i, T_{gi} is the glass transition temperature of component i, K_{21} and K_{22} are the polymer free volume parameters, K_{11} and K_{21} are the solvent volume parameters and, represented by

$$K_{11} = \hat{V}_1^0 T_{g1}[\alpha_1 - (1-f_{H1}^G)\alpha_{c1}] \quad (20)$$

$$K_{21} = \frac{f_{H1}^G}{\alpha_1 - (1-f_{H1}^G)\alpha_{c1}} \quad (21)$$

where α_1 is the thermal expansion coefficient of the solvent, α_{c1} is the thermal coefficient of the sum of the specific occupied volume and the specific interstitial free volume, $\hat{V}_1^0$ is the free volume occupied by the solvent at 0 K, and f_{H1}^G is the average fractional hole free volume. Eq. (19) can be simplified in the case of pure solvent or very low polymer concentrations by the equation as follows:

$$\log(\frac{D}{D_0}) = -\frac{\omega_2\xi V_2}{2.303K_{11}(K_{21}-T_{g1}+T)/\gamma} \quad (22)$$

These paramers Kij, γ and Tgi for many organic solvents are available in the literatures [99].

A lot literatures studied diffusion coefficients by applying the model of Vrentas and Duda, such as the tracer diffusion of toluene into poly(vinyl acetate) system over a concentration range 0-96% [100], diffusion in PS [101]. Other studies demonstrated good agreements with Vrentas and Duda's model [102]. The problem of Vrentas and Duda model is the deviation to the diffusion occurring below the glass transition temperature of the polymer [99]. Another concern is that Vrentas and Duda model needs 14 independent paramenters and some of them are difficult to acquire from literatures. This limits its application to the studies of diffusion in polymer solutions to a wider extend.

1.6.6.3 The Model of Peppas and Reinhart

To have a physical diffusion model that can be used for cross-linked networks, Peppas and Reinhart [103] developed a diffusion model based on free volume theory. Their model was carried out for three types of structures: 1) macroporous hydrogels referred to pore size larger than 0.1 um in which the diffusion mechanism relies on convection. 2) microporous hydrogels defined by pore size between 20 to 500Å where the diffusion mechanism is attributed to both diffusion and convection. 3) nonporous hydrogels characterized by limited space among macromolecular chains where the mechanism of transport only depends on diffusion. Since the elastomers used in our research do not belong to porous polymers, hereby the discussion focus on the nonporous hydrogels. More information about structures 1) and 2) can be obtained in the paper [103]. In Peppas and Reinhart model for nonporous hydrogels, the diffusion progresses through the gel space not occupied by polymer chains. Therefore, the self-diffusion coefficient is proportional to the probability of moving through gel with mesh size, P_ξ, and proportional to the probability of finding the free volume in gel and solution, $P_0^{'} / P_0^{+}$, and the self-diffusion coefficient is presented by

$$\frac{D}{D_0} = P_\xi \frac{P_0^{'}}{P_0^{+}} \tag{23}$$

where D is the diffusion coefficient of diffusants in hydrogel, D_0 is the diffusion coefficient of diffusants in water. For the probability of finding the free volume in gel and solution, $P_0^{'} / P_0^{+}$, Peppas and Reinhart's paper [104] described that the diffusion of solutes through free volume was mainly with respect to water and little to polymer, so that Eq. (23) can be rewritten by

$$\frac{D}{D_0} = P_\xi \exp(-\frac{Y}{Q-1}) \tag{24}$$

where Y is a structural parameter, $Y = k_2 R_h^2$, k_2 is a constant related to polymer-water system, R_h is the solute hydrodynamic radius and Q is the volume degree of swelling for gels. For cross-linked polymer, P_ξ can be obtained by its relation to the critical mesh size M_c^*, the number average molecular weight between cross links M_c and the number average molecular weight of uncross-linked polymer M_n, built up by Eq. (24)

$$P_\xi = \frac{M_c - M_c^*}{M_n - M_c^*} \tag{25}$$

then combining Eq. (23) and Eq. (24), we get the diffusion coefficient for high swollen membranes

$$\frac{D}{D_0} = k_1 \frac{M_c - M_c^*}{M_n - M_c^*} \exp(-\frac{k_2 R_h^2}{Q-1}) \tag{26}$$

where k_1 is a structural parameter of the polymer-water system.

However, for moderately swollen since the free volume of swollen network is not equal to the free volume of the solvent, and the difference of diffusion jump length of solute between in

polymer network and in water, a modified diffusion coefficient model is provided to describe the diffusion in moderately swollen network.

$$\frac{D}{D_0} = B(\nu^*)\frac{\lambda^2}{\lambda_0^2}\exp[-\nu_s(\frac{1}{V}-\frac{1}{V_0^{'}})] \tag{27}$$

where λ^2 and $\lambda_0{}^2$ are the diffusion jump lengths of the solute in hydrogel and water, respectively, B(ν*) is the function indicating characteristic size of the space available for diffusion in membrane, ν_s is the size of solute, and V and $V_0^{'}$ are the free volumes in the membrance and water [105].

Several papers were published by Peppas [106] to present the good agreements of this model with diffusants having various sizes in various hydrogels, but he also pointed out the limititions of his model in the study of diffusion of ionized diffusants in charged hydrogels, which are probably caused by the interaction between diffusants and carboxylic groups in ionized hydrogels [107].

All the seven models with their applications and limitations are listed in form as follows, Table 2.

Models	Equations	Applications	Limitations
Maxwell-Fricke	$\frac{D(1-\varphi)}{D_0} = \frac{1-\varphi'}{1+\varphi' x}$	Small size diffusants Very dilute polymer solutions	Large diffusants Semi-dilute and concentrated polymer solutions
Mackie-Meares	$\frac{D}{D_0} = (\frac{1-\varphi}{1+\varphi})^2$	Small size diffusants Dilute and semi-dilute polymer solutions	Large diffusants Concentrated polymer solutions
Cukier	$D = D_0\exp(-\kappa R_h)$	Small size diffusants Semi-dilute polymer solutions	Large diffusants Concentrated polymer solutions
Phillies	$D = D_0\exp(-\alpha c^{\nu})$	Dilute or semi-dilute polymer solutions	High concentration solutions

Fujita	$D = A\exp(-\frac{B}{fv})$	Small size diffusants Semi-dilute polymer solutions	Large diffusants Concentrated polymer solutions
Vrentas and Duda	Eq.19--22	Various solutes Semi-dilute and concentrated polymer solutions	Numerous parameters Dilute polymer solutions
Peppas and Reinhart	Eq.26,27	Cross-linked gels or hydrogels	Non-cross-linked polymers

Table 2 Summary of the diffusion models based on different theories

If D as a function of concentration D(C) is added into the Fick's second law expression, that partial different equation cannot be solved analytically. Fortunately, there still exist numerical solutions for the complicated equation and are be able to be calculated by some commercial software like Anysis®, Comsol®.

Besides these diffusion models described above, there exist other approaches that can be used to derive the diffusion coefficient of the network, where the observed phenomena are tightly related to or caused by the diffusion or the integration of diffusion and other physics. Some of these approaches are very convenient to perform in the lab and have excellent advantages in derive diffusion coefficients. For example, Tanaka etc. developed swelling theory of cross-linked gel to describe the linear expansion kinetics of gels in water or other solvents, where the swelling process is related to the diffusion. This model will be used in our experiment to derive the diffusion coefficient of the sensing material—metal particle PDMS composite and the details will be discussed in later chapter.

1.7 Reaction in Corrosion Sensor

After discussing diffusion of species through polymer composite, it is time to observe reaction that occurs in matrix. As these molecules of corrosive species penetrate in polymer and then they collide with metal particles. If the energy of supplied by these colliding molecules is enough to break bonds of metal particles, new products can be formed. Chemical kinetics relates

the microscopic collisions to the macroscopic observation of changes of concentration. Considering a typical chemical reaction that can be described as x molecules of A react with y molecules of B to generate z molecules of C and w molecules of D, so this can be written as,

$$xA + yB \rightarrow zC + wD \tag{28}$$

In a reaction of closed and well-mixed system, the rate can be defined in terms of concentration with respect to time t,

$$R = -\frac{1}{x}\frac{d[A]}{dt} = -\frac{1}{y}\frac{d[B]}{dt} = \frac{1}{z}\frac{d[C]}{dt} = \frac{1}{w}\frac{d[D]}{dt} \tag{29}$$

where, R represents the reaction rate (moles/liter sec, moles/liter min, etc), [A], [B], [C], [D] represent the concentration of reactants A and B, and products C and D, respectively. The minus sign in Eq. 29. indicates the concentration of reactants decreases in the reaction. On the other hand, the concentration of products increases. In a certain reaction, balancing coefficient x, y, z, w are constants.

According to collision theory [108], the reaction rate is also proportional to the frequency of intramolecular collisions, and to the product of [A] and [B]. Therefore, the reaction rate can be formulated as,

$$R = k[A]^n[B]^m \tag{30}$$

where k is defined as reaction constant (sec^{-1}, min^{-1}, etc.) and n and m are called reaction order that is related to the particular species and dependent on atomic details of specific reaction mechanism. Reaction order can be obtained from experiments approaches (Chromatographic techniques or Mass Spectrometry techniques) and literature. Basically, they are determined by changing the initial concentrations of reactants and examining how that affects the reaction rates.

Combine equation (29) and (30), the reaction rate can be addressed by reactants A or B

$$R = -\frac{1}{x}\frac{d[A]}{dt} = k[A]^n[B]^m \tag{31}$$

$$\text{or } R = -\frac{1}{y}\frac{d[B]}{dt} = k[A]^n[B]^m \tag{32}$$

These equations can be solved by integration to give the concentration changes with respect to time once n and m are known. For a simple first order reaction (n=1, m=0), $A \rightarrow C$, the concentration change of [A] can be described by $\ln[A] = \ln[A]_0 - kt$, where $[A]_0$ is defined as initial concentration of A. For a second order reaction (n=2, m=0), $2A \rightarrow C$, the concentration change of [A] can be presented as $\frac{1}{[A]} = \frac{1}{[A]_0} + kt$.

Then the reaction equation can be put together with diffusion equation and the general governing equations describing reaction and diffusion process can be described as,

$$\frac{\partial C_s}{\partial t} = \nabla(D_s \nabla C_s) + R_s(C_1 ... C_n) \qquad \text{for s=1,2,…,n} \tag{33}$$

where $C_s(x,y,z,t)$ represents the concentration of species s, Ds is the diffusion coefficient and $R_s(C_1, C_2 \ldots C_n)$ is the reaction term, which is usually presented as $R_s(C_1 ... C_n) = \sum_{m-1}^{r}(k_m C_1^{\alpha_{m1}} C_2^{\alpha_{m2}} ... C_n^{\alpha_{mn}})$, where m is the reaction index, α_{mn} is the reaction order and r is the total number of reactions consuming or producing s. Some forms of equation (33) can be solved analytically, like diffusion coupled with first order reaction (decomposition, oxidation, etching, etc.). Some forms of equation (33) cannot be solved analytically so have to rely on numerical methods like finite difference method or finite element method [109].

The RD process in the composite material can be solved using above governing equation. Moreover, the 2D projections of the RD process can be displayed in Figure 16, which presents the evolution profile of RD process in composite.

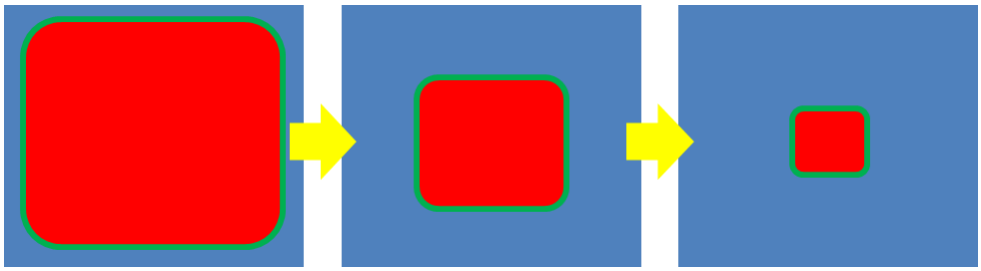

Figure 16 Evolution of RD process in sensing element

1.8 Diffusion Through Polymer Micro/Nano Composites

Diffusion through polymer composites is difficult to study due to the complex internal structure induced by the dispersion of nano-particles throughout polymer matrix. There exists no single theoretical model that is able to completely comprehend the diffusion process. Two models are generally acceptable and used in investigation. One that is derived from Fickian diffusion involves the modification of diffusion coefficient with respect to the impermeable effect of fillers. The diffusion coefficient of composite depends on the geometries of the particles (sphere, flake, rod etc.) as well as the volume fraction of particles in the incorporated polymers. These diffusion coefficients are measured experimentally according to different types of polymers and fillers. Unnikrishnan investigated diffusion through carbon black filled rubber composite and found that filled polymer showed resistance to permeation and thus had small diffusion coefficient. Moreover, he indicated the size effect of carbon black nano-particles on diffusion-- carbon blacks with smaller size have higher resistance to permeation.

Tortuosity theory is another applicable model to describe mass transport through filled polymers. Impermeable particles create tortuous paths in polymer matrix hindering penetrant molecules to travel through. The higher the particles content, the longer time penetrants take to move. Furthermore, particles occupy free volume in matrix and reduce the mobility and flexibility of polymer chains, which contribute to the impermeability as well. For example,

polymer-clay-nano-composites exhibited increased resistance to permeation as increasing the volume ratio of silicate clays attributing to the increase of tortuosity for diffusants.

There is no physical model to directly correlate diffusion in composites with filler structures and properties. Most studies focus on explaining the experimental results of mass transport in nano-composites. Drozdov examined water molecules diffusing into vinyl ester/montmorillonite nano-composites. He found that water transport of pure vinyl resin demonstrated Fickian behavior. However, with the increase of clay, the transport changed to non-Fickian. He attributed this conversion to the tortuosity induced by the clay nano-particles. Another conclusion is that despite the reduction of diffusivity resulting from the increase amount of clay particles, the mass of uptake penetrants increase with an increase of filler amount, likely caused by the affinity of montmorillonite particle for the water molecules.

Chapter 2 Objectives of Dissertation

My doctorate project topic is to develop a MEMS-based corrosion sensor using metal particle polymer composites. It includes three main objectives:

- **Investigate the microfabrication techniques for patterning micro sensors efficiently**
- **Study the diffusion behavior in the composites and obtain diffusion coefficients**
- **Characterize the electrical properties of the metal particle polymer composites**

The developed DPPOST fabrication technology makes it capable of utilization of micro/nano particles in solid state sensors, which was not perniciously possible in the MEMS. Furthermore, this technique also contribute to functionalizing polymers that was normally regarded as inert materials as active structures. An important impact of this research is regarded to the micro/nano technology, which is a popular topic among current researches (considering nano-particles, nano-tubes, nano-wires, and nano-fibers), and its application in corrosion monitoring, which is considered as a breaking through of solving corrosion inspection via micro/nano technology. The combination of embedded particle and functional polymer is promising in biological instrumentation and lab-on-chip field. The corrosion of embedded metallic nano-particles also has significance on the functionalization of body-injected particle mixtures in bio-nano technology due to the safety consideration. In addition, besides engineered application of corrosion sensor, this research also dedicates contributions on science of diffusion mechanism and theory. Speaking of the proposed applying reaction diffusion mechanism in cross-linked solid polymeric composite, under microscopic system, it represents a significant investigation toward non-well-known diffusion mechanism and its undeveloped physical models in the type of multi-phase materials. Overall it is believed that the development of this MEMS-based corrosion

sensor will pitch in preventing the corrosion impacts in monetary, life, environmental health and safety, and will also open an opportunity of insight expansion of science and technology. The technical details of each task are described below.

2.1 Microfabrication Technique to Pattern Corrosion Sensor

Based on the fully developed DPPOST fabrication and its modified technique and the capability of achieving DPPOST fabrication in our engineered micro/nano system laboratory, it is planned to develop high-yield micro corrosion sensors. Prior to use of DPPOST to pattern sensing elements, multilayers of metals have to deposit on substrate to transport electrical signals from the sensing elements to data acquisition devices, in order to monitor signal changes in real time. Then DPPOST technique is utilized to pattern polymeric composites onto metal layer and developed to achieve sensor array for the corrosion measurement. The DPPOST technique has been successfully used to develop chemical vapor sensor made up of the composite of carbon black (~40nm) and PDMS. Hereby we try to extend its application to the corrosion sensor that consists of various metal particles (a variety of metals, particle size and shape) and polymer materials. The metal particles that are planned to be employed include copper, nickel, aluminum, iron and stainless steel, whose mesh size is 325, about 44um for the maximum axial length. Also, the particle shapes change from sphere (nickel, e.g.) to flake (copper, e.g.). Both the size and shape will affect the viscosity of the composite as well as thermo expansion coefficient that will finally affect DPPOST technique. In fabrication, the DPPOST will be applied to numerous different composites and find out if the technique is applicable to pattern all these composites.

2.2 Study the Diffusion Behavior in the Composites and Obtain Diffusion Coefficients

The second objective of the research is to investigate diffusion process in microscopic composites. We will use image process approach to photo samples by short time interval.

Through curve fitting of the experimental data series, the rate of diffusion and diffusion coefficient can be determined. Due to the automation of the measurement and data processing, the diffusion properties can be achieved easily. The sample will be fabricated to disk shape so that the diameter change is measured to characterize the linear expansion which is tightly related to the diffusion coefficient.

These experimental data will be curve fitted by Tanaka's swelling theory to derive diffusion coefficient. Since diffusion is presented via concentration gradient in such a way that the concentration change takes place temporally and spatially. But careful observation will find out that the random distribution of metal particles through polymer matrix influences the concentration gradient due to the species may be trapped by these particles due to collision and/or rebound of species molecules. If that is the case, the results of diffusion rate from experiments would vary in each measurement. Therefore, one object of the project is to find if these random distributed particles would affect diffusion process and how it does so. To quantify the influence of particles in terms of their distributing density in polymer, these samples can be mixed with particles by different mass percentage. Either corroding (oxidizing) process or etching (de-oxidizing) process, which is the reversible process of corrosion, can be investigated later according to the study of diffusion.

2.3 Characterization of the Electrical Properties of the Metal Particle Polymer Composites

After completing fabrication of the micro corrosion sensor, the next task is to test its performance. The sensing principle is based on the resistance increase of the composite material in the corrosion process. Therefore, an important objective is to investigate the electrical porperties of the sensing material in order to ensure the good performance of sensor itself. The

resistance change is characterized with the increase of metal particle mass ratio in order to find the optimal mass percentage associated with measurable resistance in monitoring corrosion. Since the surface to volume ratio of the micro/nano size of the metal particles, oxide layers have been formed even before mixing them with polymer matrix, it is necessary to remove oxides of metal particles. Oxide removal can be implemented before or after mixture with polymers. The corresponding electrical properties will be tested.

Chapter 3 MEMS Fabrication Approach—DPPOST and its Modification

3.1 Introduction

Polymers are widely used materials in MEMS due to their unique properties, including high chemical inertness, high elongation ratio, surface properties, proper thermal/electrical insulation and stability, and low Young's modulus. Despite the availability of polymer materials for MEMS fabrication, patterning polymers such as silicone elastomers has remained a common problem. Silicone is resistant to reactive ion, oxygen plasma, and chemical etching techniques. It is also difficult to pattern silicone directly with photolithography without significantly degrading its high elongation ratio and mechanical compliance properties. The current methods of patterning soft polymers, like silicone-based materials, using different variations of soft lithography generally do not yield high alignment accuracies or full wafer patterning with consistent dimensional stability of the patterned features.

Huang et al. has successfully developed a robust method to pattern silicone polymer on substrate directly, which is called Direct Polymer Patterning On Substrate Technique (DPPOST). By using DPPOST, 25μm square patterns have been achieved. Other advantages of DPPOST include photolithographic alignment accuracy, a high dimensional stability, full wafer patterning, and parallel processing found in traditional MEMS fabrication. The first MEMS device—chemical vapor sensor applying the DPPOST technique has been presented and tested. In order to improve the performance of this type of sensor, miniaturization of individual sensor elements is the critical aspect.

As described by Huang et al., the DPPOST technique is parallel processing and surface micromachining compatible, while the ultimate line-width should only be limited by the lithographic resolution of the patterned materials. The percentage of complete patterns on the

whole wafer is high (~90%), but not 100 percent. Other issues experienced include lift-off sensitivity to patterns with high aspect ratios. The main reason may be the stiction between the SU-8® mold and the patterned polymer, where higher aspect ratio patterns increases such damaging stiction forces.

The focus of the current modified DPPOST work is to reduce the stiction problem. An extra deposition of Omnicoat™ (MicroChem Corp) is used to separate SU-8® and polymer patterns. The most important parameter in the modified approach is the deposition and etching rate of the Omnicoat™, which controls the thickness and roughness of the lift-off layer.

3.2 Direct Polymer Patterning On Substrate Technique (DPPOST)

The DPPOST fabrication technique is similar to the lift-off technique that is already employed in typical MEMS fabrication of metals. The key difference is that the conformally coated polymer, as oppose to thermally deposited metals, is separated from the patterning area through mechanical polishing. The DPPOST uses the SU-8® (MicorChem®) as the photo-lithographically patterned sacrificial layer for lifting-off the top coat of the conformally deposited polymer. As part of the standard lifting off procedure of the SU-8®, a thin layer of Omnicoat™ is used to act as the sacrificial layer between the substrate and the SU-8®. Omnicoat™ is an organic compound that also acts as adhesion promotion for SU-8®. It is nominally 15nm thick and can be easily removed by oxygen plasma, Remover PG®, or TMAH based developers.

SU-8® is a negative photoresist commonly used in the MEMS fabrication of microdevices. The advantages of SU-8® over other types of photoresists include high aspect ratio, hydrophobic surfaces, high dielectric constant, temperature stability, and deep robust structures. SU-8® is also

easy to spin onto a wafer and can range in thickness from <1um to >200 um in a single spin coat, depending on the specific type of SU-8® used.

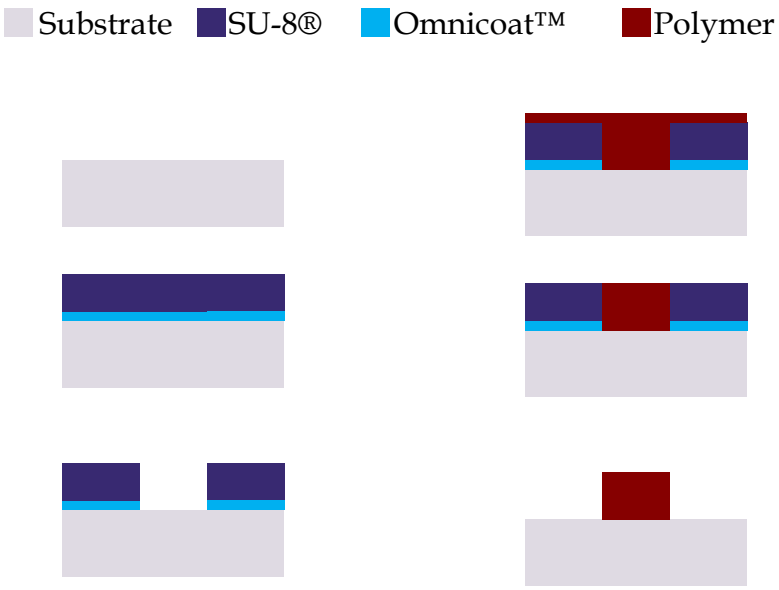

Figure 17 The process flow of DPPOST

The general process flow of the DPPOST technique is shown in Fig. 17. First, a thin dissolvable Omnicoat™ is deposited on a silicon wafer. Typically, the Omnicoat™ is spin-coated onto the wafer at a speed of 3000rpm. Then it is baked on hotplate at 200°C for 1 minute. Then, by using SU-8® 2025 spin-coated at 3000rpm a film thickness of about 30μm is achieved. The standard 2-step soft bake for the SU-8® at 65°C for one minute and 95°C for five minutes is then used prior to exposure.

To pattern the SU-8® the wafer is exposed on a Karl Suss MA-150 top-side aligner. The required total energy of SU-8® for this thickness is 150mJ/cm^2, which corresponds to 23.1 seconds of exposure at 6.5mW/cm. In accordance with the manufacturer's recommendation, a UV filter is used to eliminate UV radiation below 350 nm which eliminates cracks in the SU-8® and allows better sidewall definition. The adjustments on exposure time for using the filter and

patterning on a silicon wafer are an additional 40% and 50% respectively. The total exposure time used is thus 48.5 seconds.

After exposure a post exposure bake is required at 95°C for five minutes. The SU-8® developer composed of 1-Methoxy-2-Propanol Acetate is used as a wet etch and the wafer is dipped in the bath for approximately five minutes. If the SU-8® is not developed enough the pattern would turn white as if it were frosting when rinsed with isopropyl alcohol. The wafer is then dipped back into the developer until it is fully developed. The wafer is then etched in oxygen plasma to ash the exposed Omnicoat™, which is done for five minutes with a gas flow rate of 80sccm and RF power of 250W.

As part of the patterning process for the silicone carbon-black sensor, typically the 10:1 mass ratio of RTV615A to RTV615B, respectively, is used. Carbon-black particles with average sizes of 0.042 microns is then mixed with the silicone compound at 20% by weight and then applied to each individual SU-8® mold using a glass slide. The polymer takes approximately 24 hours to completely cure. A diamond abrasive pad is used to polish the surface of the wafer and remove the excess top coated polymer. The wafer is then dipped in a bath of Remover PG® (MicroChem®) heated to a temperature of 130°C. The remover PG dissolves the Omnicoat™ layer and allows the SU-8® layer to lift off. By applying the DPPOST technique, 25μm square patterns are obtained. Smaller patterns have also been fabricated using DPPOST.

However, sometimes the lifting-off process of the SU-8® for DPPOST has problem as illustrated in Figure 18. The figure shows an example that some parts of the element are torn off and the sidewalls are not sharp. The reason for this is that the sidewalls of elastomers stick with SU-8®. Sometimes residual SU-8® remains on the edge of patterns while parts of patterns have been stripped off after development. This is especially true when the side-walls of the SU-8® are

not properly prepared (negative side wall slopes and cracks) and the RTV615 is overly cured, which results in enhanced stiction between the elastomer and the mold. This can be avoided with well controlled SU-8® patterning and the curing of the deposited polymer. Ideally the DPPOST patterning should be designed to be more robust and tolerant of fabrication steps.

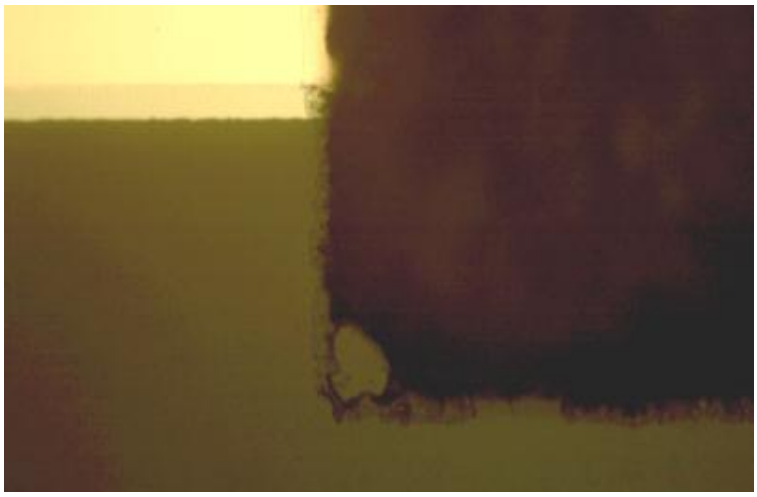

Figure 18 Example of lift-off problems at 40X magnification

3.3 Modified Approach to Direct Polymer Patterning On Substrate Technique (DPPOST)

In an attempt to correct this lift-off problem, a second method is developed to allow the silicone elastomers to adhere only to the substrate not to the SU-8®. A proposed method is to apply an extra layer of Omnicoat™ onto the pattern over the SU-8® layer. Ideally, this layer would create a separation region between SU-8® and the deposited polymer, allowing ease of lift-off.

The process flow of the modified DPPOST is shown in Fig. 19. For the procedure of modified DPPOST, the protocol of the original DPPOST is repeated until the application of the silicone elastomer material to the pattern. Instead of following with the normal DPPOST steps, an extra layer of Omnicoat™ is spun onto wafer at a 3000rpm for 30 seconds. The wafer is then baked at 200°C for 1 minute. From this point on the modified process is identical to the original DPPOST.

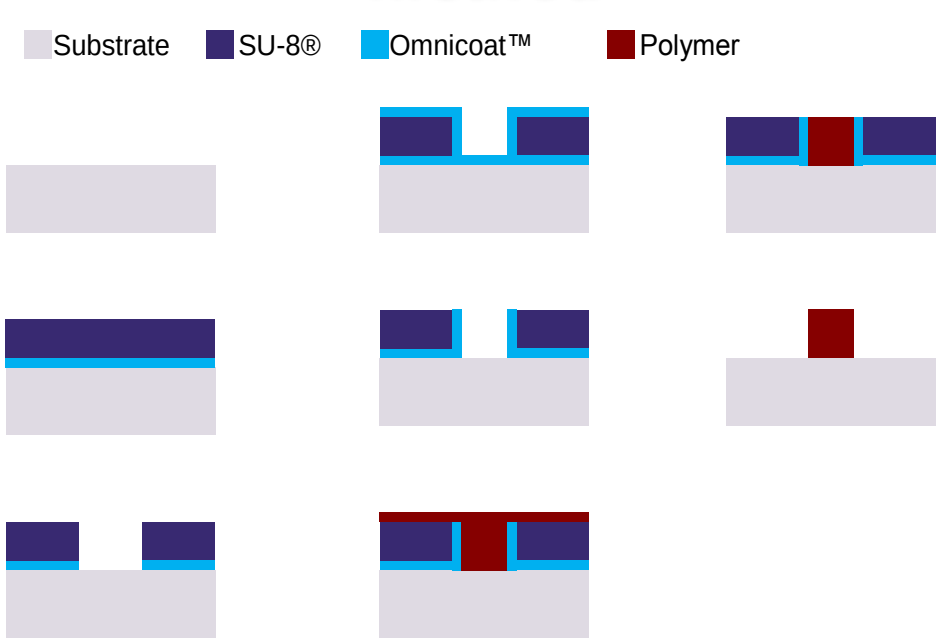

Figure 19 Process flow of modified method for the DPPOST

For effective removal, maintaining the consistent thickness of Omnicoat™ on vertical sidewall is the key to the modified approach. This thin layer not only decides the SU-8® lift-off, but also decides the conformation of patterns. In the first series of experiments, the extra Omnicaot™ layer was spin-coated onto the surface and then etched by oxygen plasma, both of which directly determine the thickness and roughness of the vertical Omnicoat™ layer; further affecting the final patterns. By spin-coat, the Omnicoat™ solution should have been deposited on the surface and covered each individual hole-pattern. However, that was not the case. Fig. 20 (top side down image, by Environmental Scanning Electron Microscope) demonstrates the cross section of 25μm width SU-8 lines patterned on substrate, with spin-coated Omnicoat™ between SU-8® patterns. The Omnicoat™ cannot fill up the hole-patterns completely while clogging up the top side. It cannot cover the SU-8® pattern surface smoothly. The reasons for this phenomenon might be the gap size is too small to be filled by Omnicoat™ solvent; or the subsequent bake step heterogeneously evaporated the Omnicaot™ inside, reducing its volume.

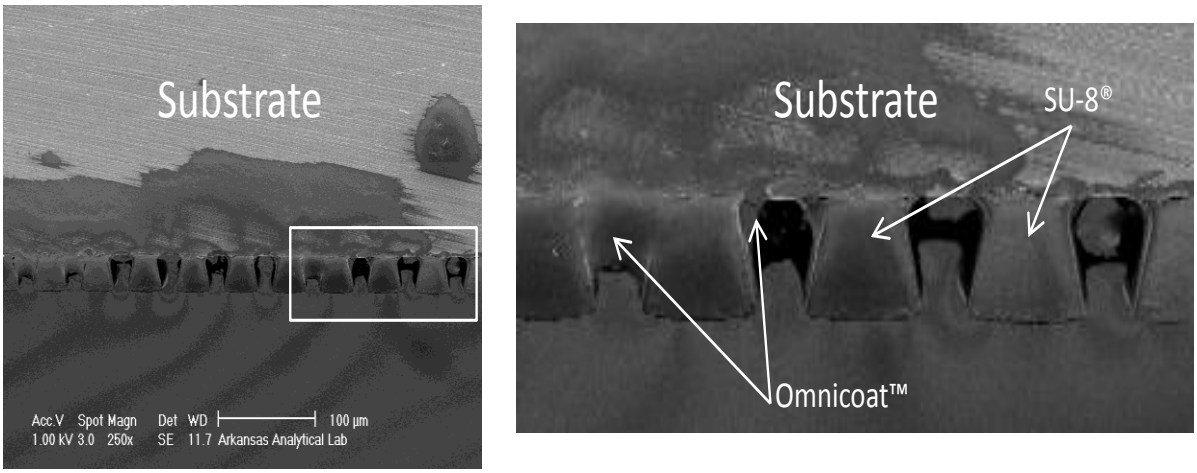

Figure 20 Cross section of 25µm width SU-8 lines patterned on substrate, with spin-coated Omnicoat™. Left: Image of cross-section of SU-8® patterns; the width of patterned lines is 25µm. Right: the magnified image of the framed area.

3.4 Oxygen Plasma Etching Rate Test

Another factor that affects the vertical layer is the oxygen plasma etching. Typical oxygen plasma etching in ashers is anisotropic (non-directional). This means that the vertical layer of the Omnicoat™ may be removed by the plasma etching step. Thus, a better knowledge of the deposition and etching process of the Omnicoat™ is required for properly developing the modified DPPOST process. Thus, an etch rate experiment is performed to find the etch rate and coating thickness of the Omnicoat™. The process flow of the test experiment is shown in Fig. 21.

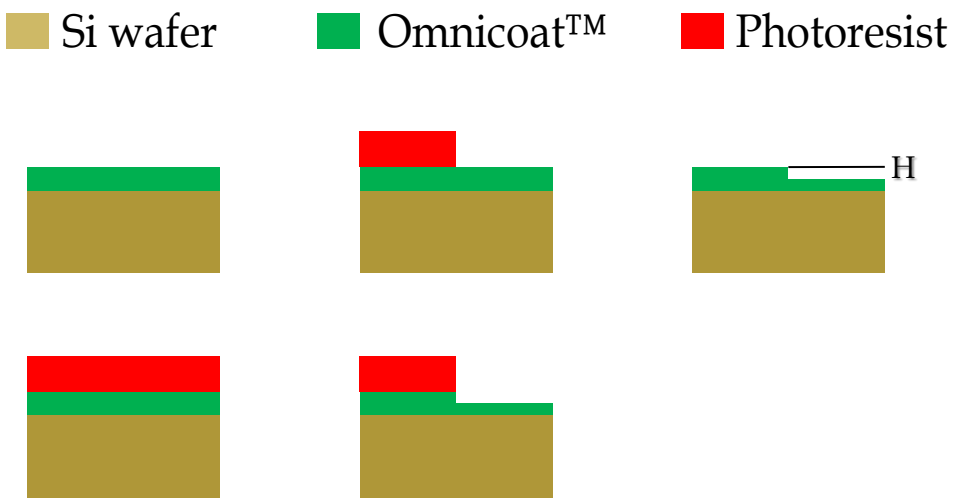

Figure 21 Process flow of testing oxygen plasma etching rate

First, we cut the whole silicon wafer into 10mm x 10mm chips by dicing saw; then spin-coat Omnicoat™ and AZ 4620 positive photoresist on each chip. The spinning speed for Omnicoat is 3000rpm; and the spin speed for photoresist is 3000rpm that allow the thickness of photoresist to be 9μm, which is much more thicker that the Omnicoat™ layer. This is used to preserve the photoresist mask during the subsequent ashing step. Then, the chips are exposed and developed to remove a half of exposed photoresist. After development, they are ashed in asher (APE 110 General Purpose Barrel Plasma Unit) sequentially with a gas flow rate of 80sccm, 450mtorr, and RF power of 250W. The etching time is set from 0.5min, 1.0min to 5.0min, 0.5 min interval. The masks for the etched chips are then stripped in acetone.

Atomic force microscope (Multimode Pico-force Mode, Vecco® Corp.) is used to measure the height difference between exposed and unexposed part of each chip. Fig. 22 shows AFM images by etching 0.5min, 2.5min, and 5.0min respectively.

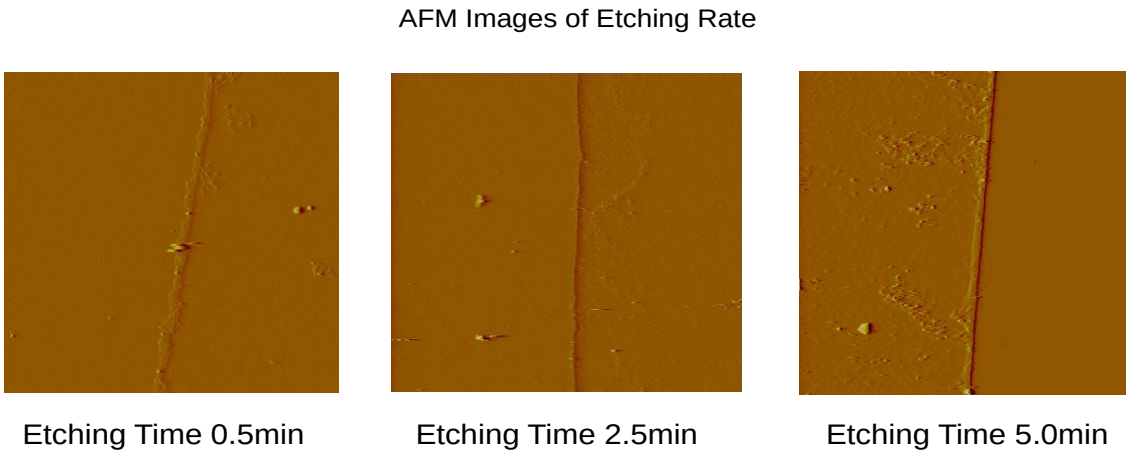

Figure 22 AFM images of chips etched by different time

Plotting the etching time versus depth, we can obtain the oxygen plasma etching rate, as shown in Fig. 23. It is demonstrated to be 2.4nm/min. the value is much smaller than expected and this may be due to the slow etch rate of the asher used (since manufacturer's specifications listed 30 seconds etch time as typical). The slope of etching rate does not pass the coordinate original point, and shifted upward. This may be due to the asher, which starts the etching timer countdown only after attaining stable plasma. Thus, the actual etching time is longer than set time. However, the etch rate should be correct since the slope is invariant of the initial etching conditions.

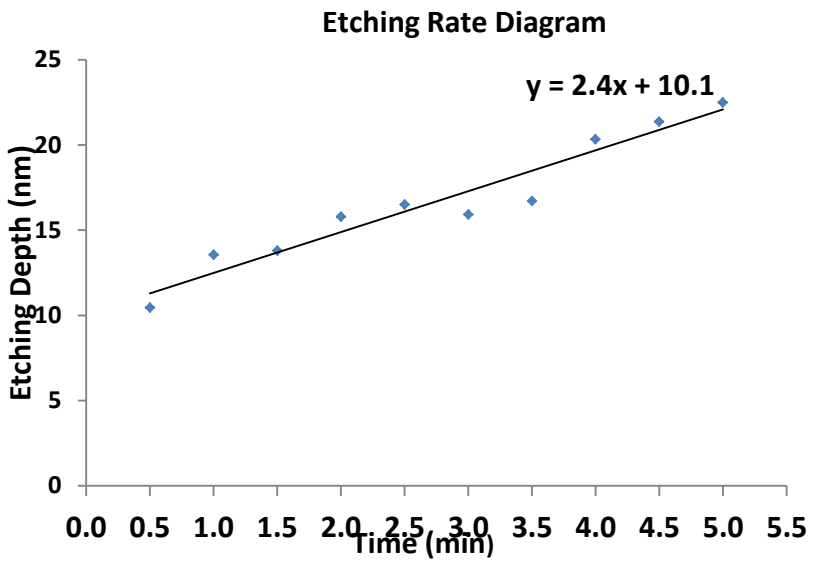

Figure 23 Oxygen plasma etching rate using APE 110 General Purpose Barrel Plasma Unit

Currently, we are repeating the experiment using RIE-based oxygen plasma to provide faster etching, better process control, repeatability, and directional etching. Fig. 24 illustrates the etching rate of the Omnicoat™ due to the RIE (Plasma-Therm SLR SERIES). For comparing with the APE110, the same setting power is used for this RIE-based asher. From the graph, the Omnicoat™ is almost eliminated in 1 minute. It shows that the RIE-based oxygen plasma provides faster etching. Key future experiments include the determination of the directional etching of the RIE as opposed to the conformal characteristics of the asher, which is needed for the improved DPPOST. Other possible side-wall preservation methods may include techniques similar to DRIE.

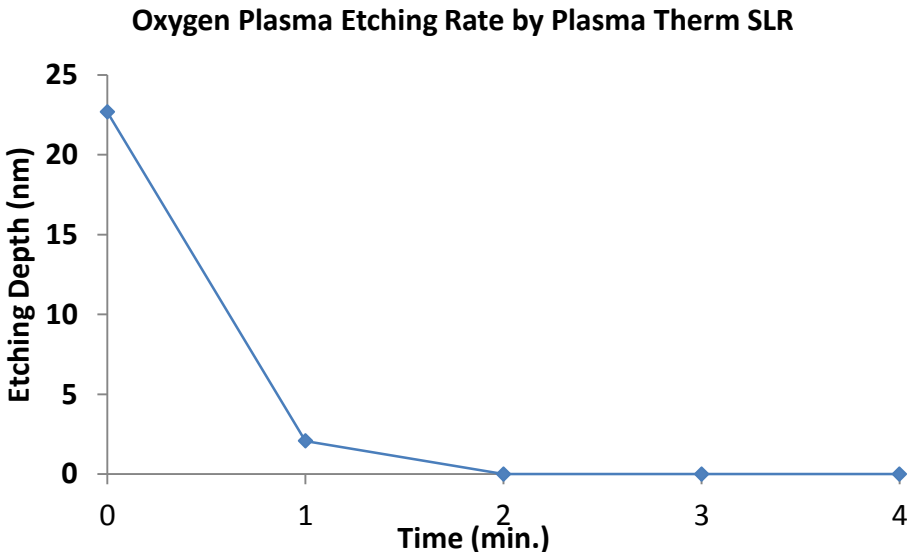

Figure 24 Oxygen plasma etching rate using Plasma-Therm SLR

3.5 Optimize the Modified DPPOST Technique

Due to the problems from spinning-coat Omnicoat™ in the modified DPPOST, two trial ways using vapor priming to deposit Omnicoat™ is currently ongoing and summarized here. Vapor priming methods often provides evenly deposited surfaces and that vapor molecule can pass through smaller gap comparing with liquid coating. It can also reduce the amount of deposited materials used. Thus, we started to investigate vapor priming system as a way to provide the required conformal second Omnicoat™ layer. The first method employs a bubbler generator connected with a flask filled with Omnicoat™. Nitrogen is bubbled through the Omnicoat™ and its vapor is carried into the deposition chamber, where it coats the wafers. The setup of vapor priming is illustrated in Fig. 25.

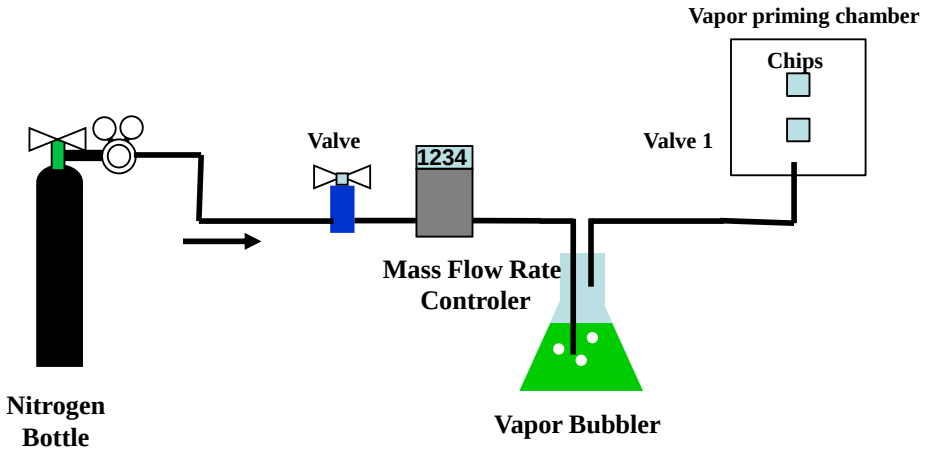

Figure 25 Vapor priming illustration

Another type of vapor priming is called thermal vapor priming, which employs an evaporated vapor from a reservoir of liquid Omnicoat™. The Omnicoat™ is heated to vapor is used to coat the wafer placed at a standoff distance above the liquid surface. The illustration is shown in Fig. 26. The chips are put on a flat surface which is totally seal in the reservoir. The reservoir is heated up to 60°C by hot plate. The temperature is controlled by a thermometer. Before the chips are put into the reservoir, they are preheated up to 120°C in order to prevent Omnicoat™ condensations on the chip. Chips are vapor-primed from 15 to 60 minutes at 15 minute intervals. A scalpel (X-acto knife) is used to scratch on the chip. The knife removes the soft Omnicoat™ polymer and provides a step for height measurements, performed using AFM.

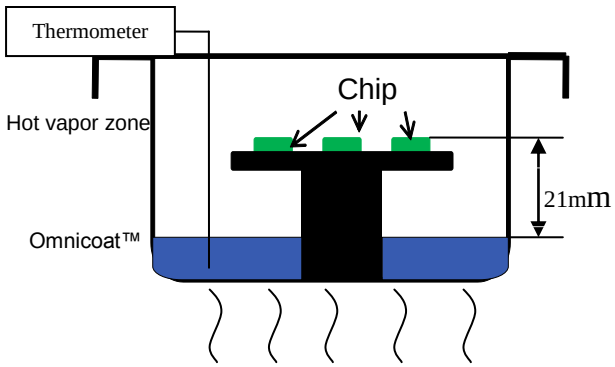

Figure 26 Thermal Vapor Priming illustration

Fig. 27 shows the thickness increment by increasing time. The growth of the thickness is very slow, even after one hour the thickness is only 5.837nm. This demonstrates that the thermal vapor priming can be applied to grow nano-films of Omnicoat™, which contributes to the deposition of Omnicoat™ on the sidewal.

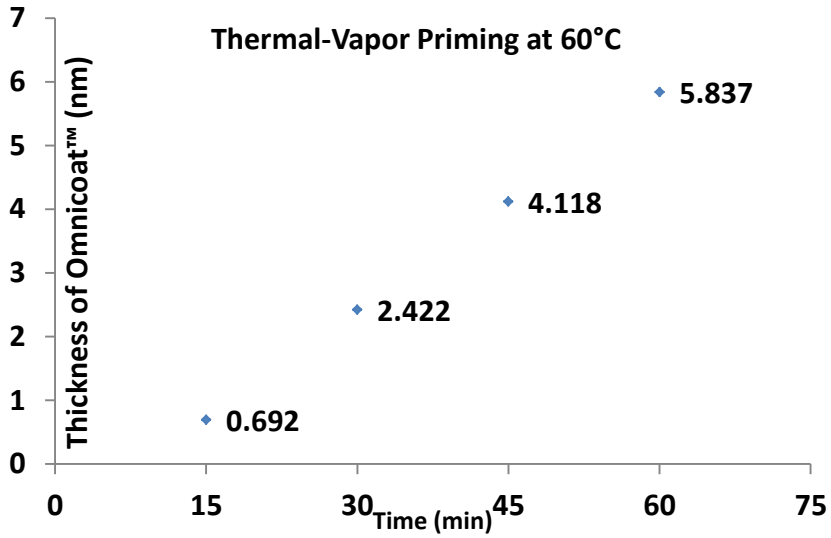

Figure 27 Thermal Vapor Priming Thickness vs. Time

3.6 Summary

This chapter presents the Directly Polymer Patterning On Substrate Technique (DPPOST) for MEMS fabrication. Additionally, the modified method of the DPPOST is also demonstrated here with the intent of improving the fabrication yield toward 100%. The modified approach requires

a double coating of the Omnicoat™, which serves as the barrier material between the substrate, SU-8®, and the deposited polymer. In order to optimize the modified DPPOST, a test of oxygen plasma etching rate has been done to provide accurate etch rate of the Omnicoat™. The etching rate is 2.4nm/min by using APE110 asher, which is smaller than expected, but most likely is due to the asher equipment used. Obviously, the RIE-based asher provides more efficient etching comparing with the APE110 asher. Thermal vapor priming to grow Omnicoat™ layer is also presented in the paper. The interesting result is that the thickness of the layer is so thin—5.8nm for an hour at 60°C in the reservoir, although the growth is relative slow.

Further work will focus on the new pattern techniques, vapor priming and thermal vapor priming, in order to obtain smooth and evenly deposited layer of Omnicoat™. Systematic experiments is needed to test the relation between deposited thickness and the mass flow rate of nitrogen for the first type of vapor priming; for the second, thermal vapor priming, the relationship between deposited thickness, the vapor priming time, the standoff location needs to be known.

Chapter 4 Diffusion and Expansion of Sensing Materials—Metal Particle Composites

4.1. Diffusion of Liquid Molecules in Metal Particles and Polymer Composites

The study of diffusion through composites of metallic particles and polymers relies on the technique that has been developed to investigate diffusion rate in composite by image processing method. The purpose of this study is to remove oxide layers of metal particles after mixed with PDMS. Due to the large surface to volume ratio of micro-size particles, they are very easy to be oxidized when exposed to air. Mixing metal particles with PDMS matrix can prevent particles further oxidization due to the isolating function of PDMS. Therefore, to remove metal oxides after mixture becomes a key in the sensor development. In addition, the oxidizing or de-oxidizing process is diffusion behavior that is a main object of this dissertation to study. The first portion of this chapter is to use image processing approach to investigate the diffusion of acetic acid through copper particle PDMS composites as well as the de-oxidation of copper particles.

The presented experiment is to investigate the diffusion of liquid acetic acid molecules through the composite of copper micro-particles and polydimethylsiloxane (PDMS) polymer, which exhibits a typical example of experimental technique accessing the diffusion study. The mesh size of the copper particle is 325, which means the maximum axial length of particle is about 44μm. Before making composite, copper particles have been etched in acetic acid (70% in volume) to remove all copper oxide surrounding particles. Since acetic acid doesn't react with pure copper, this process will not attack copper particles. All the native copper particles are rinsed by using diluted acetic acid solution (5%) and then exposed in air at room temperature for 14 days. By controlling exposure time, the oxide layer growing on particles are able to be well-defined. In this experiment, the quantitive investigation of copper oxide is not performed, but

that has been considered as an importance in the future work. After oxidation finished, the particle are ready to mix with PDMS.

In the composite, there exist copper particles 70% by mass, mixing with PDMS (Sylgard® 184 from Dow Corning Co.). In the procedure, firstly PDMS base is mixed with cross linker by mass ratio 10:1; and then the mixture is cured in 4 minutes at 80ºC in order to increase the viscosity of PDMS and prevent particle sedimentation as mixing with liquid PDMS. After PDMS well-mixed with copper particles, a 3-D printed plastic mold has to be used for the diffusion test. The mixed composite solution are then squeegeed into the plastic mold, as shown in Figure 28. The size of the groove in the middle is 6.35x2.54x2.032mm (Length x Depth x Width). A batch of these molds are completely cured in microclimate chamber (CSZ® Inc. MCBH) at 60ºC for 1 hour, then cooling to room temperature. Then each sample material is shaved across the top surface of the mold to ensure each sample having consistent height for the diffusion test.

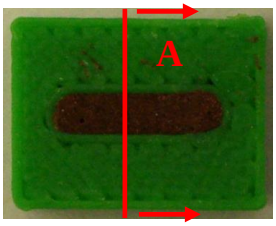

Figure 28 Sample mold with copper particle and PDMS composite;

Every four samples are submerged in 200ml 99.7% (in volume) acetic acid solution and allowed to soak at room temperature. In the soaking procedure, all solution beakers are set on a parameter-settled lab shaker for the purpose of having homogenous solution. By a predetermined time interval, 30 minutes, samples are then extracted and blown dry with nitrogen gas.

After dried, samples are cut in half by a special cutting tool, which is used to cut sample profile perpendicular to the mold top surface, Figure 29. Then four cut samples are positioned in

the spaces in the sample holder that fit the size of each sample. The sample holder, which is printed by 3D printer, with four samples is scanned by a scanner (HP Scanjet G4010) to obtain digital images of the diffusion of the composite material. The hardware resolution of the scanner is 4800X9600dpi.

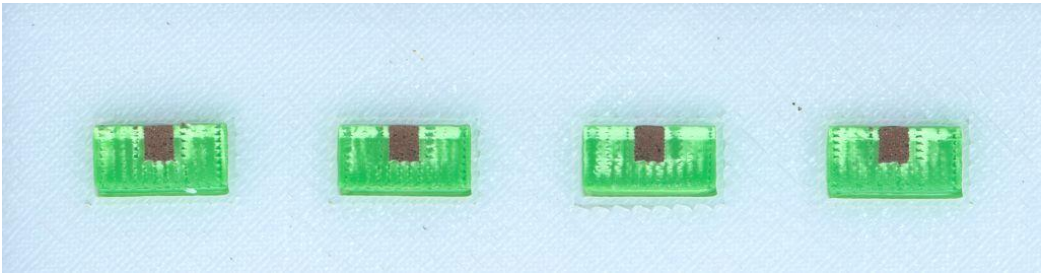

Figure 29 The scanned profiles of samples after cutting, attached with sample holder

It should be noted that as acetic acid reacts with copper (I) oxide, it removes the oxide layer surrounding the copper, leaving pure copper, which is brighter than copper (I) oxide. Due to the brighter color, copper yields a higher intensity value than that of copper (I) oxide. Therefore, from the intensity contrast, the extent of diffusion can be investigated and the diffusion rate also can be obtained from the comparison. The longer the samples are left in acid, the higher their average intensity value should be, since a larger area of copper (I) oxide is being exposed to acetic acid leaving behind just copper particles. Plotting the average values of intensity versus time yielded an upward trend as seen in Figure 30, which indicates that diffusion was occurring in the copper-polymer mixture.

All scanned images are processed within a batch-process program operated in LabView®, identifying object sections, extracting RGB (red, green and blue) information and converting images to data files based on RGB values on each pixel unit. RGB values can be indicated in terms of grayscale intensity (0~255). Each pixel in the image will be assigned three values—intensity of red, green, and blue. With the RGB color model, a value of zero occurs when no light

passes through a certain filter and a value of 255 occurs when that color is at full strength. Using the data files, graphs depicted by intensity values of RGB, for each time interval of diffusion test, can be plotted by using MATLAB®. Plotting the average intensity of each row of pixels across the width of the composite section versus the diffusion depth represents the diffusion pattern of acetic acid molecules through the composite, etching off copper oxide.

Graphs in Figure 30 show the average intensity of R, G, B versus diffusion depth by time 0.5h, 1h, 1.5h and 2h, respectively. The equation applied to do curve fitting is the non-linear sigmoidal equation 34 as listed below:

$$f(x) = b + \left(\frac{a-b}{1+\exp\left(\frac{x-c}{d}\right)}\right) \tag{34}$$

where, b, bottom value of the curve; a, top value of the curve; c, slope factor; d, width of the slope.

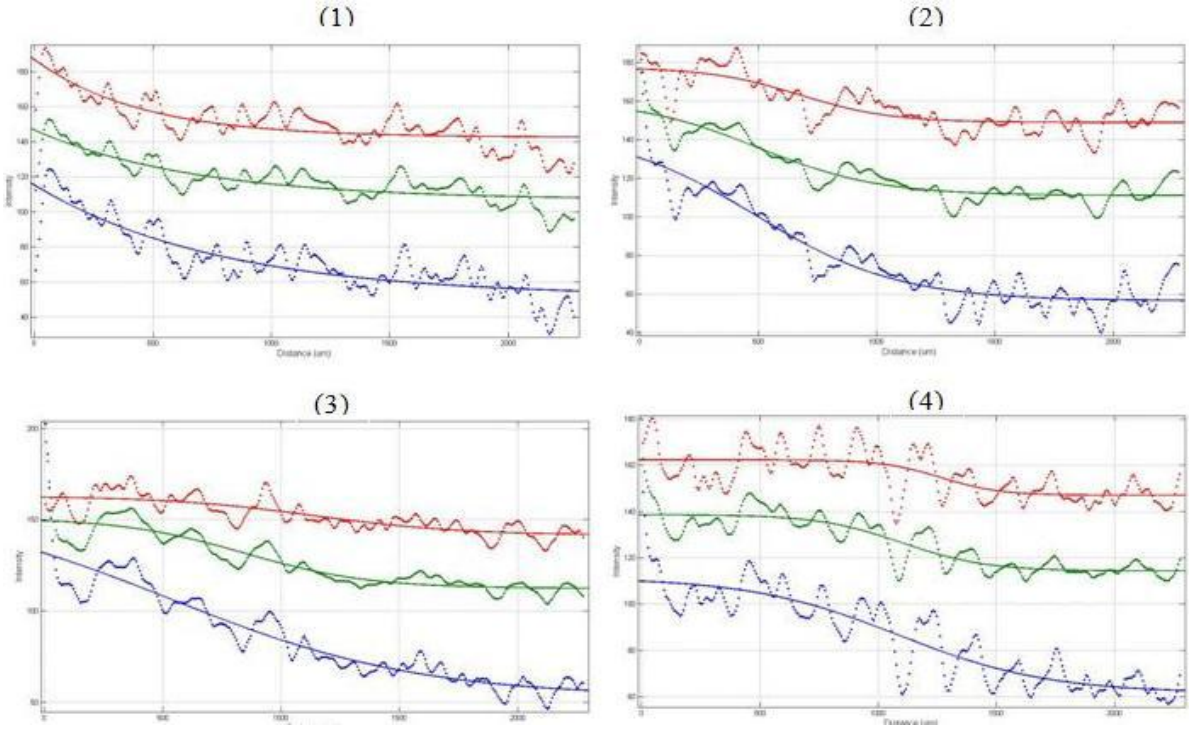

Figure 30 Intensity of Red, Blue and Green versus diffusion depth (μm). (1) 0.5h soak; (2) 1h soak; (3) 1.5h soak; (4) 2h soak

When fitted to the graphs produced in MATLAB, allows for the *c*-value to be determined, where *c* is the inflection point of the graph. Anticipating line fits, the *c*-value can be plotted against time. From that graph, a diffusion rate could be determined.

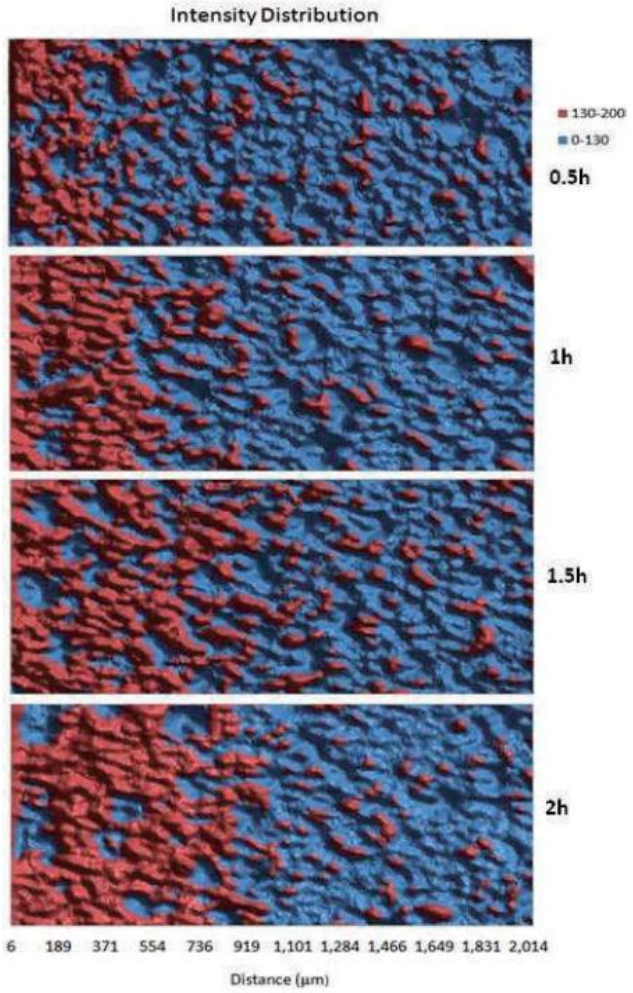

Figure 31Intensity distribution over cutting profile of samples by soak times of (1) 0.5 hour; (2) 1 hour; (3) 1.5 hours; (4) 2 hours.

A simpler approach to understand the species diffusion through the sample is to observe the intensity distribution over the sample profile. The strength of intensity can be depicted by different color mapping and height. As shown in Figure 31, picking the green intensity as an example, red color indicates intensity above 130 and blue indicates the value from 0 to 130. The finer intensity can be demonstrated be the height difference on the topography. The peaks show

higher intensity comparing to caves. The intensity distribution can be easily observed from the color contrast and topology. The interface between red and blue moves forward along x axis, which is the depth of the sample, as soak time increases. It means that acetic acid molecules flow over lager area, react with copper oxide and leaving native copper particles behind which have higher intensity value than copper (I) oxide.

From this diffusion test, it is found that the diffusive species can be replaced to other types of liquid or gas, with which the filling metallic particles can react. Therefore, the intensity contrast can be examined by image processing. Moreover, this approach can be used for not only testing diffusion rate of various species through different composites, but also removing metallic oxide layer outside of particles before using for corrosion sensing device. The advantage of this oxide removal approach, in which particles are embedded in matrix first and then remove oxide, is the polymer material can work as a barrier to prevent oxygen molecules attack particles, as they do when particles are exposed barely to oxygen filled environment.

However, there exists limitation of this approach to investigate diffusion. In the experiment, PDMS is type of non-polar polymer, but acetic acid is a polar solvent. It means that the acetic molecules cannot penetrate in PDMS well and the diffusion process into PDMS is very slow. Moreover, since the polar solvent can restrict the PDMS element, the product from the reaction of acetic acid and copper oxide are difficult to diffuse out of polymer. The obstruction can be observed from the top region of the cross section of the sample where blue and green micro-clusters attach to the structure. It is believed that they are copper ion compound clusters blocked inside of composite. These blue-green copper compounds reduce the image contrast due to their low intensity comparing to red color.

To solve the problem and diffuse out products after reaction from the matrix, an auxiliary solvent is needed to swell the PDMS and diffuse copper ions out. Some common used and most effective PDMS swelling solvents include Toluene, SU-8 Developer, IPA and Acetone. These solvents usually swell PDMS 6%—30% times in length. Furthermore, the swelling solvents also ease the diffusion process since acetic molecules transport into matrix after the expansion of matrix volume.

These swelling solvent (Acetone) also contribute to extract uncross-liked PDMS oligomers from the matrix. In mixing PDMS base with cross-linker by the ratio (10:1), after being cured, not all PDMS polymer chains are cross-linked. Certain Amount of PDMS oligomers entrap in cross-linked PDMS networks. These oligomers are concerned as contaminants, because they will influence the swelling of cross linked PDMS structure; and reduce the adhesion of PDMS to glass or silicon substrate as processing plasma bonding.

Besides swelling PDMS using solvents, expansion of PDMS also can be done by supercritical carbon dioxide ($scCO_2$), which is a promising approach to dryly swell non-polar polymer materials such as PDMS. There are many advantages of employing $scCO_2$. In particular, carbon dioxide is non-toxic, nonflammable and has a threshold limit value of 5000ppm at 25°C. Moreover, carbon dioxide is cheap and widely available, and has a mild critical temperature (Tc = 31.1°C) and pressure (Pc = 73.8bar), as shown in its phase diagram in Figure 33.

The novel scanning image approach is applied to the study of diffusion through metallic particle and polymer composites, which offers a technique with better resolution and accuracy of measure of corrosion. But this approach's limitations need to be overcome by assistance of addition of swelling solvents or gas ($scCO_2$).

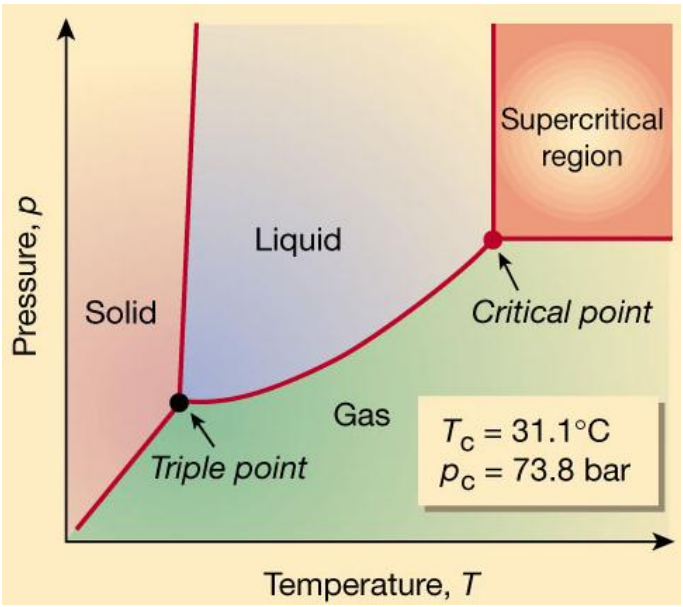

Figure 32 Phase diagram of carbon dioxide (Courtesy Zichen Qiu)

4.2. Swelling of PDMS Metal Particle Composites in Solvents

The objective of this work is to expend the volume of the PDMS matrix of the PDMS metal particles composites by using organic solvents. Then the acidic solvents that react with the specific metal oxides are added into solution to remove the metallic oxides on the surfaces of metal particles in the PDMS matrix. Due to the volume expansion of PDMS matrix penetrated by organic solvent molecules, the acidic molecules can be absorbed and desorbed into the composites by passing through free volumes that are created by the expansion of PDMS matrix. The extent of expansion of the composites in organic solvents is based on the solubility of organic solvents that is similar to that of PDMS. If two materials can be soluble, their solubility parameters must be similar. The principle of solubility can be explained by the cohesive energy theory, where the intermolecular energy must be overcome to separate the molecules of PDMS matrix to allow the solvent molecules to penetrate. Even a material that cannot be dissolved in solvent, such as cross-linked polymer, exhibits swelling behavior in exactly the same way.

4.2.1 Principle of Solubility

To understand the principle of solubility, one must realize the intermolecular stickiness in solute (in our case the solute is the PDMS matrix). The stickiness must be overcome by the solvent molecules in order to insert into solute molecules. The best way to achieve this is when the attractions between solvent molecules are similar to these of the solute molecules. Otherwise the solvent and solute are immiscible, like water and oil typically.

The stickiness between molecules actually is the van der Waals force that results from the electromagnetic interaction. The differences, in these electromagnetic interactions in the molecules--also called polarity, depend on the deviations of molecular architectures. Substances that have similar polarities tend to be soluble with each other. There are three components in the polarity (dispersion component, polar component and hydrogen bonding component) that affect the total solubility, which will be discussed late in this chapter [111].

Typically, Hildebrand parameter is the one that is widely used to indicate the solubility. Hildebrand parameter is derived from the cohesive energy density of the solvent, which is described by the equation (35).

$$c = \frac{\Delta H - RT}{V_m} \tag{35}$$

where c is the cohesive energy density; ΔH is the heat of vaporization; r is the gas constant; T, temperature; and Vm is the molar volume. From the equation, it has demonstrated that cohesive energy density is the numerical indicator that indicates the energy of vaporization of the solvent. In other words, it reflects the degree of van der Waals forces clinging molecules together. The solubility parameter is expressed by the square root of the cohesive energy density, as shown by equation (36).

$$\partial = \sqrt{c} = [\frac{\Delta H - RT}{V_m}]^{1/2} \quad (36)$$

where the unit of the solubility parameter ∂ can be expressed by $cal^{1/2}cm^{-3/2}$ or SI unit $MPa^{1/2}$. For example, the solubility parameter of PDMS is 14.9 $MPa^{1/2}$. The solubility parameters of toluene and methanol are 18.2$MPa^{1/2}$ and 29.6$MPa^{1/2}$, respectively [112]. Thus PDMS is more soluble in toluene solvent rather than methanol, which has been proved by the experiment that will be discussed later in this chapter.

Three components in the combination of the molecular interaction (dispersion force, polar force and hydrogen bonding force) contribute to the difference of solubility, while the total cohesive energy density is similar. Hildebrand parameter of the solubility has been subdivided into the three components.

The dispersion forces are derived from the random movement of the electron cloud surrounding the molecule. This random movement causes polar fluctuation that forms not permanent polar configuration but temporary dipoles that induce attraction between molecules. Therefore, the dispersion force is also named dipole-induced force. This type of force has weak attraction compared to the other two types of forces. The degree of attraction depends on the size of the molecules. For example, molecules with straight chains have larger surface area; therefore, they have greater dispersion force and thus greater intermolecular attraction, than the same molecular weight molecules with branched-chain structures.

Different with the dispersion force that is considered as temporary polar interaction, the polar force generated by the asymmetrical distributed electrons in the polar molecules, are considered as permanent polar attraction. Polar force isare stronger than the dispersion force and thus increases the intermolecular attraction. These polar molecules clung by polar forces tend to construct themselves as a head to tail form—positive at one end and negative at the other end.

The polarity of this type of molecules depends on the atomic composition, geometry and size. For example, water and alcohol are strongly polar molecules and toluene is slightly polar molecules.

Among all three solubility components, the hydrogen bonding is the strongest force that occurs in molecular interactions. The hydrogen bonding is created by the interactions between the hydrogen atoms and the electron-hungry atoms such as oxygen, nitrogen or fluorine. Because these electronegative atoms are extremely electron-grabbing, thus they draw the electrons away from the hydrogen atoms and leave the strongly positive hydrogen atoms exposed, which makes these hydrogen atoms greatly attract electrons in other molecules. The generated protonic bridge between molecules is considerably stronger than the other two types of dipole interactions. Substantially the hydrogen bonding is a type of polar forces, but it is such a strong interaction and thus has such significant contribution to solubility that it has to be considered separately from the other types of polar interaction. Even through the total cohesive energy density is similar of two solvents, the difference in their component forces, especially in their hydrogen bonding, result in the considerably different solubility. The relation between total solubility parameter and its three components can be described by the equation (37), which is called Hansen parameters.

$$\partial_t^2 = \partial_d^2 + \partial_p^2 + \partial_h^2 \tag{37}$$

where ∂_t is the total Hildebrand parameter; ∂_d is the dispersion component; ∂_p is the polar force component and ∂_h is the hydrogen bonding component. Table 3 lists the total Hildebrand parameter and the three component parameters of the solvents applied in the experiment of PDMS expansion [113]. For SU-8 Developer, it contains >99.5% 1-Methoxy-2-Propanol Acetate,

therefore we use the total solubility parameter of 1-Methoxy-2-Propanol Acetate [113], instead. But its components have not been found.

Solvent	∂_t**(MPa$^{1/2}$)**	∂_d**(MPa$^{1/2}$)**	∂_p**(MPa$^{1/2}$)**	∂_h**(MPa$^{1/2}$)**
Toluene	18.2	18.0	1.4	2.0
Acetone	20.0	15.5	10.4	7.0
Methanol	29.6	15.1	12.3	22.3
IPA (Isopropyl alcohol)	24.5	16.0	6.8	17.4
1-Methoxy-2-Propanol Acetate (SU-8 Developer)	18.8	*	*	*

Table 3 Hansen parameters for solvents at 25°C

Since the total solubility parameter of PDMS is 14.9 MPa$^{1/2}$, and is the most proximate value to the solubility parameter of Toluene, it can be expected that Toluene will swell PDMS material to the largest volume among all these five solvents. On the other hand, the ionic solvents such as hydrochloric acid, acetic acid, whose solubility parameters are much larger (due to the strong hydrogen bonding) than that of PDMS, are immiscible with PDMS. For example the total solubility parameter of acetic acid is 43.8 MPa$^{1/2}$, and makes the diffusion of acetic acid molecules into PDMS very difficult, which has been indicated in the 4.1 section. That is the reason why the PDMS composites have to be soaked into organic solvents first to make volumes expand and then the embedded metal particles are able to contact with acidic solvents to achieve the removal of oxides.

4.2.2 Experiment Setup

This experiment is to investigate the expansion of the composites consisting of PDMS and metal particles by using different solvents (the setup is shown in Figure 36). The purpose of expansion of the composites is to create the free space in the composite so that the reactive species can pass through the PDMS matrix to attack metal oxides surrounding these particles. In sensor fabrication process, this approach can be used to remove the oxide layers to reset the sensor to an initial sensing condition of zero oxide coating on the particle surface. In addition, the advantage of performing the expansion and reaction process under fluid bypasses the difficulties encountered in fabrication, where the metal particles are easily oxidized as exposed to air.

For the oxide removal—basic redox reaction, the key step is to swell the PDMS by swelling agents. After the volume expansion of PDMS, the free paths are formed in PDMS matrix so that these embedded metal particles are able to contact with etching chemicals to strip off oxide layers. Swelling agents investigated in this experiment are Toluene, Acetone, Methanol, IPA (Isopropyl alcohol) and SU-8 Developer (1-Methoxy-2-Propanol Acetate). They are all widely used chemicals in the laboratory. In addition, they are all commonly applied chemicals in MEMS fabrications. We investigated these chemicals also for the purpose of examining the degree of expansion of the composites in sensor fabrication.

A program from the Labview Vision Acquisition® would be to offer an automatic approach to capture images by controllable time intervals. All the captured images that record the expansion kinetics (diameter change) of the composites can be analyzed automatically by Labview Vision Assistant® to measure the diameter increase during the expansion. In this way, the time interval can be set to small value, even in long swelling time, the expansion kinetics can

be described precisely by plotting all the captured image data. In addition, saved images are in the bitmap format without compression ensuring the conservation of all figures displaced in the pictures.

In the experiment, five common types of micro-size metal particles (Copper, Nickel, Iron, Aluminum, and Stainless steel) are applied to mix with PDMS. Their mesh size is the same 325, which limits the maximum particle size to 44um in long axis. All the particles are purchased from Alfa Aesar®. Those particles are mixed with PDMS (Sylgard® 184 from Dow Corning Co.) in certain mass ratios (80%, 70%, 60%, 40%, and 20%). Hereby we concentrate on high mass ratio since it was observed from the preliminary tests that high mass ratio of metal particle sample can provide lower measurable resistance and thus long life span in the corrosion monitoring. Before fabricating the composites, PDMS base is mixed with curing agent by 10:1 mass ratio. Then the mixture is cured for 4 minutes at 80°C to increase the viscosity and prevent particle sedimentation during the time needed to fully cure the PDMS. After mixing PDMS with those metal particles, the gel-like composites are degased in vacuum chamber to reach the pressure 25 millitorr, in order to eliminate the air bubbles entrapped in the composites during mixing. An aluminum mold is employed to form the sheets of composites as shown in Figure 33. The ABS plastic mold is used to control the size and thickness of the composites. The size is 76x80mm and the thickness is 1mm. By tightening the bolts and nuts surrounding the aluminum mold the composite sheet can be well formed. Then the sample is completely cured in microclimate chamber (CSZ® Inc. MCBH) at 60°C for 1 hour.

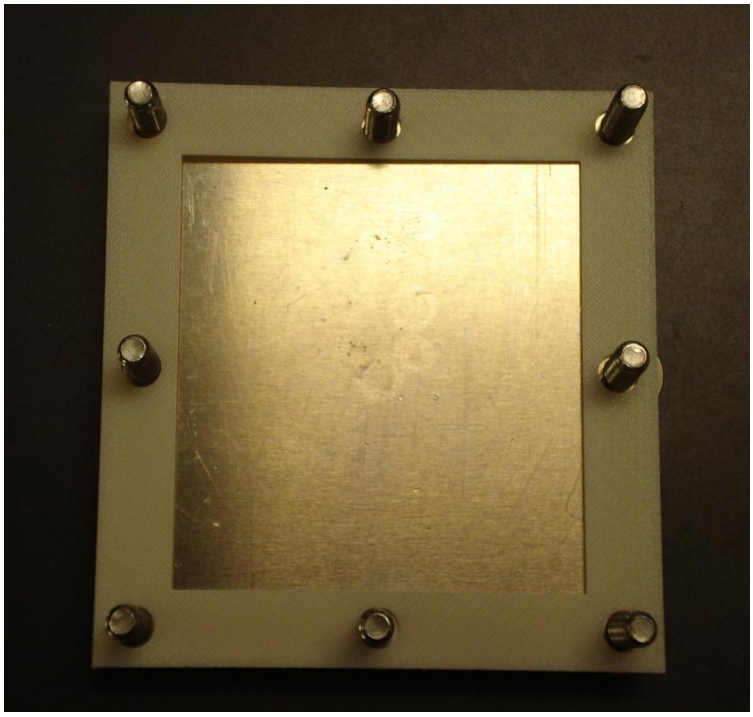

Figure 33 Aluminum mold to fabricate composite material sheets

Figure 34 (a) shows the cured nickel-particles PDMS composites sheet. After the composite sheets are fabricated, a puncher (Figure 34 (b)) with diameter 6.35mm is used to obtain a circular sample with 1mm thickness. Figure 35 shows the five types of metal particle composites with five different mass ratios (80%, 70%, 60%, 40%, and 20%) after completely curing. Then the sample is cut from each composite sheet and dipped into solvents to measure the diameter change during swelling. Figure 36 shows the experimental setup of the measurement. Samples are dipped into the beakers with pre-filled swelling solvents. For each beaker, 40ml solvent is filled up to ensure enough solvent to completely swell the sample during the experiment period. Two digital cameras (Microsoft Lifecam Cinema®) are controlled to capture images in parallel (therefore two set of swelling measurement can be implemented at the same time). The images are taken up-side-down from the bottom of the two beakers. The time interval is set to 18000ms, enough data points to describe the diameter change of the sample. The expansion test time is 4

hours for each sample in one solvent. All the parameters used in capturing images are presented in Appendix A on the back of the dissertation. The contrast is set to 50 to ensure the highest intensity difference between the sample and the transparent solvent in order to measure the sample diameter precisely. The resolution of the image taken from the camera is as high as 1280x800 pixels and all the image data are stored automatically in the computer for the further analysis. Appendix B demonstrates the Labview® program diagram and interface to achieve automatic image capture. It should be noticed that the setup is settled on an optical plate to eliminate the vibration transferred from the glove table.

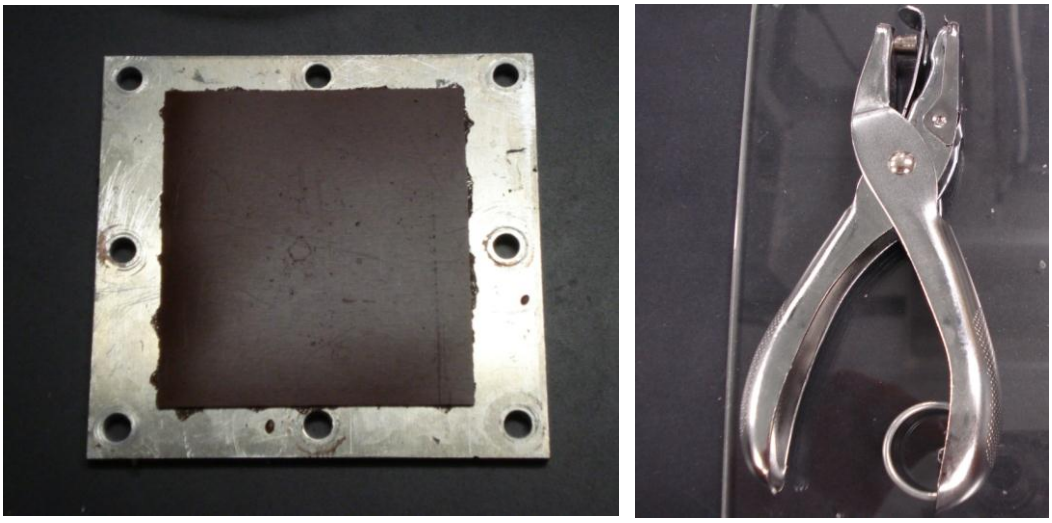

Figure 34 (a) nickel-particle PDMS composite sheet. (b) 6.35mm diameter puncher.

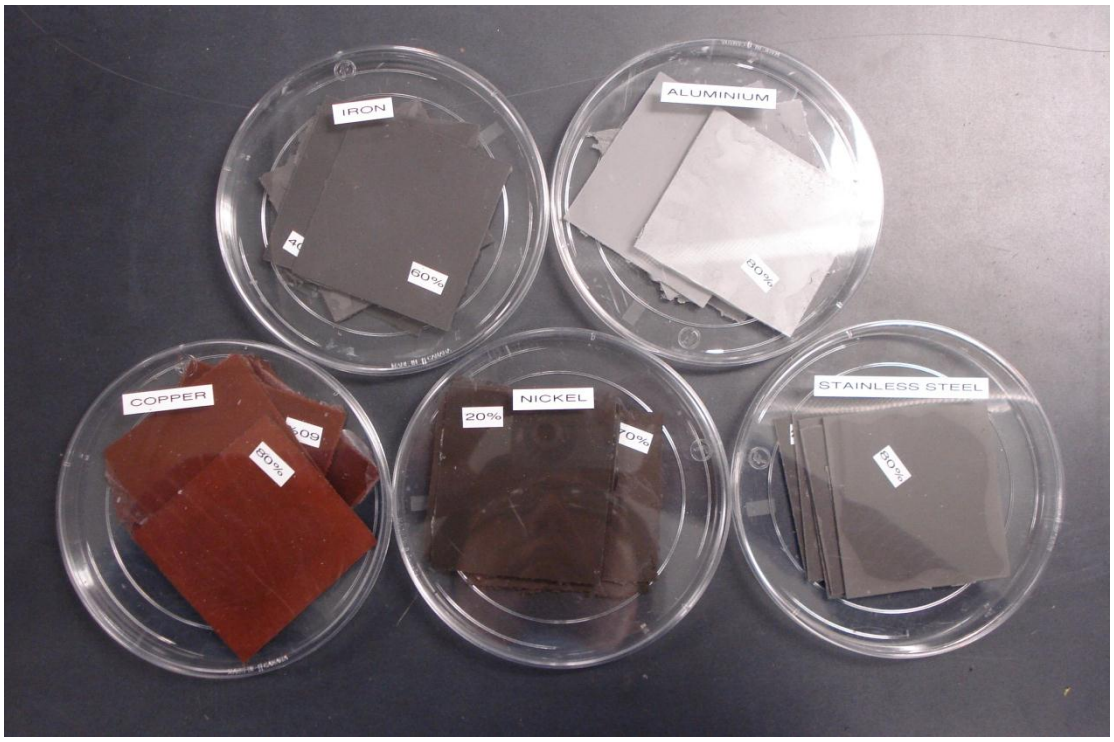

Figure 35 Five types of metal particle composites with five different mass ratios (80%, 70%, 60%, 40%, 20%)

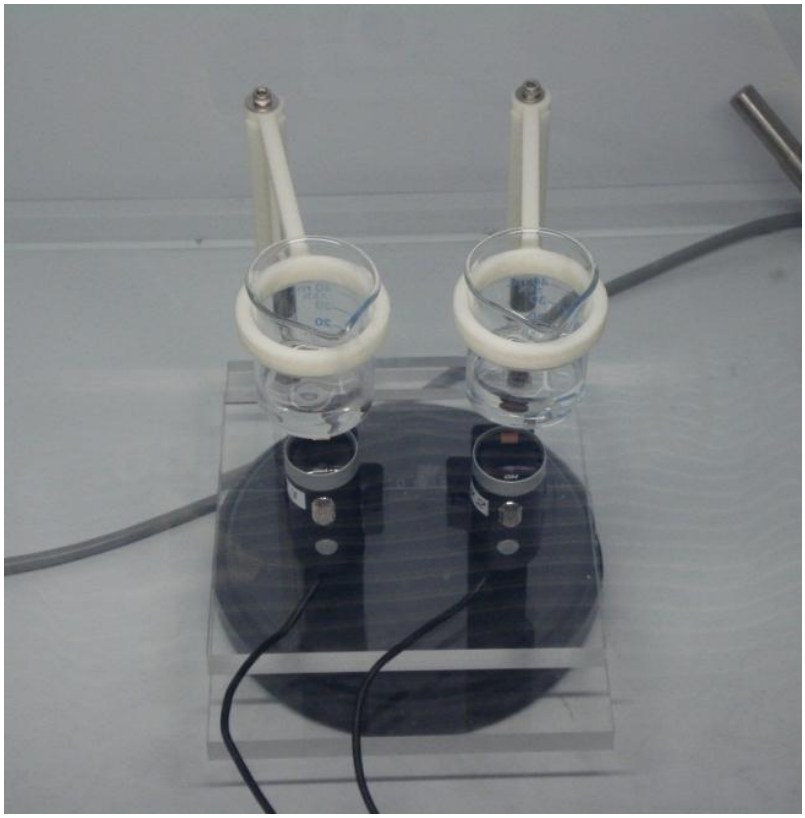
Figure 36 Expansion measurement setup and data acquisition

Figure 37 shows the captured image of 60% nickel particle PDMS composite sample in Acetone. The black-and-white image is taken from the bottom of the beaker and includes the profile of the composite sample which has intensity contrast to the surrounding transparent solvent. And the profile of the sample can be detected by Labview Vision® to obtain the measurement of the diameter. It should be noticed that the resolution of single image (in bitmap format) is high and thus even the sample diameter is relative small, the number of pixels on the sample is still in large amount (~22500 pixels), which guarantees the measurement of swelling kinetics to be in high precision (Labview Vision® can reach to the precision of 0.01 pixel).

Labview Vision utilizes the approach of step searches **to** search for the circular edge in a two-dimensional, annulus-shaped region of the sample. The region of the sample contains a number of search lines along which the step searches for sharp transitions in pixel intensities. A sharp transition typically characterizes the edge of an object in the image. The step fits a circle through the individual edge points of each search line to determine a circular edge on the object under inspection as shown in Figure 38. The first step in edge search is to select the direction property of the search lines, which selects the search direction along the lines that have the least number of obstacles between the edge of the region and the object edge. In all circular edges detection in the experiment, the search direction is to search from outside edge to inside edge of the region of the sample. Second, since the sample is dark and the solvent is bright, we set the Edge Polarity to be "Bright to Dark Only" which means that it finds only those edges characterized by bright-to-dark pixel intensity transitions along the direction of the search line. The last setting is to choose the type of edges you want to detect from the Look For control where these parameters governing edge detection have to be selected. Hereby according to the sample size and intensity contrast, we select Minimum Edge Strength—the minimum difference

in the intensity values between the edge and its surroundings—to be 10; the Kernel Size, which specifies the size of the edge detection kernel to be 3; the Projection Width to be 3 that specifies the number of pixels averaged perpendicular to the search direction to compute the edge profile strength at each point along the region of interest; and Gap to be 1 where it counts the number of degrees between search lines in the region of interest. It has to be noticed that the region of detecting edge should be larger than the sample area so that the sample can be completely included in the edge searching without losing any region of interest. Appendix C presents the Labview Vision® algorithm and its interface to implement circular edge detection and the measurement of the diameter.

After the circular edge is identified, the diameter is able to be calculated by Labview Vision in pixels. The entire calculated diameters from all the images versus their coordinated time intervals in one experiment run are saved as txt file to be ready for plotting by using Matlab®.

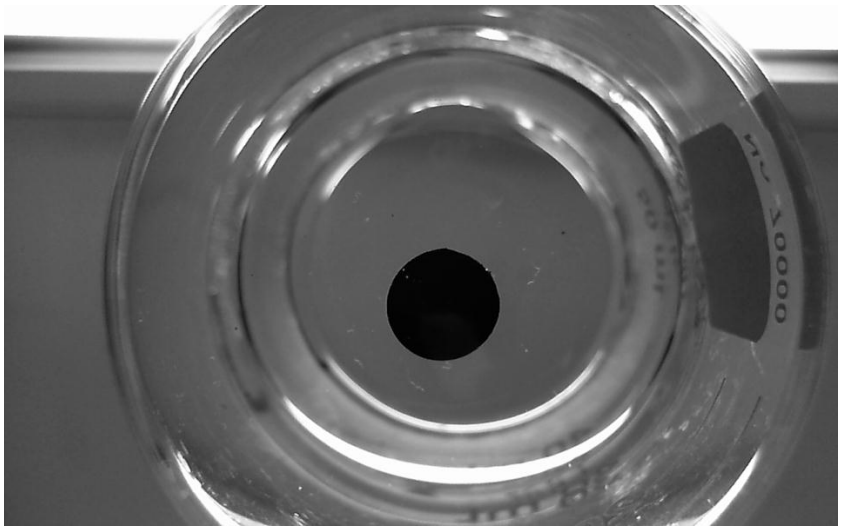

Figure 37 60% nickel particle PDMS composite sample in Acetone

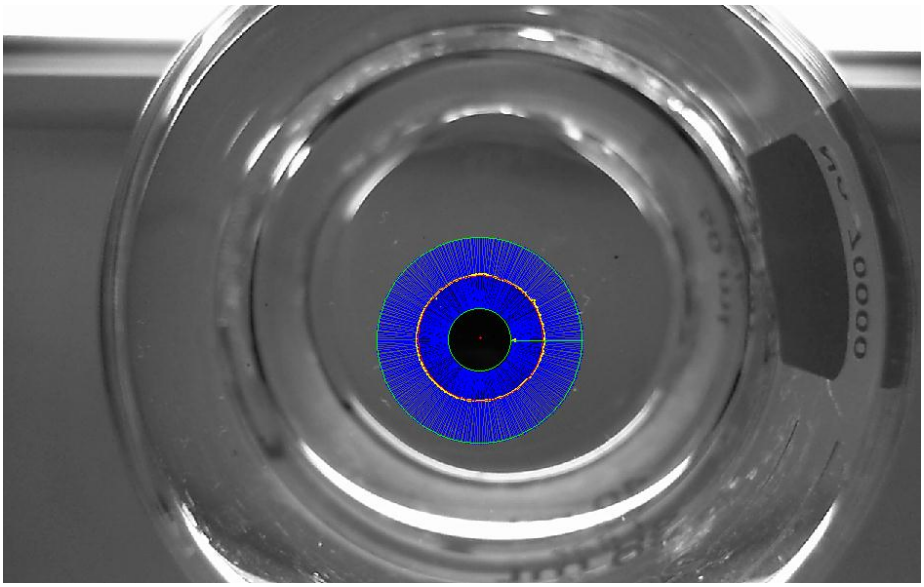

Figure 38 Circular edge detecting and diameter measurement by using Labveiw Vision®

To verify the experimental results, we first test the linear expansion of pure PDMS sample that is fabricated in the same procedures as described before without mixing metal particles. Figure 39 shows the swelling kinetics of pure PDMS in the five solvents (Toluene, Acetone, Methanol, IPA and SU-8 Developer) in 4 hours. It can be seen that PDMS swells about 32% in Toluene, which is the maximum expansion among five solvents. This value is very similar to the linear expansion value 31% observed by Whitesides [114], who measured the linear expansion of crosslinked PDMS in toluene solvent after 24 hours. The linear expansion values of PDMS in IPA and Methanol are 9% and 2.5%, respectively. These two numbers are also close to the values 9% and 2% that are obtained by Whitesides [114]. But Whitesides' measurement of PDMS expansion in Acetone after 24 hours is 6%. Our measurement of PDMS swelling kinetics is that it swells by 9% to maximum and then gradually shrinks 1.5%, to have the total swelling value 7.5% in 4 hours. The reason for this will be analyzed later in this chapter. PDMS swelling kinetics in SU-8 Developer has not been found in literatures but our measurement is 10%.

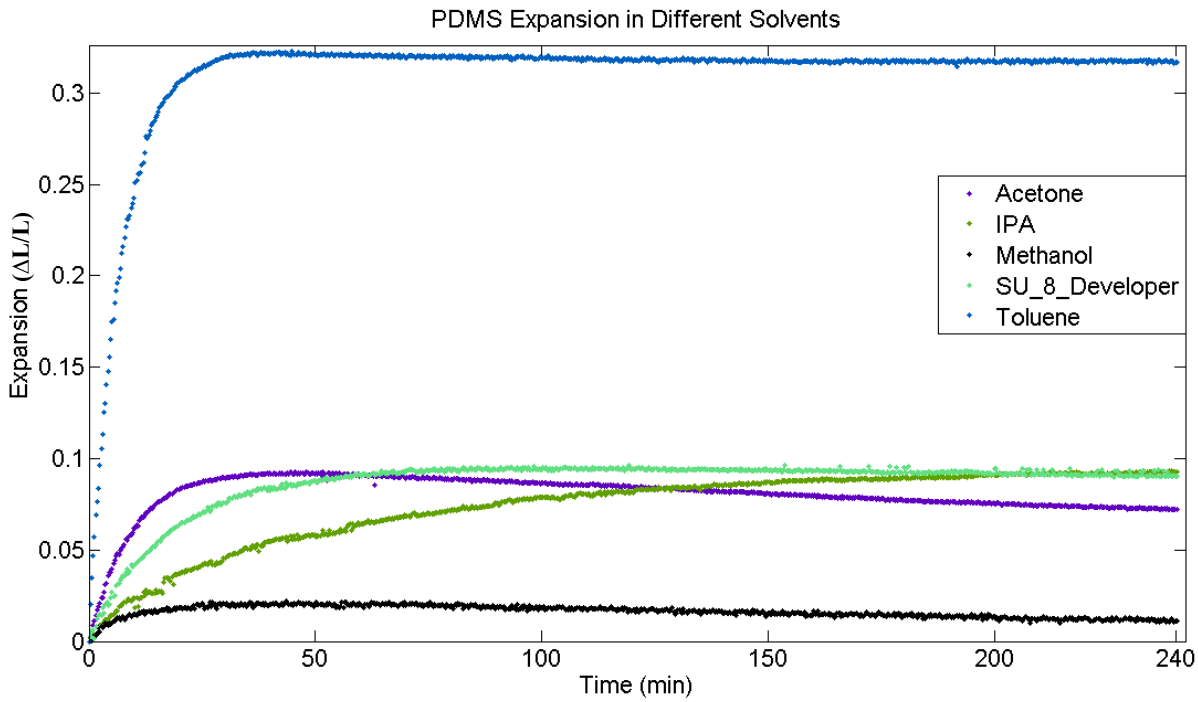

Figure 39 Swelling kinetics of pure PDMS in the five solvents (Toluene, Acetone, Methanol, IPA and SU-8 Developer)

4.2.3 Results and Discussion

4.2.3.1 Metal Particle PDMS Composites Swelling Kinetics in Toluene

Experimental results for the metal particle PDMS composites swelling behavior are shown in Figure 40 –44, as an example of figure 40 presents the stainless steel particle PDMS composites' expansion with different mass percentages in Toluene in x-y coordinate. The x axis represents the swelling time—240 min (4 hours); y axis presents the expansion, starting with the origin of (0, 0), meaning at t=0, the initial expansion is zero. To better characterize the plotted data and investigate the expansion behavior, an exponential function is utilized to fit all the curves. Since the curves are positive exponential type, the function used is a two-term exponential equation, as presented in Equation 38,

$$y = a * \exp\left(-\frac{t}{b}\right) + c * \exp(-\frac{t}{d}) \quad (38)$$

where y represents the linear expansion of the circular sample; t is time variable; and a, b, c, d are constants. It has to be noticed that the value of c should be negative due to the positive exponential curve fit. In analysis, the absolute value of c will be used for the characterization in convenience. The parameters a, b, c and d can be extrapolated from the fitted function. Mathematically, for these constants in the function, a represents the maximum value of the curve can reach; the larger value of a representing the greater the material swells. b indicates the decay of curve after it pass its peak value; the larger value of b, the slower the curve decays with time. c controls the shift of the curve along y axis. The curve move downwards with the increase of the absolute value of c. d indicates the slope of the curve. The larger value of b, the smoother (lower slope) the curve exhibits. That means it takes longer time to reach its maximum expansion. Physically b is the time constant of the swelling curve. Meanwhile, the goodness of fit is able to be justified by the R-Square, which is the coefficient of determination, statistically measures how successful the fit is in explaining the variation of the data, where a value closer to 1 indicates a better fit. The curve fitting has been done using Matlab® curve fitting tool. Non-linear least square method is applied to implement the curve fitting. This method is to approximate the model by a linear one and to refine the parameter by successive interations. Table 4 presents the R-Square and a, b, c, d values extrapolated from the curve fitting for all five types of metal particle (Al, Cu, Fe, Ni and Stainless steel) composites with five different mass percentages (20%, 40%, 60%, 70% and 80%). It can be observed from R-Square values on the table that the selected exponential function fits these data plots very well. R-Square values for all curve fits exceed 0.9. For some cases the values are even larger than 0.99 such as the curve fit for the expansion of 20% copper particle composites.

In all graphs, they show that the more particles added in the composites, the smaller linear expansion exhibits, which demonstrates that the embedded metal particles obstacle the expansion of PDMS. The reason for that is because for the identical sample volume, the more particles in the sample means less PDMS contained. Metal particles' dimension does not change in the solvent, but PDMS dose. The more PDMS network in the sample the larger it expands.

For example, for the stainless steel particle composite, the sample with 20% mass ratio demonstrates linear expansion (24.78%) almost as 1.8 times as the expansion of the sample with 80% mass ratio (14.04%). In addition, with the increase of particle mass ratio from 70% to 80%, the expansion decreases 3.05%, from 17.09% to 14.04%, comparing to the mass ratio change from 40% to 60%, where the expansion decreases 2.9% from 22.4% to 19.5%. This swelling behavior indicates that composite swelling is greatly reduced as the particle mass reaches to 80%.

The similar phenomena also can be observed from nickel particle composites (Figure 41), where the expansion decreases from 14.64% to 8.596% -- 6.044% less as the mass ratio increasing from 70% to 80%, in comparison to the expansion reducing 2.83% with the mass percentage increase from 40% to 60%. For nickel composites, the maximum expansion is obtained for the sample with 20% mass ratio, 20.6% -- 4.18% less than the maximum expansion from stainless steel composite within the same mass ratio.

Comparing to stainless steel and nickel composites, the iron composite material swells to its maximum 21.25% with the mass ratio 20% (Figure 42). Similar with the expansion behavior of stainless steel and nickel composite in the mass ratio change from 70% to 80%, where the expansion reduces most, the iron composite expansion reduces most in the particle mass ratio increase from 70% to 80%, in which expansion decreases by 3.669% (from 13.04% to 9.371%).

Iron composite swells to 9.371%, in mass ratio 80%, comparing the expansion of stainless steel composite 14.04% and that of nickel composite 8.596%.

Copper composite swells to its maximum 21.08% with mass percentage 20%, and its minimum 12.92% (Figure 43). Similar to the expansion behavior of stainless steel and nickel composite in mass ratio increase from 70% to 80%, copper composite expansion decreases 3.24% from 16.16% (mass ratio 70%) to 12.92% (mass ratio 80%).

Different from the other four types of metal composites, the aluminum composite expands smaller than other composites within all respective mass ratios (Figure 44). It swells to 19.48% at mass ratio 20%, and to 6.778% at mass ratio 80%. However, the expansion decreases most, 3.96%, in the mass ratio increase from 40% to 60%, and decreases 3.612% in the mass ratio increase from 70% to 80%.

Toluene is a type of aromatic hydrocarbon solvent. It is non-polar and has relative large molecule volume. That is reason it swells PDMS to relative large volume comparing to other four types of solvents. Since expansion is essentially the volume increase of the material, hereby we convert the mass ratio to volume ratio-- the ratio of metal particles volume to the total volume of the sample (Appendix D). Figure 45 shows the plot of volume percentages (x axis) of the five types of composites versus the maximum expansion extracted from the values of a. from Figure 45, it can be seen that with the particle volume percentage increase, the expansion decreases. For stainless steel, iron, nickel and copper particles, their volume percentages at the same mass ratio are quite close. Therefore, their maximum expansions at certain volume percentage do not vary a lot. The values of maximum expansions are close for these particles. However, this is not the case for Aluminum composite. Because aluminum has the largest volume percentage in the same mess ratio comparing to other four types of metals, aluminum

composites swell much less than other composites at the same mass ratio. This plot also explains the reason for the maximum expansion decrease associated with the mass ratio increase from 70% to 80% for stainless steel, nickel, iron and copper particle composites and associated with the mass ratio increase from 40% to 60% for aluminum particle composites. Because in these mass ratio growths, the volume percentages of particles decrease most, comparing to other mass ratio increases. For example, stainless steel particle composite's volume percentage increases by its maximum, 10.96%, at the mass ratio change from 70% to 80% associated with the expansion decrease by 3.05%. For the aluminum particle composite, its volume percentage increases most, 16.25%, at mass ratio change from 40% to 60%, associated with the expansion decrease by 3.96%. In addition, it is interesting to note that copper particles have the smallest volume ratio, but its composites do not swell to the maximum. Contrarily, stainless steel particles have the moderate volume ratio among the five metal particles, but its composites swell most. The reason for that may be due to the shape or surface area of individual particles, or the affinity between Toluene and different types of metals. But generally the composites with the similar volume percentages expand to the similar degree which is consistent with the conventional observation.

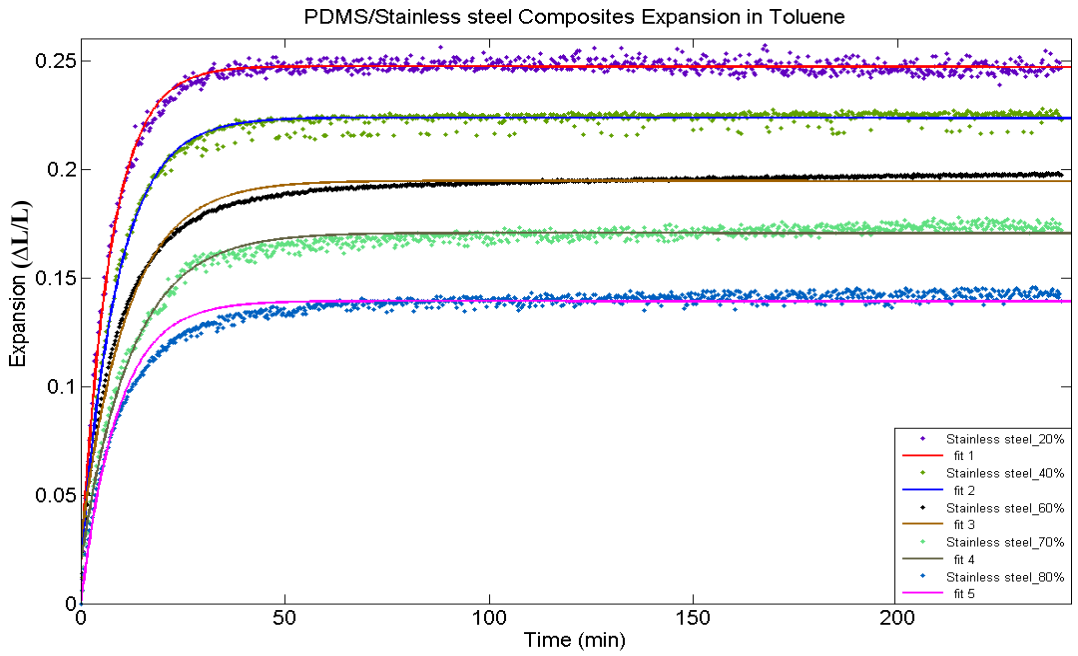

Figure 40 Stainless steel composite expansion kinetics in Toluene

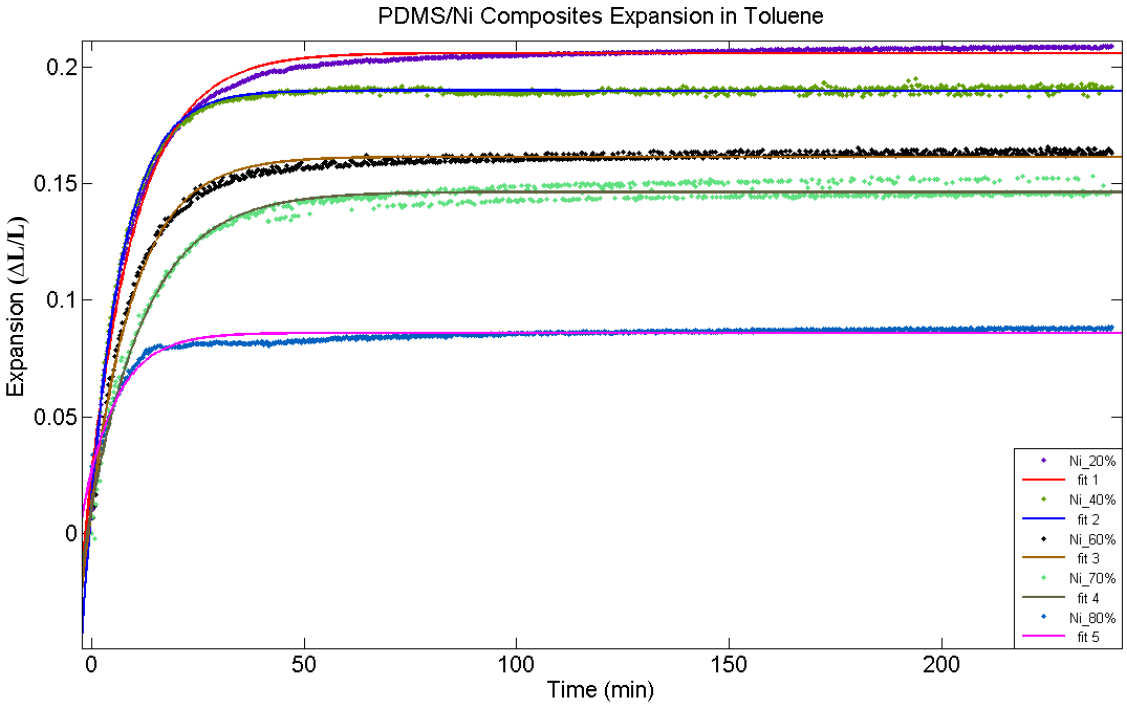

Figure 41Nickel composite expansion kinetics in Toluene

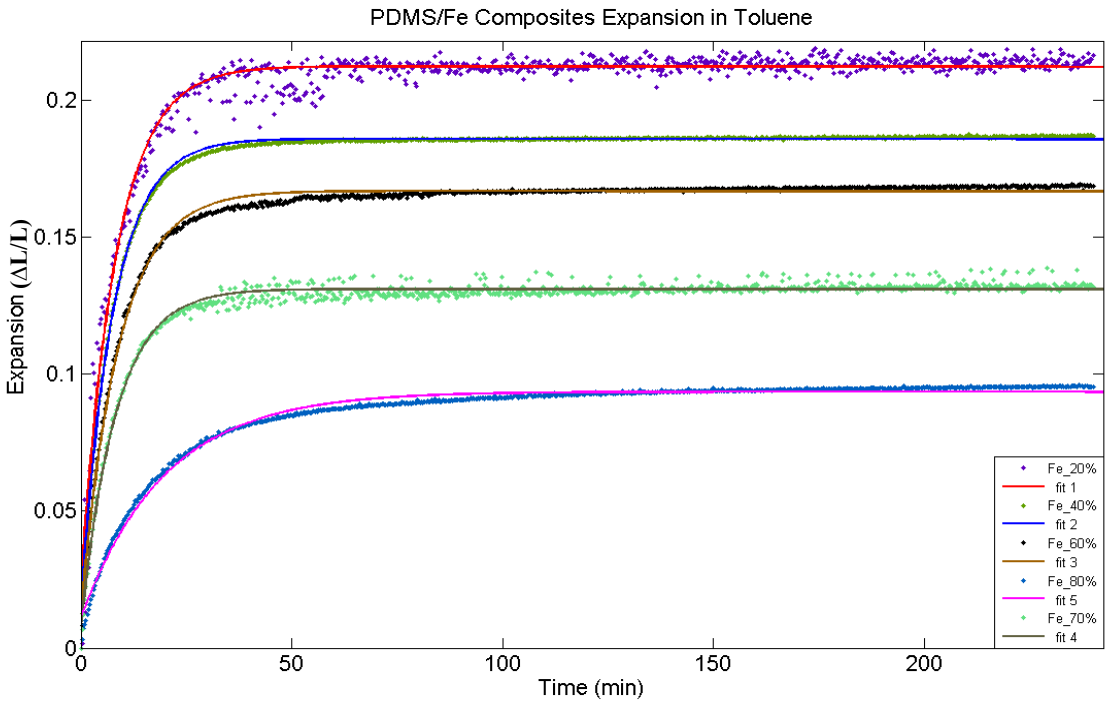

Figure 42 Iron composite expansion kinetics in Toluene

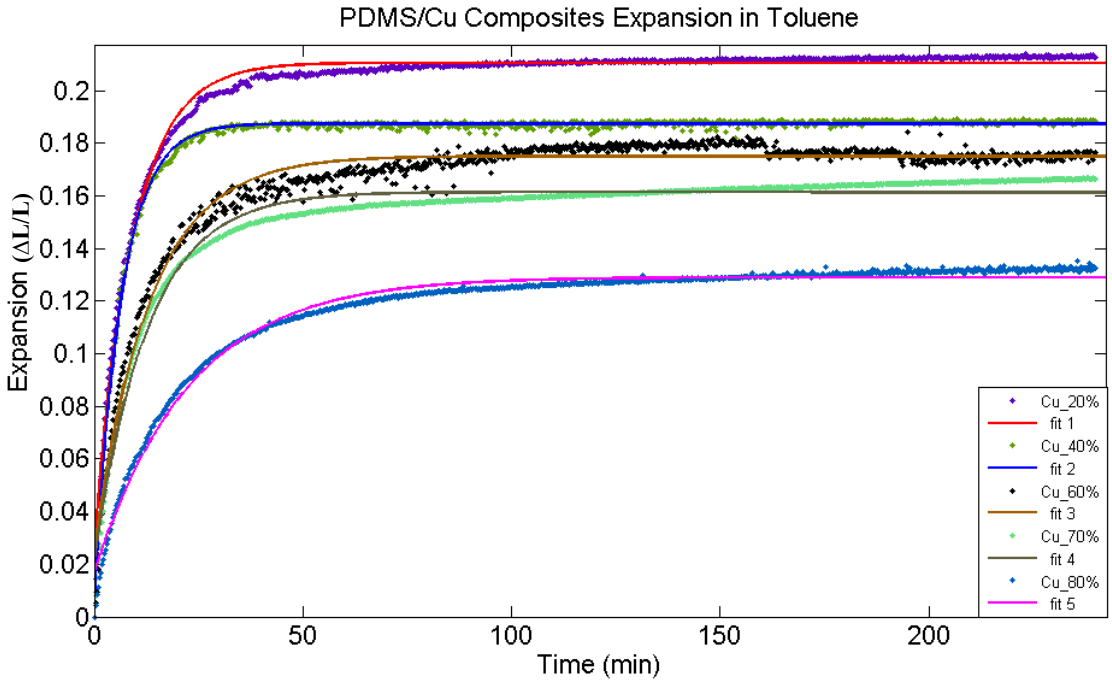

Figure 43 Coper composite expansion kinetics in Toluene

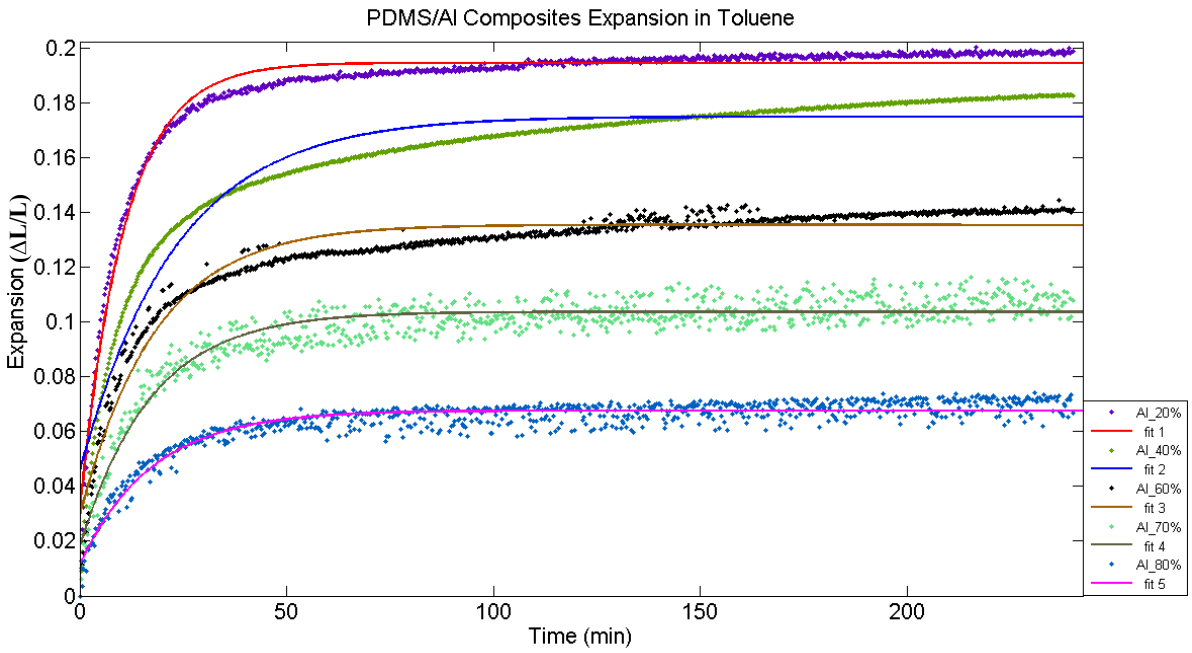

Figure 44 Aluminum composite expansion kinetics in Toluene

	Toluene				
	R-square	**a**	**b**	**c**	**d**
Stainless steel					
20%	0.9891	0.2478	134700	-0.2328	7.255
40%	0.9897	0.224	185200	-0.2083	8.775
60%	0.9865	0.195	184500	-0.1667	10.36
70%	0.9818	0.1709	205000	-0.1525	11.28
80%	0.9813	0.1404	164000	-0.126	12.81
Ni					
20%	0.9903	0.206	184500	-0.1808	8.41
40%	0.9962	0.1898	164300	-0.1753	8.921
60%	0.9896	0.1615	174300	-0.1493	10.63
70%	0.9807	0.1464	205000	-0.1356	11.29
80%	0.9394	0.08596	123400	-0.0591	6.905
Fe					
20%	0.9668	0.2125	183500	-0.191	8.241
40%	0.9974	0.1861	183500	-0.172	8.635
60%	0.9925	0.167	184300	-0.1548	8.945
70%	0.9816	0.1304	183600	-0.1142	9.283
80%	0.9881	0.09371	188000	-0.0826	19.96
Cu					
20%	0.9967	0.2108	184800	-0.1836	9.067

40%	0.987	0.1876	163700	-0.1823	10.439
60%	0.9656	0.1753	190000	-0.1491	11.45
70%	0.9737	0.1616	172000	-0.14	12.84
80%	0.9877	0.1292	155600	-0.1124	22.78
Al					
20%	0.9755	0.1948	164900	-0.1645	10.73
40%	0.9423	0.1753	164900	-0.1297	13.16
60%	0.9351	0.1357	134200	-0.1065	17.09
70%	0.8989	0.1039	124000	-0.086	17.46
80%	0.9021	0.06778	123600	-0.0563	18.18

Table 4 The R-Square and a, b, c, d values for composites in Toluene

From figure 40—44, it has been observed that after the linear expansion reaches to maximum, it will not swell further. This behavior also was observed by Teng [115], where PDMS/copper particle composite swelled in super critical carbon dioxide within controllable temperature and pressure. For all cases, the values of b in the exponential function are in the order of 10^5, which indicate that the decay is negligible after the expansion achieves maximum.

Parameter d indicates the swelling rate; the larger the value of d, the slower the sample swells. From table 4, it presents that the value of d increases with the increase of mass ratio for all cases expect the case of nickel composite in 80%. This means that the metal particles in PDMS block the swelling rate. The more particles, the slower the composite expands. Increasing metal particles not only reduces the expansion but also slows down the diffusion of penetrants since the swelling behavior is tightly related to the diffusion [117]. This point will be described later in the chapter. But hereby we use volume percentage to show the obstacle effect of composite swelling caused by the increase of particle mass ratio. Figure 46 shows the plot of volume percentages of five metal particle composites versus the inverse values of d, (1/d). In general, this figure shows that with the increase of volume percentage of metal particles, the swelling rate decreases. However, it also can be observed that the swelling rate of aluminum composite decreases much slower than other four types of metal composites. The reason may be due to the size and shape of

individual particle and their distribution within the polymer chains, which affects the diffusion pathways through the composite. Spearot demonstrated that for uncross-linked PDMS copper particle composites, the diffusion of oxygen and nitrogen decreases as the minimum spacing between the particle inclusions decreases [116]. Aluminum composites have much larger volume percentage in the same mass ratio as the other four types of metal composites and thus the spacing between particles is smaller, so the swelling ratio is much slower than these ratios in other composites. It is interesting to note that the swelling rate of nickel particle composite at 80% is much higher. This may be caused by the reduction of polymerization of the PDMS networks in mixing with nickel particles. At high mass ratio, more particles are mixed in, which reduces the encounter possibility of PDMS chains and prevents the polymerization of PDMS and thus loosens the network in the composite. Therefore, there exists more free space in the composite. In the expansion process, solvent molecules become easier to diffuse into the composite through the free space and contact with PDMS chains, resulting in higher swelling rate. But this case only occurs to the nickel composite, not for other metal particle composites, even though their volume percentages (Cu, etc.) are similar to that of nickel composite. The reason for that may be due to the affinity of PDMS polymers being weaker to nickel particles than other metal particles. Or the size of nickel particle is even smaller than the size of other particles, so the surface area that contacts with PDMS network is much larger, which leads to reducing polymerization of PDMS and thus creates free space in the bulk easing the diffusion of solvent. As shown in Figure 47, it can be observed that there exist cracks on the surface of the nickel particle composite at mass ratio 80%. These cracks mobilize the penetrants easily in the bulk composite. But these cracks do not appear on other composites even at the same mass ratio. Therefore, the swelling rate in the case of w/w 80% nickel composite is much higher.

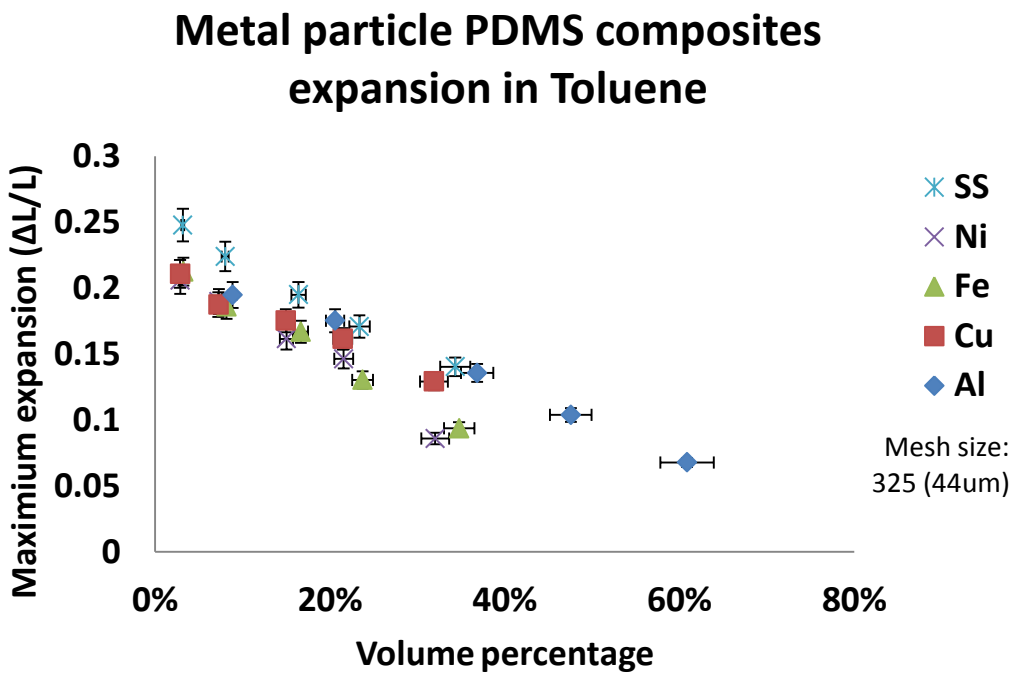

Figure 45 Volume percentages of all five types of composites versus their the maximum expansion in Toluene

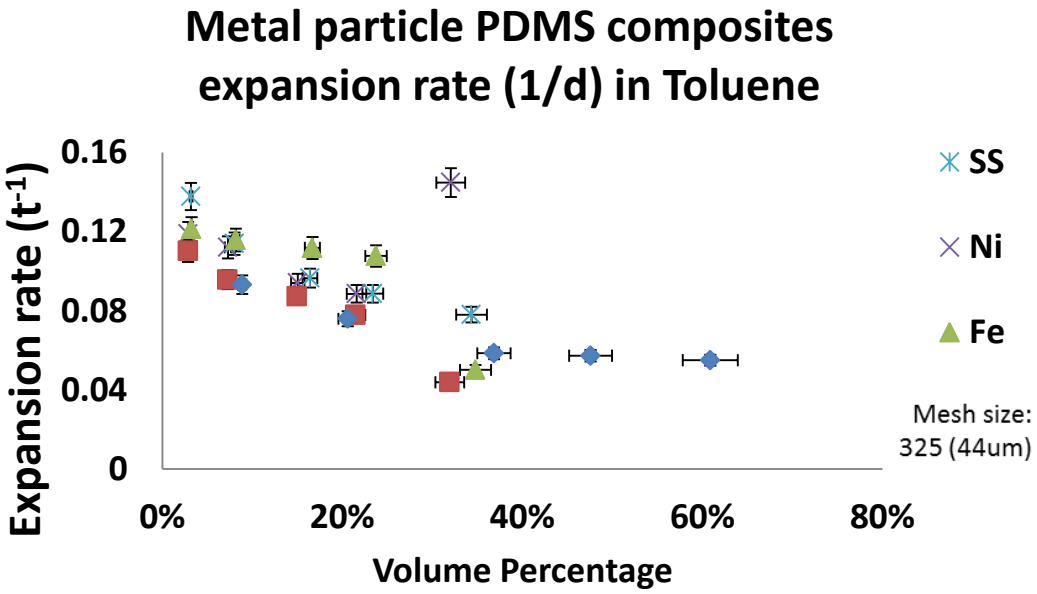

Figure 46 Plot of volume percentages of five metal particle composites versus the inverse of the value d in Toluene.

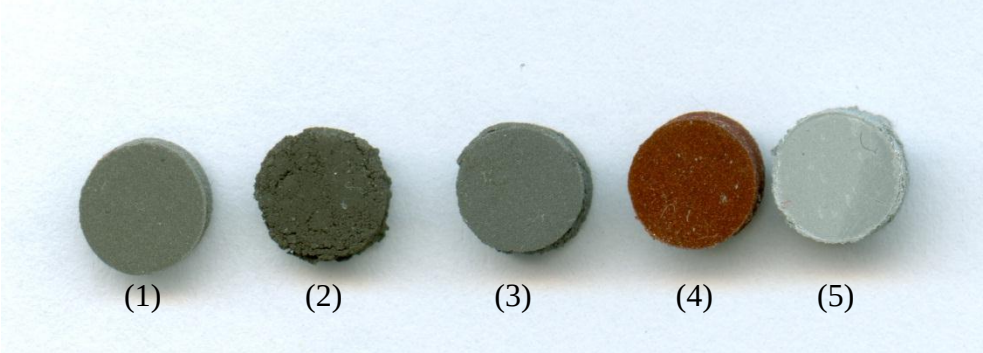

Figure 47 Free space on the surface of nickel particle composite at mass ration 80% (2), comparing to other composites at the same mass ratio (1) stainless steel (3) iron (4) copper (5) aluminum

4.2.3.2 Metal Particle PDMS Composites Swelling Kinetics in SU-8 Developer

SU-8 Developer is normally known as a stripper to etch the type of epoxy-based SU-8 photoresists. However, since it contains >99.5% 1-Methoxy-2-Propanol Acetate, it is also widely used as a solvent which has excellent solvency for a variety of substances including acrylic, nitrocellulose and urethane coating resins. It is low toxicity and soluble in water. Hereby we tested its solubility to the PDMS composites.

Same approach as to collect expansion data for Toluene solvent; and implement curve fittings (Figure 47--51), the parameters associated with the exponential function, R-Square, a, b, c, and d are obtained and listed in Table 5. It can be obtained from Table 5 that after 4 hours penetration, stainless steel particle composite expands to its maximum 8.177% at mass ratio 20%, much smaller than the maximum expansion at the same mass ratio in Toluene which value is 24.78% (Figure 47). The reason is because for SU-8 Developer, it contains acetate group whose polarity and hydrogen bonding are much stronger than those components of Toluene, whose structure is basically aromatic hydrocarbons—less polar and more soluble to PDMS, though the total solubility parameter of Toluene ($18.2MPa^{1/2}$) is similar to that of SU-8 Developer ($18.8MPa^{1/2}$). Stainless steel composite also exhibits largest reduced expansion 1.435% as the

mass ratio increases from 70% to 80%, but this reduction is smaller comparing to the reduction occurred in Toluene—the value of 3.05%, due to the lower solubility capacity of SU-8 Developer to PDMS.

Nickel particle composite's maximum expansion is 8.28% at mass ratio 20%. This value is even a little bit larger the expansion of stainless steel composite at the same mass ratio (Figure 48). However, the expansion of the nickel composites at other mass ratios are all smaller than these expansions of stainless steel composite, which is consistent with the observation from the expansion in Toluene. The larger expansion of nickel composite at 20% mass ratio might be caused in the procedure of pre-curing PDMS (to prevent particle sedimentation), where the initiation of polymerization may create some cross-linked PDMS chains that are not evenly spread throughout the sample sheet. At some portion of the sample sheet, more of these high molecular weight PDMS chains may occupy and thus less amount particles are filled in. Therefore, these parts of the sample sheet could swell more in the expansion experiment. At mass ratio increased from 70% to 80%, the expansion reduces by 2.499% from 5.624% to 3.125%.

For iron and copper particle composites, at mass ratio 20%, their maximum expansion values are 7.22% and 6.771% respectively; at mass ratio 80%, their minimum expansion values are 4.166% ((Figure 49).) and 4.257% respectively (Figure 50). While mass ratio increases from 70% to 80%, the expansion reductions are 1.411% for iron composite and 1.346% for copper composite.

Consistent with the expansion (Figure 51) in Toluene, aluminum particle composite swells much smaller than other four types of metal composites due to its larger volume percentage. Its maximum expansion is 6.586% at 20% mass ratio and its minimum expansion is 2.449% at 80%

mass ratio. At the mass ratio increase from 40% to 60%, the linear expansion decreases by 1.491%, this is the maximum expansion drop among all mass ratio changes.

From figure 47--51, it can be observed that after the linear expansion achieves its maximum value, it stops swellings. Indeed, from table 5, it shows that for the parameter b, their values are in the range 10^4~10^5. The decay is negligible after the expansion reaches maximum. Figure 52 shows the relation between volume percentage and expansion extents for the five metal particles. The higher volume percentage of metal particles in the composites, the lower the samples swell. For the parameter 1/d, plotted in Figure 53, which indicates the swelling rate, it has been realized that the value of d increases with the increase of mass ratio for all types of composites. Therefore, the swelling rate decreases with the increase of mass ratio. Another reason for this is probably that 1-Methoxy-2-Propanol Acetate contains acetate group which exhibits electronegativity and larger polarity and thus has larger affinity to metal particles, which reduces the diffusion rate of penetrants comparing to Toluene. With the increase of particles, the affinity effect becomes stronger. The greater drop can be seen on the high volume percentage. The exception is for the nickel particle composite in 80% mass ratio, where its b value is 9.806, much lower than other b values of nickel composites. Thus its swelling rate is relatively high. This phenomenon is consistent with the expansion case in Toluene and the reason has been presented above. Similar to the expansion in Toluene, aluminum particle composites swell slower due to their larger volume percentages within the same mass ratio as other metal particle composites. In general, the swelling rate of these composites in SU-8 Developer is lower than the swelling rate of the composites in Toluene, which can be seen from Figure 46 to Figure 53.

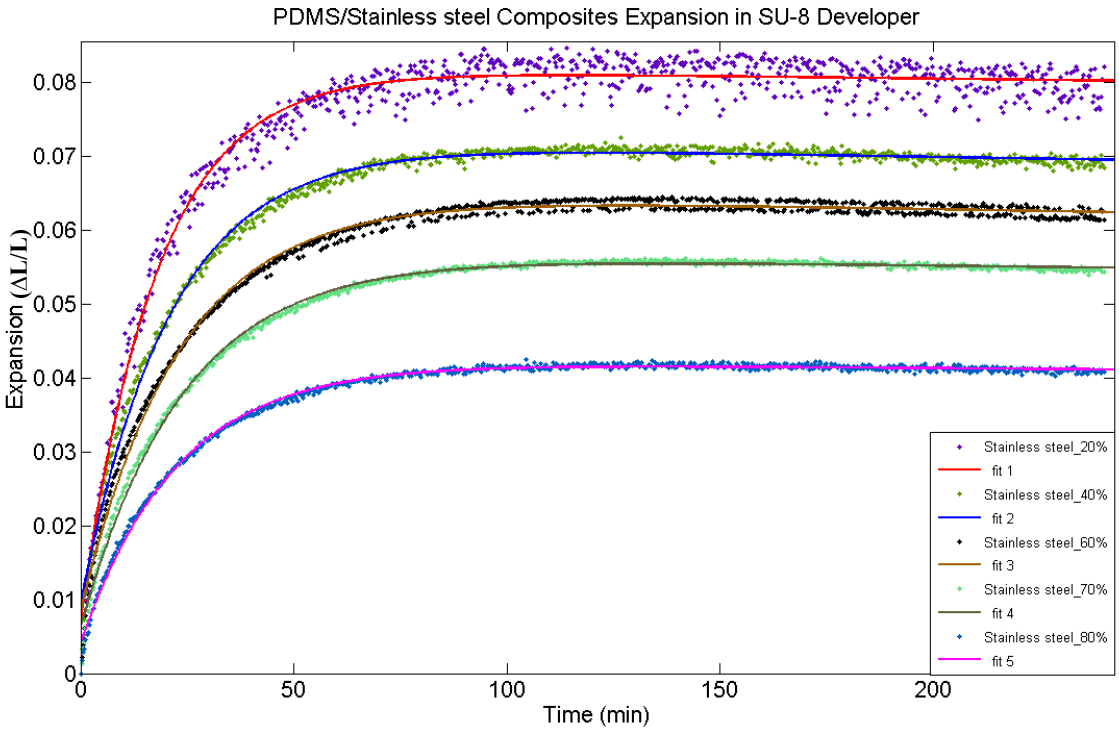

Figure 48 Stainless steel composite expansion kinetics in SU-8 Developer

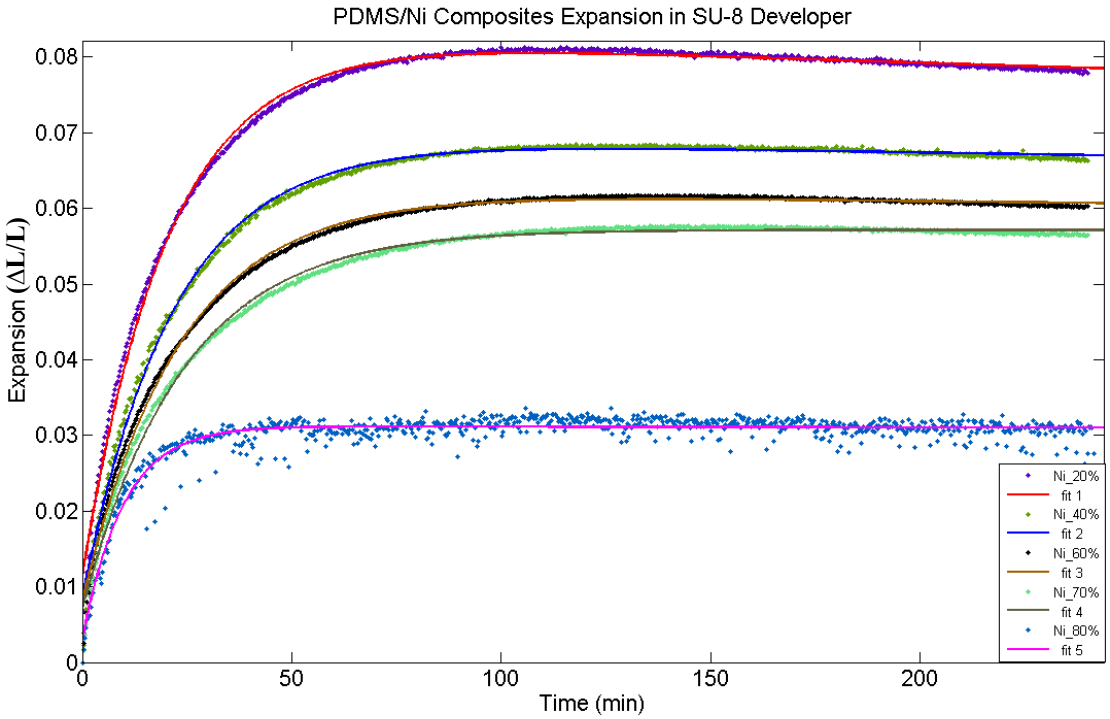

Figure 49 Nickel composite expansion kinetics in SU-8 Developer

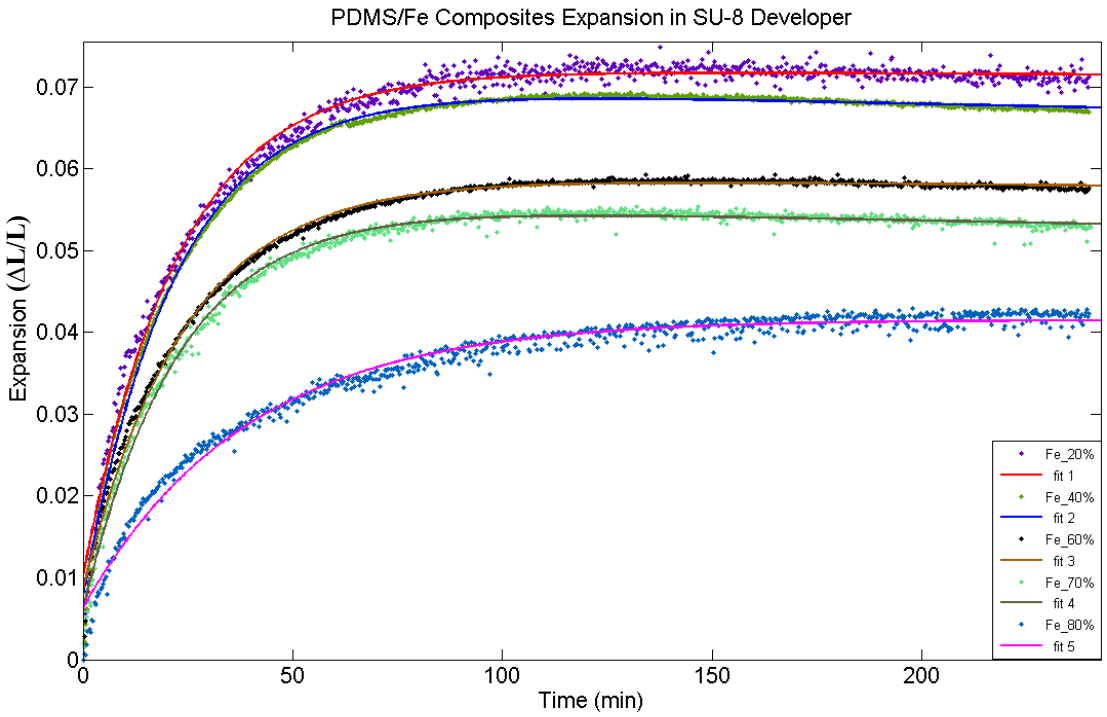

Figure 50 Iron composite expansion kinetics in SU-8 Developer

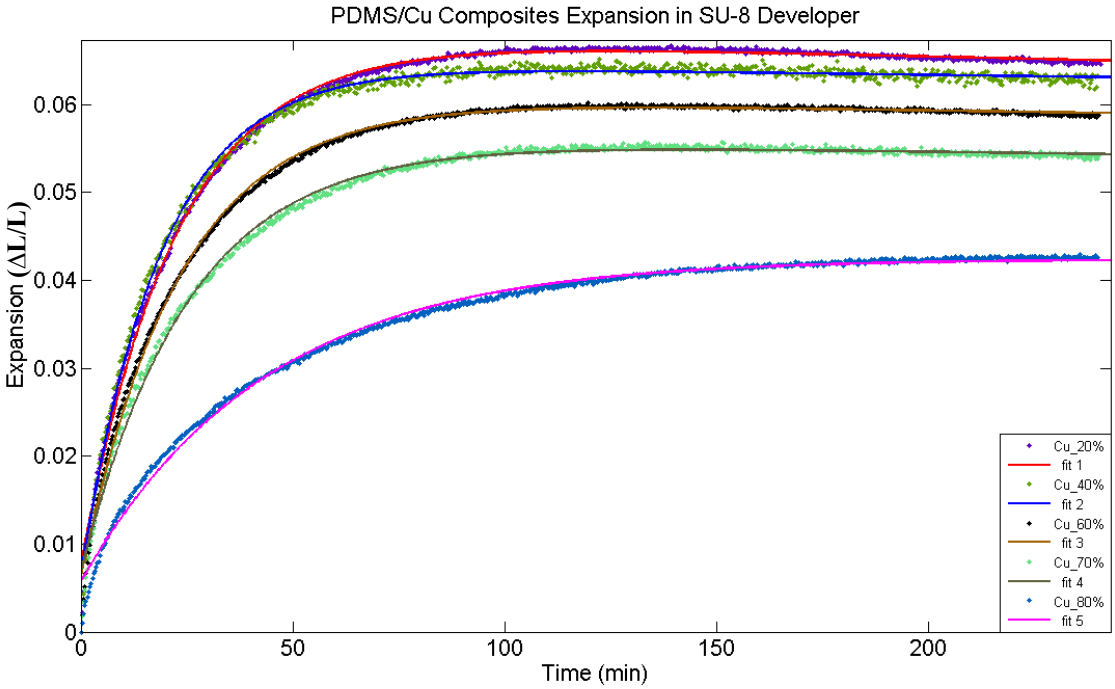

Figure 51 Copper composite expansion kinetics in SU-8 Developer

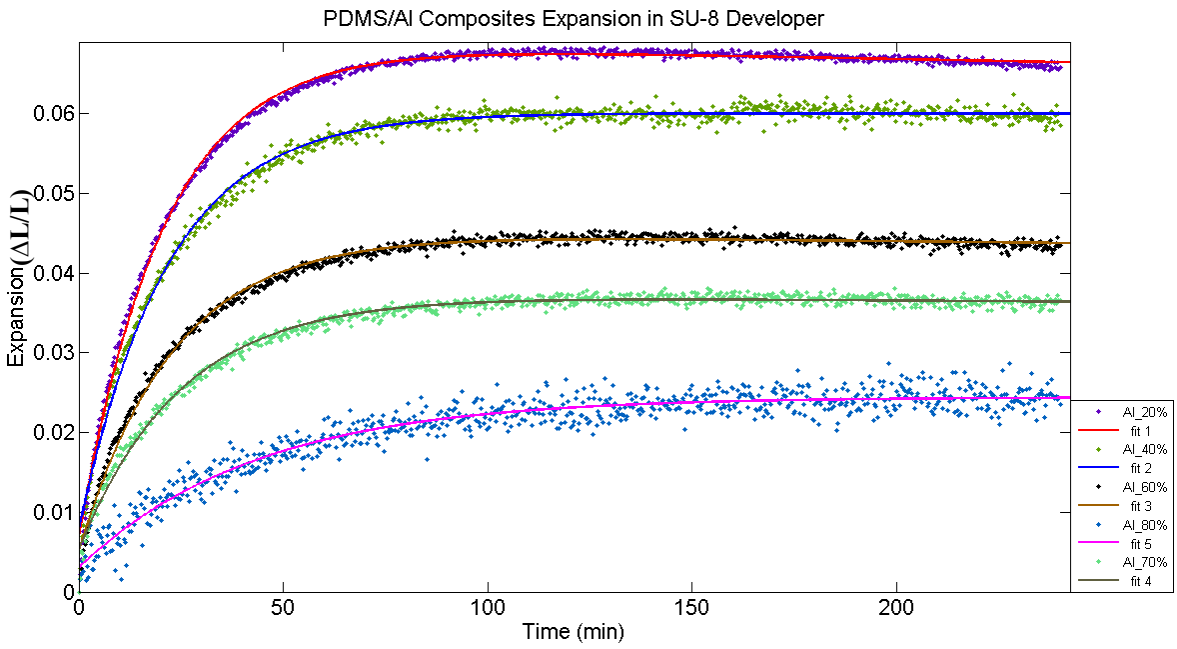

Figure 52 Aluminum composite expansion kinetics in SU-8 Developer

	SU-8 Developer				
	R-square	**a**	**b**	**c**	**d**
Stainless steel					
20%	0.9751	0.08177	12130	-0.0748	17.79
40%	0.9939	0.07176	7430	-0.0624	21.01
60%	0.9928	0.06475	6491	-0.0563	23.34
70%	0.9965	0.05655	8025	-0.0503	24.05
80%	0.9966	0.0422	9173	-0.038	25.77
Ni					
20%	0.9956	0.0828	4555	-0.0716	20.45
40%	0.9963	0.06916	7678	-0.0607	21.87
60%	0.9963	0.06219	10010	-0.0541	23.35
70%	0.995	0.05624	102900	-0.0502	24.16
80%	0.9022	0.03125	30940	-0.0283	9.806
Fe					
20%	0.9899	0.07222	25950	-0.0613	22.13
40%	0.997	0.07019	6217	-0.0625	22.58
60%	0.9958	0.05909	12660	-0.0505	24.13
70%	0.994	0.05577	5308	-0.0497	25.66
80%	0.9819	0.04166	97490	-0.0353	39.07
Cu					
20%	0.9974	0.06771	5981	-0.0602	22.58

40%	0.996	0.06464	10220	-0.0583	22.86
60%	0.9978	0.06079	8346	-0.0546	23.32
70%	0.996	0.05603	8052	-0.0492	25.48
80%	0.9953	0.04257	110300	-0.0367	43.73
Al					
20%	0.9969	0.06586	6803	-0.0621	20.78
40%	0.9924	0.06001	11240	-0.0524	21.55
60%	0.9938	0.0451	8083	-0.04	23.11
70%	0.9906	0.03729	110150	-0.032	25.01
80%	0.929	0.02449	91910	-0.0215	43.47

Table 5 The R-Square and a, b, c, d values for composites in SU-8 Developer

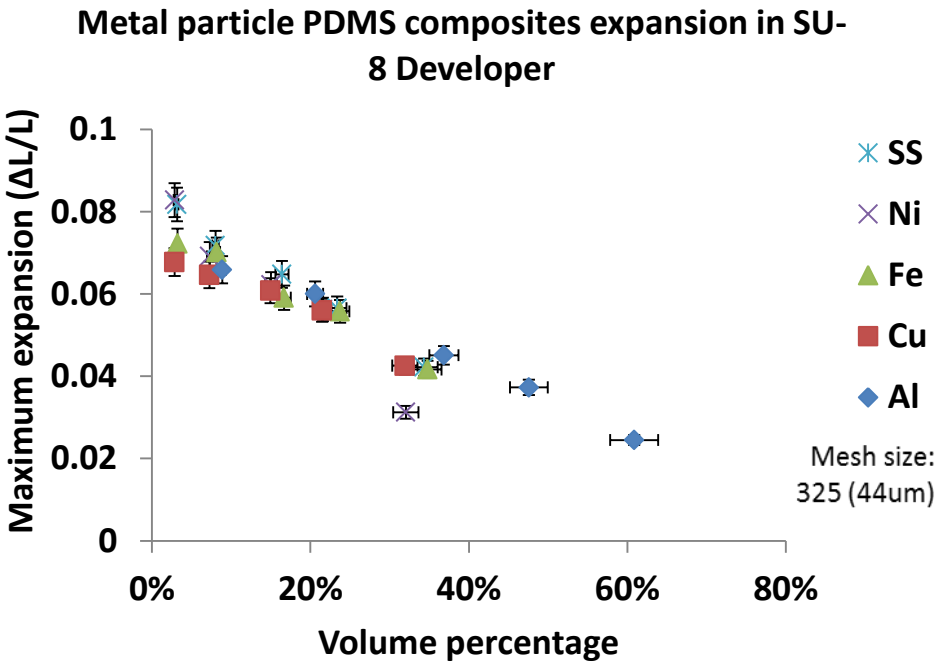

Figure 53 Volume percentages of all five types of composites versus their the maximum expansion in SU-8 Developer

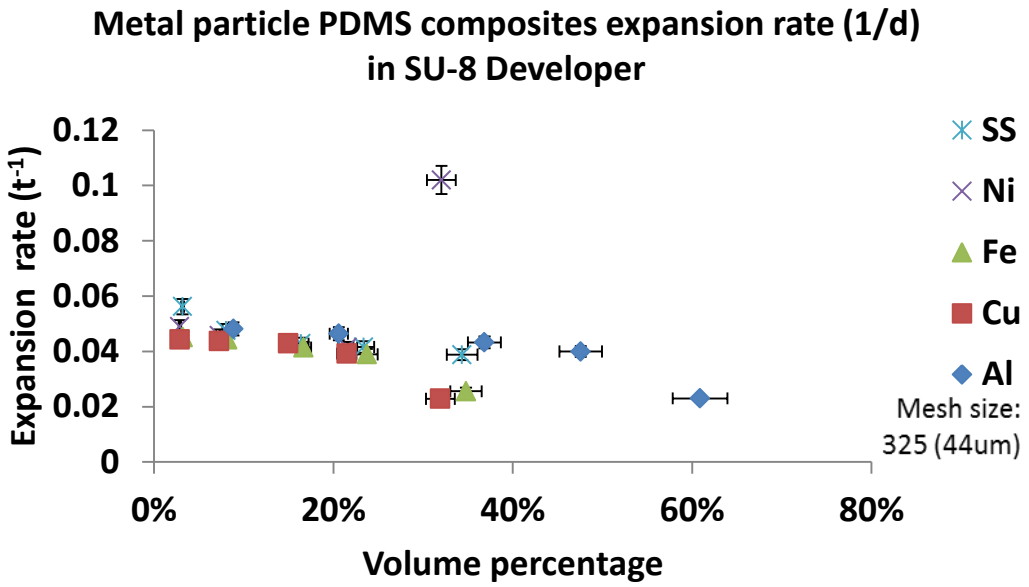

Figure 54 Plot of volume percentages of five metal particle composites versus the inverse of the value d in SU-8 Developer.

4.2.3.3. Metal Particle PDMS Composites Swelling Kinetics in IPA

The solubility parameter of IPA is 24.5MPa$^{1/2}$, a little bit far away to the solubility parameter of PDMS (14.9MPa$^{1/2}$), comparing to the solubility parameters of Toluene (18.2MPa$^{1/2}$) and SU-8 Developer (18.8MPa$^{1/2}$). Therefore, the linear expansion of PDMS composites in IPA is smaller than the linear expansion in Toluene and SU-8 Developer. The maximum expansion of composites at 20% mass ratio for each metal particle is smaller than the expansion in either Toluene or SU-8 Developer. Figure 54--58 shows the swelling kinetics of the five metal particle composites in IPA associated with the curve fitting in order to obtain the character parameter of these data. All of the parameters of R-Square, a, b, c and d are listed in Table 6. From Figure 54--58, it can be observed that compared to the swelling kinetics of these composites in Toluene and SU-8 Developer, composites do not swell to its maximum degree in 4 hours. Indeed, from Table 6, the d values are much larger than the d values for the expansion in Toluene and SU-8 Developer, which indicates that the swelling rate of the composites in IPA is much slower than

the swelling rate in Toluene and SU-8 Developer. However, the curve-fitting function still works well according to the value of R-Square close to 1.

Stainless steel particle composite swells to the maximum, 5.601%, at mass ratio 20%; and swells to the minimum 3.078% at mass ratio 80%, as shown in Figure 54. Similar to the expansion behavior in high mass ratio for Toluene and SU-8 Developer, Stainless steel particle composite's expansion decreases by 0.85% at most as the mass ratio increases from 70% to 80% due to the volume percentage increases most.

Nickel particle composite expands to the maximum, 5.054%, at mass ratio 20%; and expands to the minimum 0.971% at mass ratio 80% as shown in Figure 56. The maximum expansion decrease occurs as the mass ratio increases from 70% to 80%, where the linear expansion increases 1.628% (Figure 55).

Figure 56 shows the swelling kinetics of iron particle composites in IPA. The maximum expansion at 20% mass ratio is 5.58%; the value is larger than the expansion for nickel composite but smaller than the expansion for stainless composite. This behavior is consistent with the expansion in Toluene. In addition, this composite expansion decreases most, 0.966% as mass ratio increases from 70% to 80%, which is consistent with the expansion phenomena for nickel and stainless steel composites.

Copper particle composite swells to the maximum, 5.465%, at mass ratio 20%; and swells to the minimum 2.354% at mass ratio 80%, as shown in Figure 57. Similar to the expansion behavior in high mass ratio for Toluene and SU-8 Developer, This composite's expansion decreases by 0.864% at most as the mass ratio increases from 70% to 80% due to the volume percentage increases most.

As expected, aluminum particle composite swells less than other metal particle composites at the same mass ratio, since it has the largest volume percentage at each mass ratio. The maximum expansion at mass ratio 20% is 4.841%. The minimum expansion at mass ratio 80% is 1.313%. These two values are lower than the expansion of other metal composites at the same mass ratio. The maximum expansion decrease occurs as the mass ratio increases from 40% to 60%, where the linear expansion decreases 0.96%. In figure 58, the data series distribution along the expansion fitting curve is wider than the other plots. The reason is because aluminum particle composite is light-white color. Its contrast to the environment is less obvious comparing to the darker composites such as nickel or stainless steel composites.

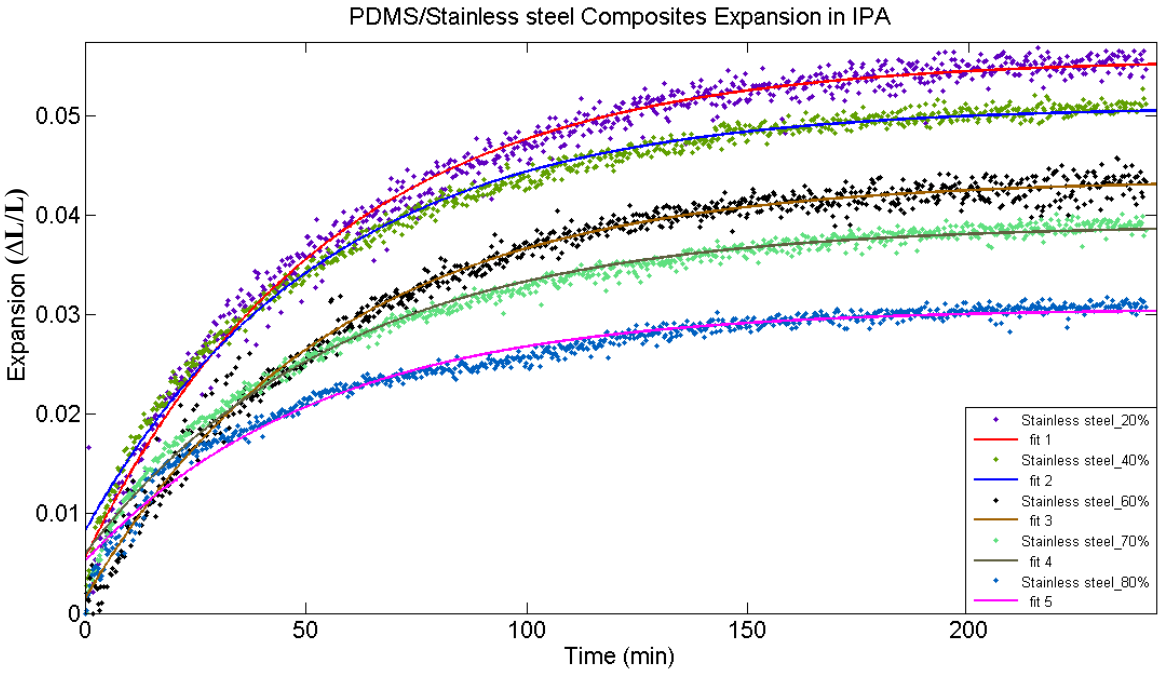

Figure 55 Stainless steel composite expansion kinetics in IPA

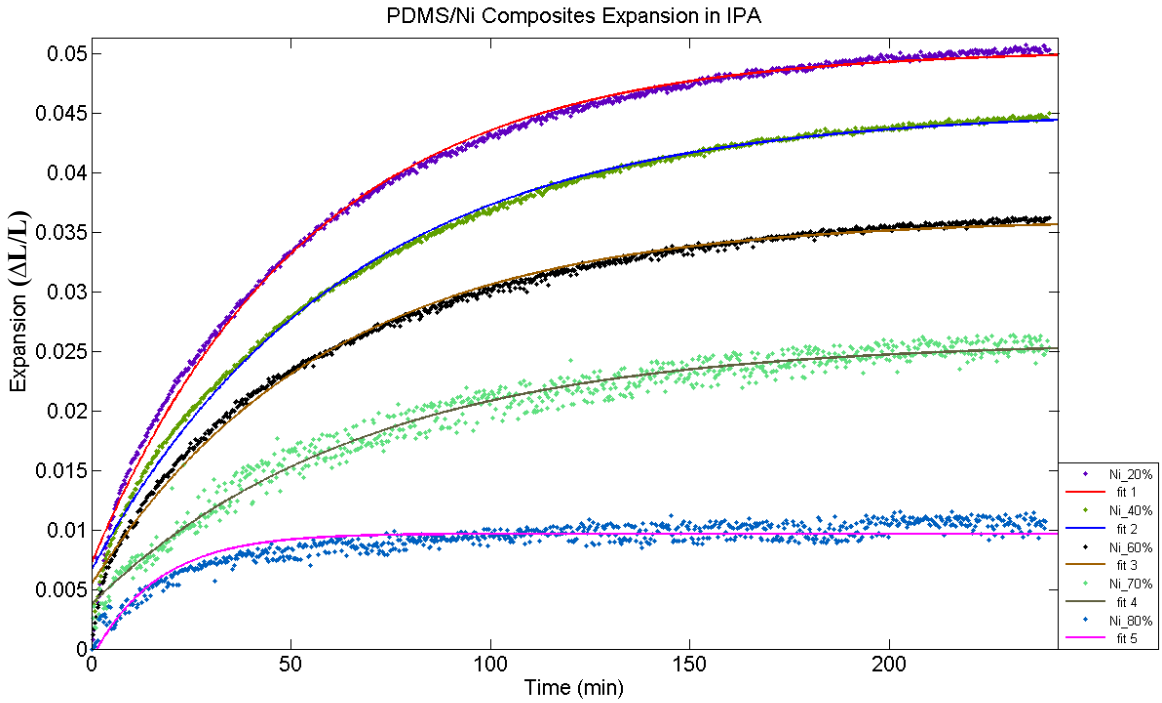

Figure 56 Nickel composite expansion kinetics in IPA

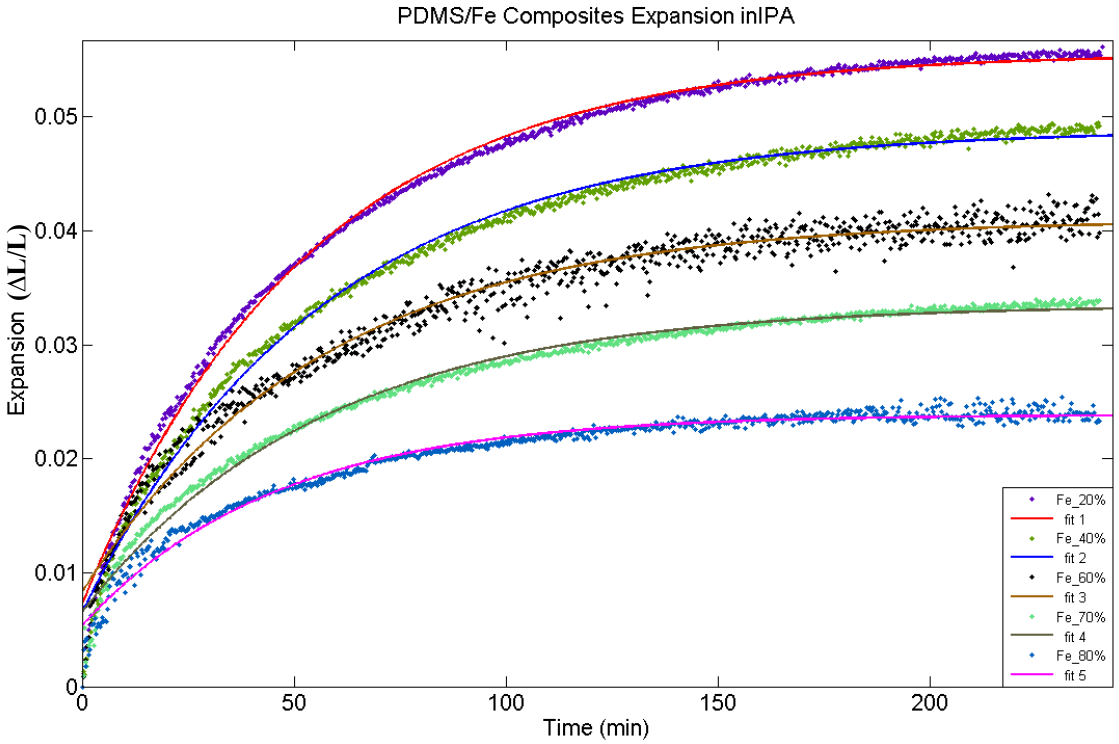

Figure 57 Iron composite expansion kinetics in IPA

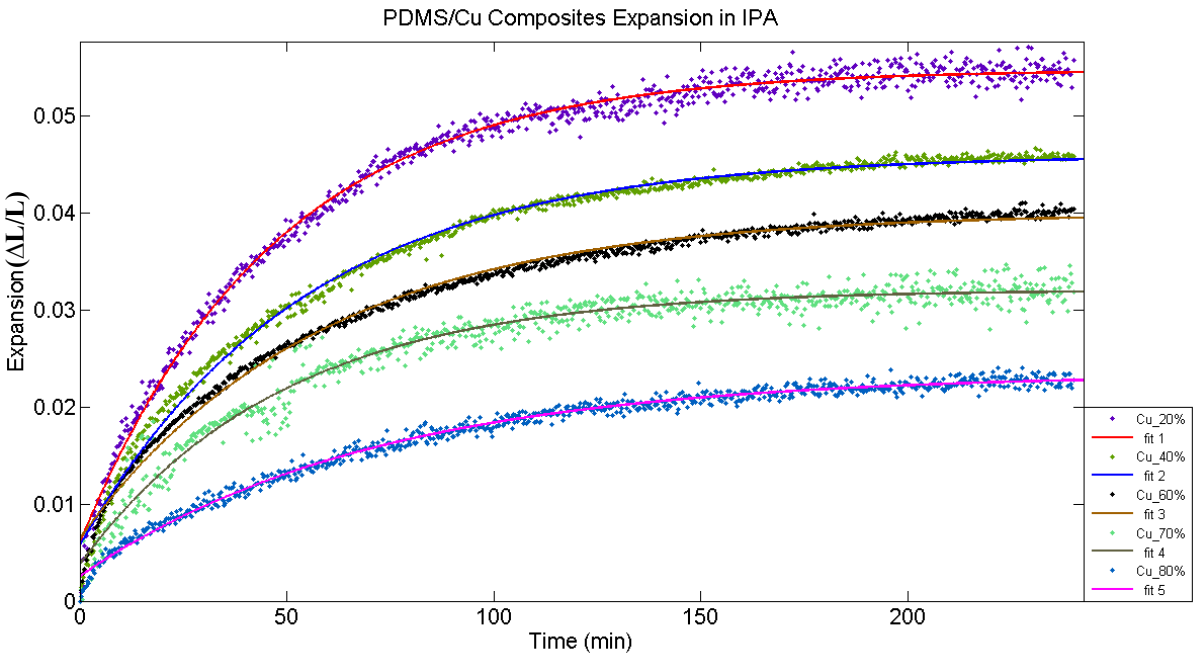

Figure 58 Copper composite expansion kinetics in IPA

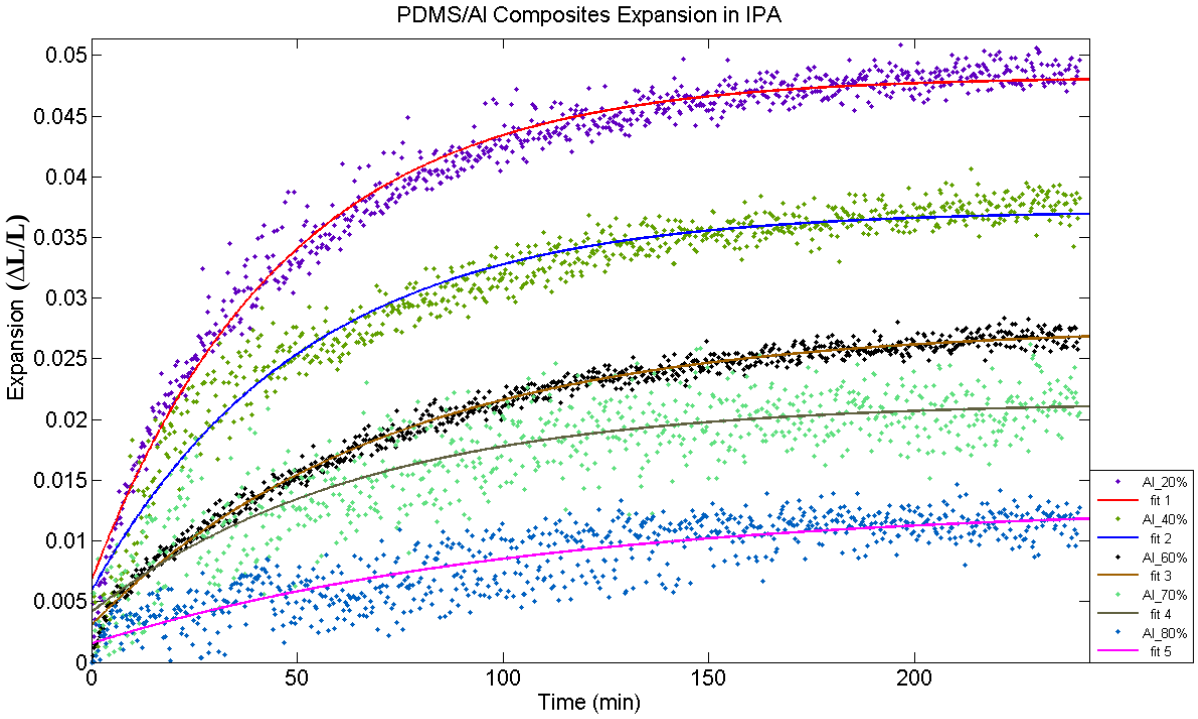

Figure 59 Aluminium composite expansion kinetics in IPA

	IPA				
	R-square	**a**	**b**	**c**	**d**
Stainless steel					
20%	0.9878	0.05601	90010	-0.0046	55.12
40%	0.9924	0.05116	90000	-0.0429	55.31
60%	0.9879	0.0438	90400	-0.0424	55.56
70%	0.9898	0.03928	90150	-0.0333	57.52
80%	0.9781	0.03078	89790	-0.0256	57.91
Ni					
20%	0.9956	0.05054	97150	-0.0433	54.52
40%	0.9967	0.04543	97150	-0.0388	58.75
60%	0.9947	0.03626	97150	-0.0308	67.71
70%	0.9755	0.02599	71550	-0.0222	68.01
80%	0.8318	0.00971	40830	-0.0106	16.5
Fe					
20%	0.9963	0.0558	92030	-0.0485	53.24
40%	0.994	0.04906	97150	-0.0425	56.47
60%	0.9772	0.04111	102300	-0.0328	56.42
70%	0.9895	0.03363	81790	-0.0271	56.4
80%	0.9814	0.02397	61310	-0.0186	45.47
Cu					
20%	0.993	0.05465	96210	-0.0489	47.08
40%	0.9941	0.04604	112800	-0.0404	53.37
60%	0.9931	0.04012	102600	-0.0337	57.31
70%	0.9669	0.03218	70610	-0.0285	58.66
80%	0.9899	0.02354	61650	-0.021	70.59
Al					
20%	0.9803	0.04841	97150	-0.0416	46.73
40%	0.9518	0.03735	81790	-0.0315	51.54
60%	0.9899	0.02775	97150	-0.0247	71.58
70%	0.7474	0.02159	61310	-0.0175	75.17
80%	0.7451	0.01313	41420	-0.0116	107.8

Table 6 The R-Square and a, b, c, d values for composites in IPA

From figure 54--58, it can be seen that after the expansion has not achieved equilibrium after 4 hour in IPA, even though table 6 shows that for the parameter b, their values are in the range 10^4~10^5. The decay does not exhibit in these plots. Figure 59 shows the relation between volume percentage and expansion extents for the five metal particles. The higher volume percentage of metal particles in the composites, the lower the samples swell. Since IPA contains OH group and

thus relative polar solvent. It swells PDMS in smaller degree comparing to Toluene. In addition, its molecule volume is relative small and able to pass through small free space in the composite. Therefore, the expansion rate would not change much even with the increase of volume percentage of metal particles. This can be seen from Figure 60, where for the parameter 1/d, plotted in Figure 60 indicating the swelling rate. The swelling rate for all cases are smaller than 0.22. It has been realized that the value of d increases with the increase of mass ratio for all types of composites. Therefore, the swelling rate decreases with the increase of mass ratio. The exception is for the nickel particle composite in 80% mass ratio, where its b value is 16.5, much lower than other b values of nickel composites. Thus its swelling rate is relatively high (1/d=0.06061). This behavior is consistent with the expansion case in Toluene and SU-8 Developer solvents. Similar to the expansion in Toluene and SU-8 Developer, aluminum particle composites swell slower due to their larger volume percentages within the same mass ratio as other metal particle composites. The swelling rate of these composites in IPA is lower than the swelling rate of the composites in Toluene and SU-8 Developer.

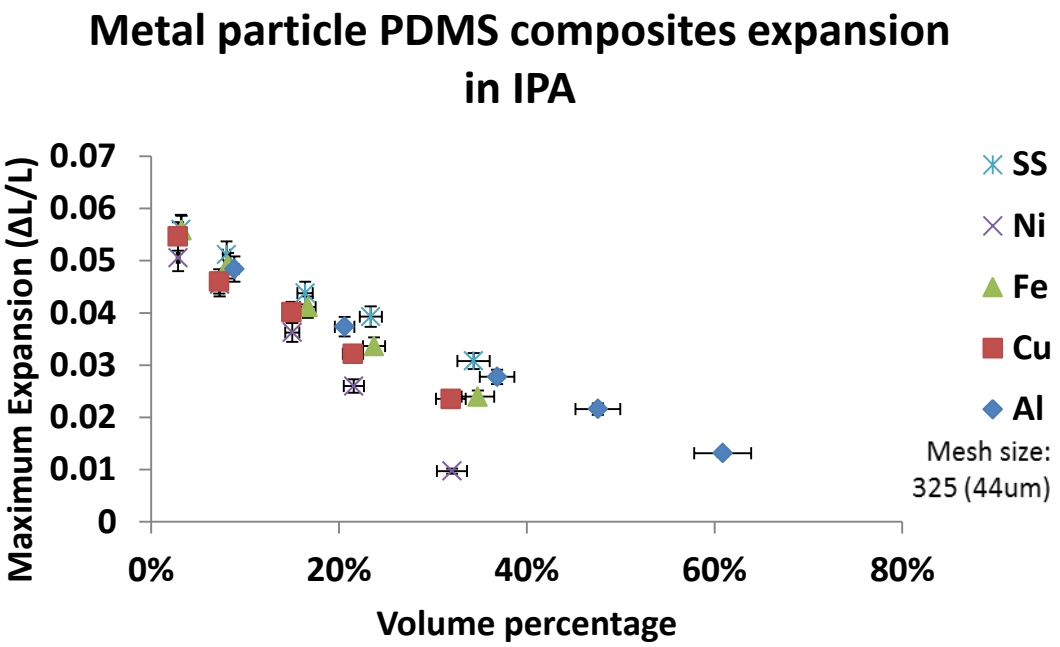

Figure 60 Volume percentages of all five types of composites versus their the maximum expansion in IPA

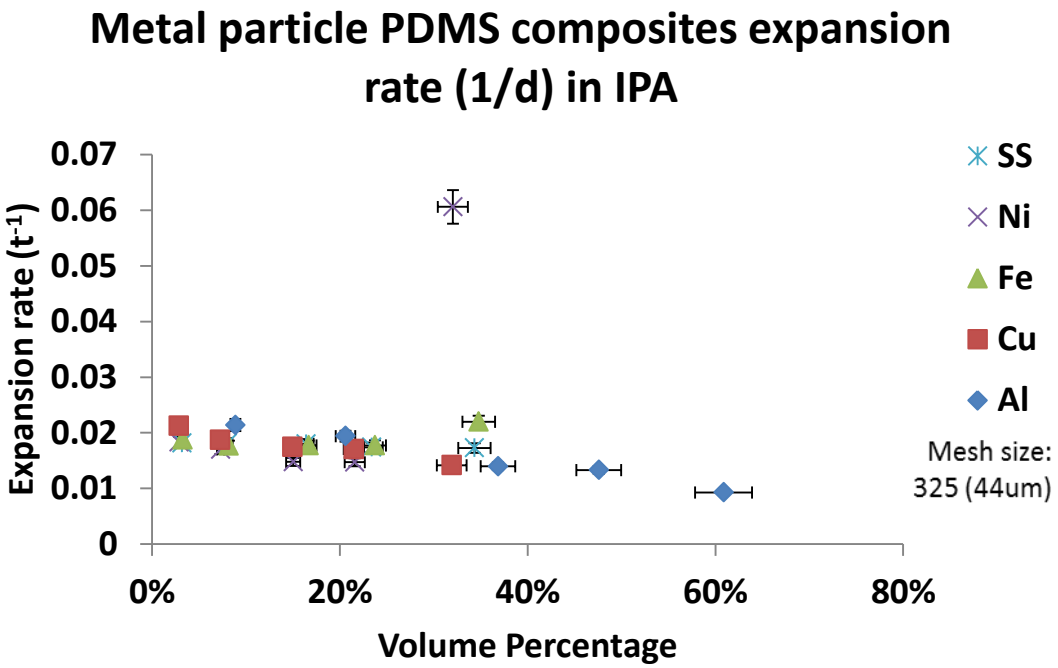

Figure 61 Plot of volume percentages of five metal particle composites versus the inverse of the value d in IPA

4.2.3.4. Metal Particle PDMS Composites Swelling Kinetics in Methanol

The swelling kinetics of PDMS metal particle composites in Methanol solvent is different from these in Toluene, SU-8 Developer and IPA. First, the expansion is much smaller at every mass ratio. This is because the solubility parameter of Methanol is far away from the solubility parameter of PDMS comparing to the solubility parameters of Toluene, SU-8 Developer and IPA. Second, the maximum expansion increase occurred in other solvents are not obvious in Methanol, though the expansion still decreases with the increase of particle mass ratio. Third, due to the light scattering through Methanol, the data distribute along the swelling trend wider than these data series for Toluene, SU-8 Developer and IPA. Fourth, the swelling rate rises up at mass ratio 80% for the case of nickel particle composite in other solvents does not occur in Methanol.

For the swelling kinetics of Stainless steel particle composite in Methanol as shown in Figure 61, the maximum expansion is 1.281% at mass ratio 20% (Table 7), which is much smaller than the expansion in other solvents. That is also true for the minimum expansion, 0.359% at mass ratio 80%. This is caused by the solubility of Methanol to PDMS. Methanol is a more polar solvent that is not a good solvent for non-polar polymers such as PDMS. The total solubility parameter of Methanol is 29.6$MPa^{1/2}$, which is far away from the solubility parameter of PDMS, 14.9$MPa^{1/2}$. Since the expansion in Methanol is so small, the maximum expansion drop with the mass ratio increase is not consistent. This is because the expansion drop is too small to be observed. But the expansion reduces with the increase of stainless steel percentage can be detected.

Figure 62 shows the swelling kinetics of PDMS nickel particle composite. It can be seen that the maximum expansion at mass ratio 20% is 0.944%, smaller than that of stainless steel composite. The minimum expansion is 0.491%, a little bit higher than that of stainless steel composite. Indeed, from Figure 62, it can be found that the five data series are compressed into a

narrow range from 0.491% to 0.944%. That means the expansion change associated with the mass ratio change is not obvious for the nickel composite in Methanol. That is also true for the case of iron composites expansion. In Figure 63, for the mass ratio increase from 40% to 80% (four data series in total), the expansion decreases from 0.932% to 0.556% (minimum expansion). However, the maximum expansion at mass ratio 20% is not "compressed", which has the value of 1.202%, which is smaller than the expansion of stainless steel but larger than the expansion of nickel. This behavior is consistent with the observation of expansion in Toluene.

Copper particle composite swells 0.985% at mass ratio 20% and 0.329% (Table 7) at mass ratio 80% as shown in Figure 64. Similar to stainless steel and nickel composites, there is not obvious expansion drop in the mass ratio increase. The maximum expansion of copper composite is smaller than iron composite expansion but larger than nickel composite expansion. This phenomenon is also observed in the expansion in Toluene.

Aluminum particle composite's expansion (Figure 65) is smaller than other composites in the same mass ratio due to its higher volume ratio. The maximum expansion at mass ratio 20% reaches to 0.87%, smaller than the expansion for other composites but similar to the expansion of iron composite at 40%. The minimum expansion at mass ratio 80% is only 0.262%. It is interesting to note that at 20%, the swelling trends exhibit different motion, where the material swells to its maximum (0.95%) in about 18 minutes and then move down to 0.87% and then keep steady. Similar situation happens to the composite at 40%, where it swells to the maximum (0.7%) in 21 minutes and then goes down to 0.6.4% and then keeps steady. That might be caused by the PDMS relaxation in the swelling process. However, this case never occurs in other mass ratios or for other types of metal composites.

Figure 65 shows that after the expansion reaches the maximum, it will not swell further. This can also be obtained from Table 7, where the b values of aluminum composites are in the order to $3x10^5$, indicating the decay is negligible. However, this is not for all cases. For example, the iron composites at mass ratio 40%, 60% and 80% exhibit decay afterwards. The decay is caused by the extraction of PDMS oligomers into Methanol [118]. The details will be discussed in the case of the expansion behavior in Acetone solvent.

Figure 66 shows the relationship between expansion and volume percentage. The larger volume percentage (larger mass ratio), the less expansion degree is. Figure 67 shows the relationship between swelling rate and the volume percentage. Different with the plot for Toluene, where the swelling rate rises up at mass ratio 80% for the case of nickel particle composite, it does not occur in Methanol. The swelling rate at 80% is smaller than the swelling rate at 70% as it is in the cases of stainless steel, iron and copper composites. It has to be mentioned that the swelling rate for aluminum composites at 20% and 40% are higher than the swelling rate of other composites at the same mass ratio. In addition, the swelling rates for all types of metal composites are faster than the swelling rates in IPA solvent, even though the swelling degree is much smaller in Methanol.

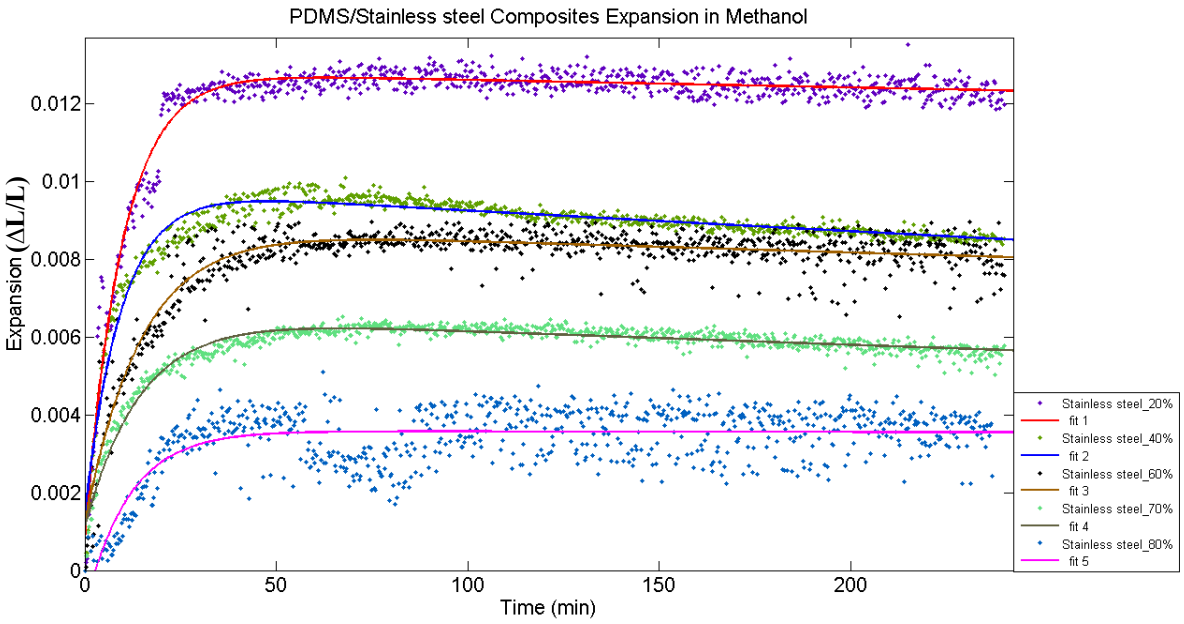

Figure 62 Stainless steel composite expansion kinetics in Methanol

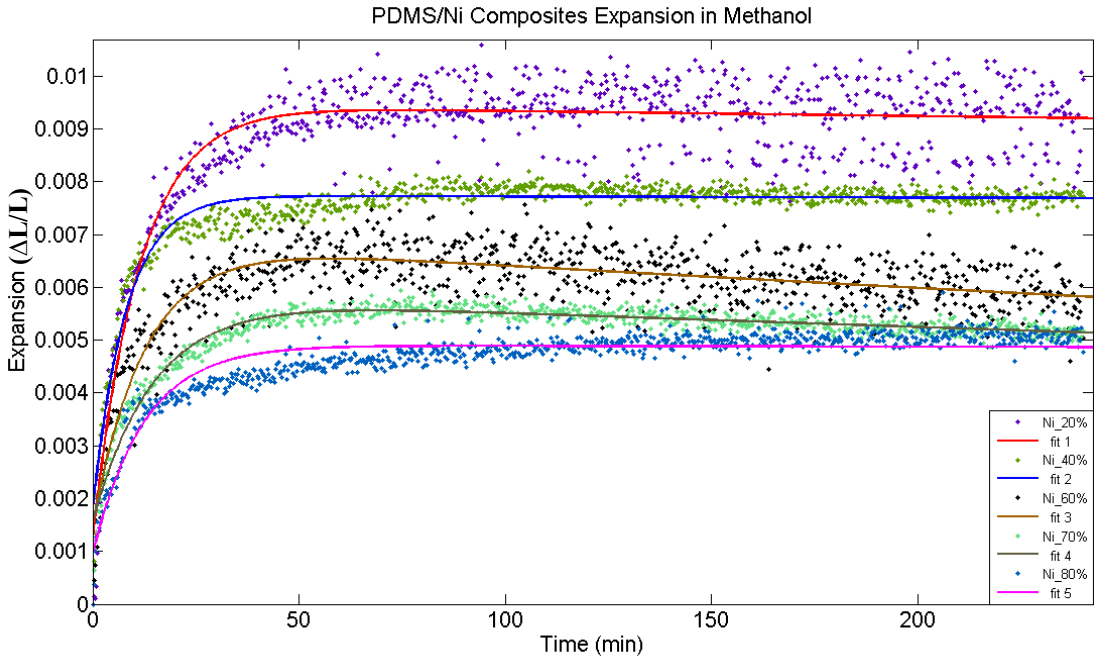

Figure 63 Nickel composite expansion kinetics in Methanol

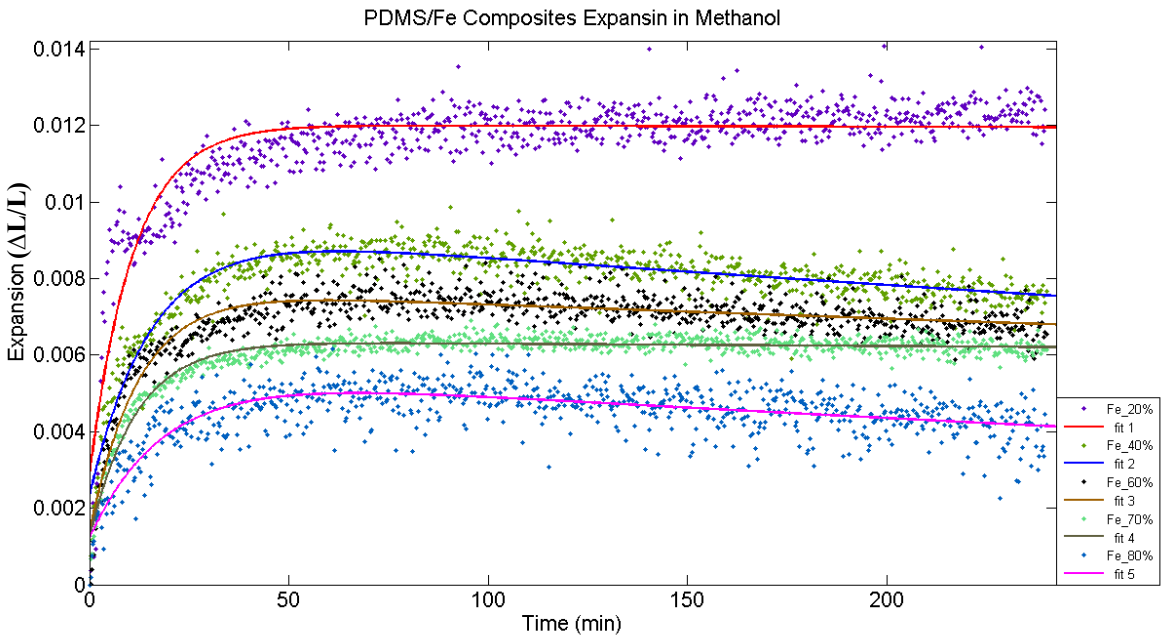

Figure 64 Iron composite expansion kinetics in Methanol

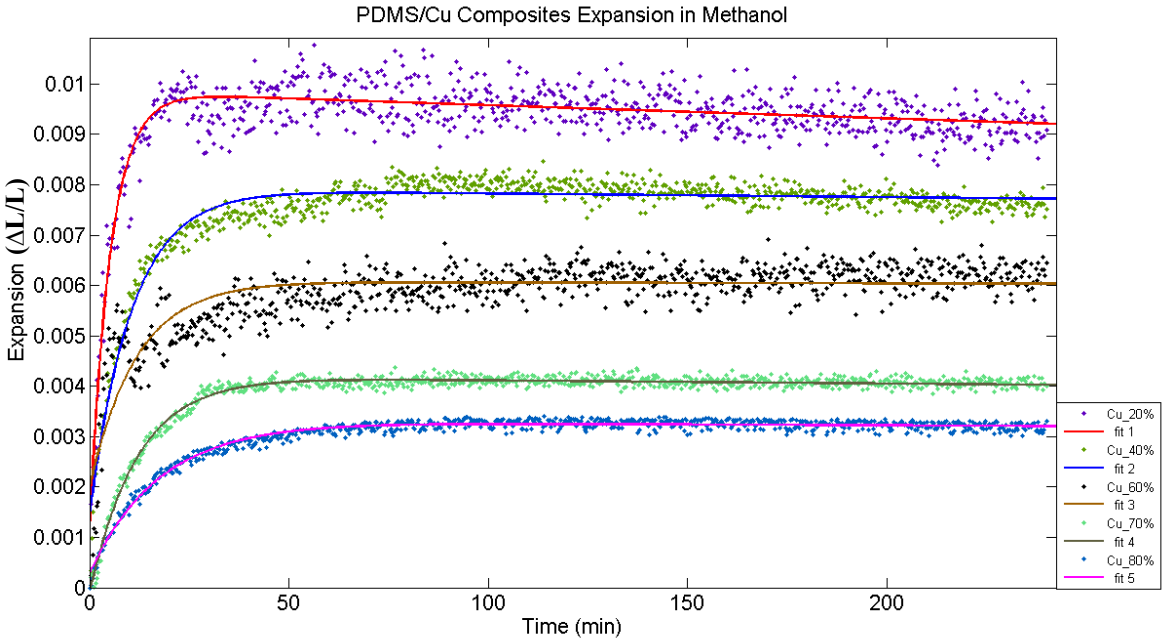

Figure 65 Copper composite expansion kinetics in Methanol

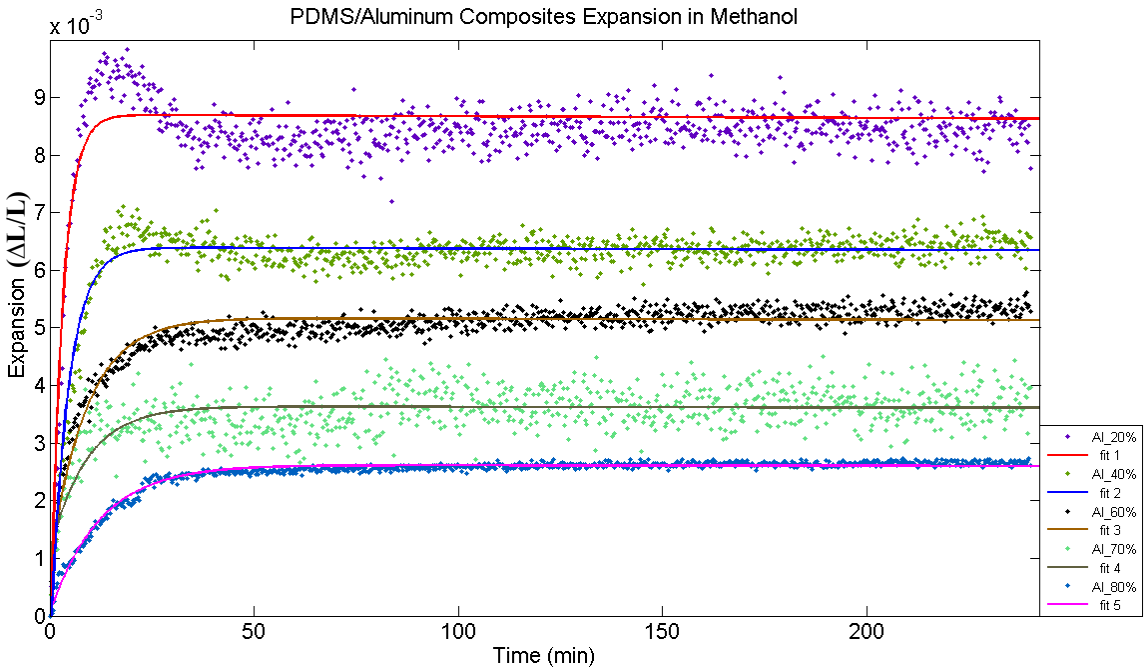

Figure 66 Aluminum composite expansion kinetics in Methanol

	Methanol				
	R-square	**a**	**b**	**c**	**d**
Stainless steel					
20%	0.9567	0.01281	6435	-0.0121	9.61
40%	0.9469	0.00982	1690	-0.0084	9.644
60%	0.8769	0.00877	2817	-0.0076	14.35
70%	0.9476	0.00652	1705	-0.0054	14.66
80%	0.4936	0.00359	26750	-0.0046	14.75
Ni					
20%	0.8269	0.00944	9545	-0.0082	11.34
40%	0.9186	0.00774	36650	-0.006	11.26
60%	0.7212	0.00686	1464	-0.0054	12.72
70%	0.9399	0.00579	2018	-0.0042	14.8
80%	0.8418	0.00491	31190	-0.004	14.82
Fe					
20%	0.8078	0.01202	46590	-0.0092	10.91
40%	0.8446	0.00932	1150	-0.007	11.06
60%	0.8395	0.00771	1927	-0.0064	12.21
70%	0.9378	0.00636	10110	-0.0051	15.66
80%	0.8028	0.00556	817.7	-0.0043	18.53
Cu					

20%	0.8438	0.00985	3606	-0.0088	5.144
40%	0.939	0.0079	10590	-0.0065	10.56
60%	0.6805	0.00608	30590	-0.0041	11.79
70%	0.9791	0.00418	6396	-0.0043	11.97
80%	0.9749	0.00329	8978	-0.003	17.68
Al					
20%	0.8885	0.0087	30000	-0.0099	2.91
40%	0.9008	0.0064	30040	-0.0072	4.294
60%	0.8978	0.00518	29310	-0.0043	9.01
70%	0.48	0.00364	30010	-0.0025	9.25
80%	0.9751	0.00262	30020	-0.0026	12.33

Table 7 The R-Square and a, b, c, d values for composites in Methanol

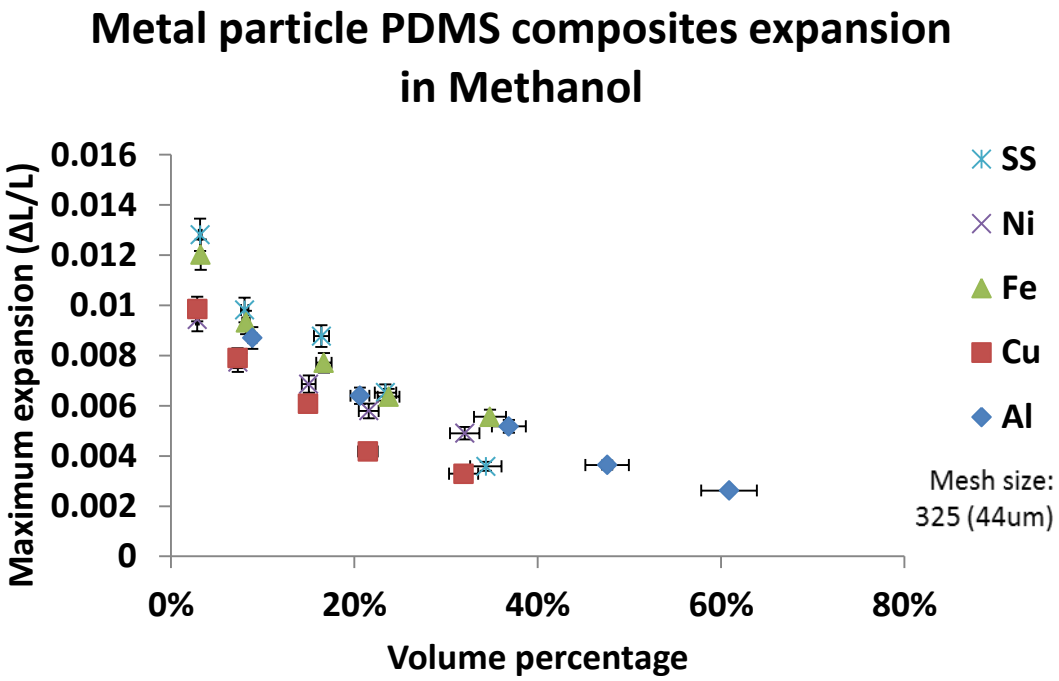

Figure 67 Volume percentages of all five types of composites versus their the maximum expansion in Methanol

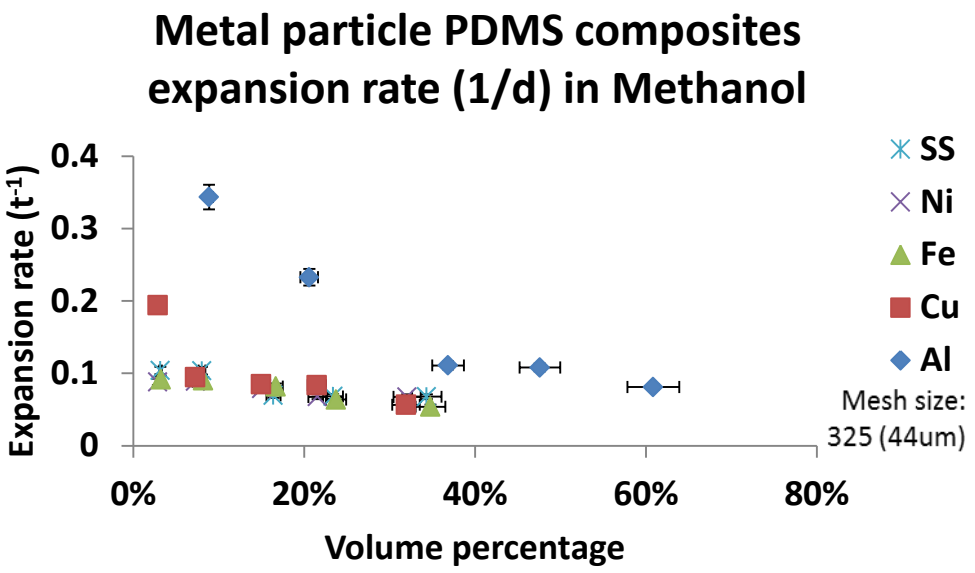

Figure 68 Plot of volume percentages of five metal particle composites versus the inverse of the value d in Methanol

4.2.3.5. Metal Particle PDMS Composites Swelling Kinetics in Acetone

The swelling kinetics of metal composites in Acetone behaves differently with the kinetics in other four solvents, as shown in Figure 68—72. The composites swell to a maximum in relative short time (<50min) and then gradually shrink down to smaller size in the rest time of the 4 hours. The data series that describe expansions for different mass ratio shrink in different rate; these different shrinking rates have no relation with the mass ratio. However, the expansion drops with the increase of particle volume percentage exhibit in all five plots.

For stainless steel composites, the maximum expansion at mass ratio 20% is 8.359% which is extracted from the curve fitting, as shown in Figure 68 and Table 8. This is also the maximum expansion among all five types of particle composites, which is also observed for the expansion in toluene. The minimum expansion is 3.3342% at mass ratio 80%. The maximum expansion drop is found from the mass ratio increase from 70% to 80%, where its value is 1.843%.

Nickel particle composite swells to 7.051% at mass ratio 20% and 2.721% at mass ratio 80%, as shown in Figure 69. The maximum expansion drop is found from the mass ratio increase from 70% to 80%, where its value is 2.058%.

For iron composites, Figure 70, it expands 7.288% at mass ratio 20%, which is smaller than the expansion for stainless steel composite but larger than the expansion for nickel composite. This behavior is consistent with the expansion in toluene. The minimum expansion at 80% is 4.196% and the maximum expansion decrease is 1.517%.

Copper composite swells to its maximum at mass ratio 20% with the value 7.1% and its minimum at mass ratio 80% with the value 4.38%, as shown in Figure 71. The maximum expansion drop is found from the mass ratio increase from 70% to 80%, where its value is 1.816%.

Aluminum particle composite's expansion (Figure 72) is smaller than other composites in the same mass ratio due to its higher volume ratio. The maximum expansion at mass ratio 20% reaches to 6.795%, smaller than the expansion for other composites. The minimum expansion at mass ratio 80% is only 2.695%. The maximum expansion drop is found from the mass ratio increase from 40% to 60%, where its value is 1.524%.

Figure 73 shows the relationship between expansion and volume percentage. The larger volume percentage (larger mass ratio), the less expansion degree is. Figure 74 shows the relationship between swelling rate and the volume percentage. Similar to that happens to Toluene solvent, the swelling rates decrease (1/d decreases) with the increase of particle amount since these particles obstacle the diffusion of solvent molecules. The only exception is for the nickel composite sample at 80%, whose swelling rate is much faster than other composites. The reason for this has been explained in the discussion of the expansion in Toluene.

From table 8, it can be seen that the b values are relatively small (~10^3) and vary with mass ratio. That indicates that there exists diameter decay after reaching the peak expansion. The decay may be caused by the extraction of PDMS oligomers into Acetone solvent. When PDMS molecules are cross-linked to form the polymer, not all the PDMS chains are incorporated into the network. Some PDMS are uncross-linked and in the form of monomer, dimer, trimer or oligomer. These low molecular weight PDMS chains are included in the composites. When the composites are contact with Acetone, these oligomers may be extracted from the bulk. The behavior has been investigated by Malczewski and Inman [119] who studied the extraction residues from silicone tubings by different solvent. They found that Acetone has the best extraction capacity to PDMS oligomers. Another interesting behavior can be observed from Figure 69—73 that with the mass ratio increase, the decay becomes slower. The reason is because the embedded particles may obstacle the diffusion of PDMS oligomers out of the bulk. Metal particles block the diffusion of solvent molecules into the composite, which has been proofed by the swelling rate decrease with the increase of mass ratio. Moreover, the particles might also obstacle the PDMS diffusing out of the composite as the mass ratio increase. From Figure 69—73 it can be observed that at mass ratio 80%, the decay is much smaller than that at lower mass ratio. The only exception is for the case of nickel particle composite at mass ratio 80%, where the decay even faster than that at lower mass ratio. As mentioned before, there exist a lot free spaces in this composite. These free spaces ease the incoming and outgoing diffusion processes. Therefore, PDMS oligomers in this composite diffuse out easily.

Figure 74 presents the expansion rate (1/d) versus the volume percentage for all composites. With the increase of the volume percentage of metal particles, the expansion rate declines. The

exceptional case is for the nickel particle composite at mass ratio 80%, where the expansion rate is much higher due to the effect of free space.

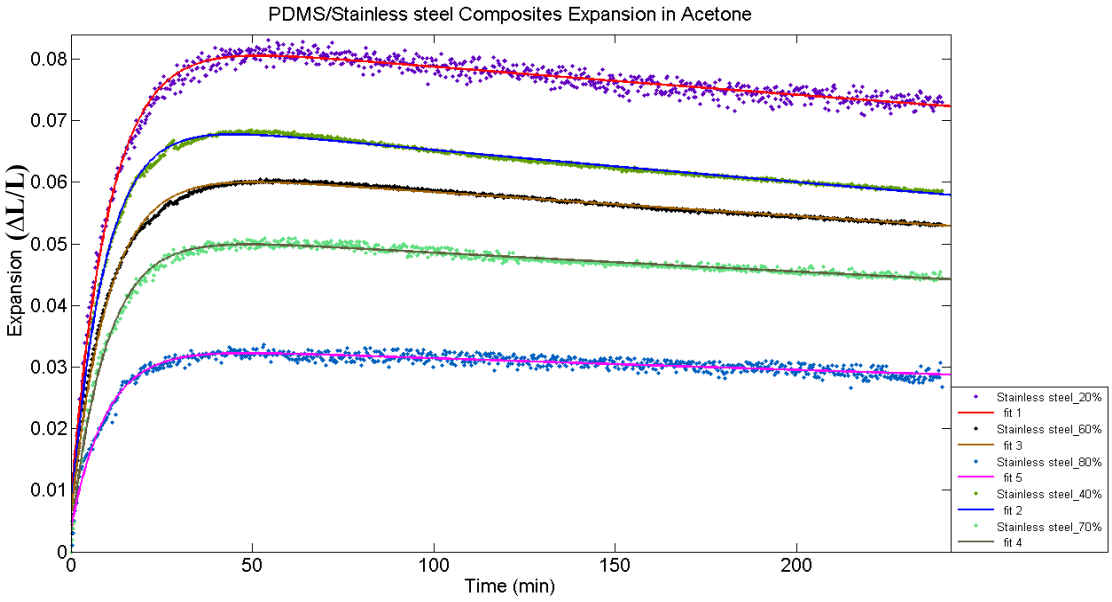

Figure 69 Stainless steel composite expansion kinetics in Acetone

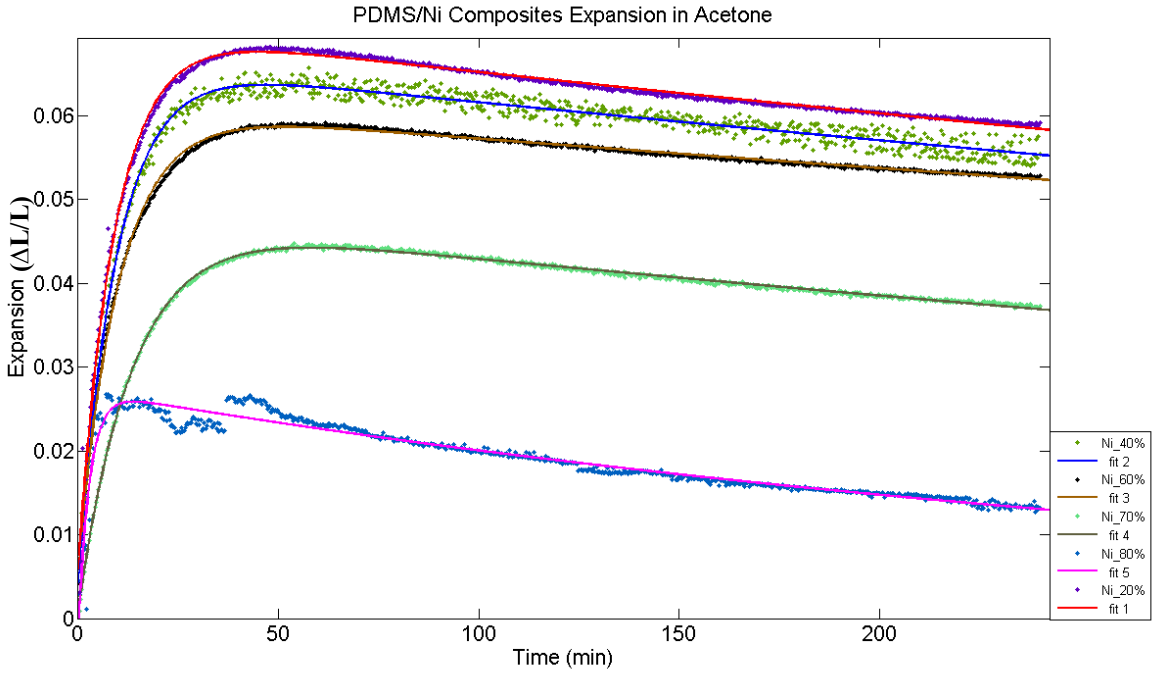

Figure 70 Nickel composite expansion kinetics in Acetone

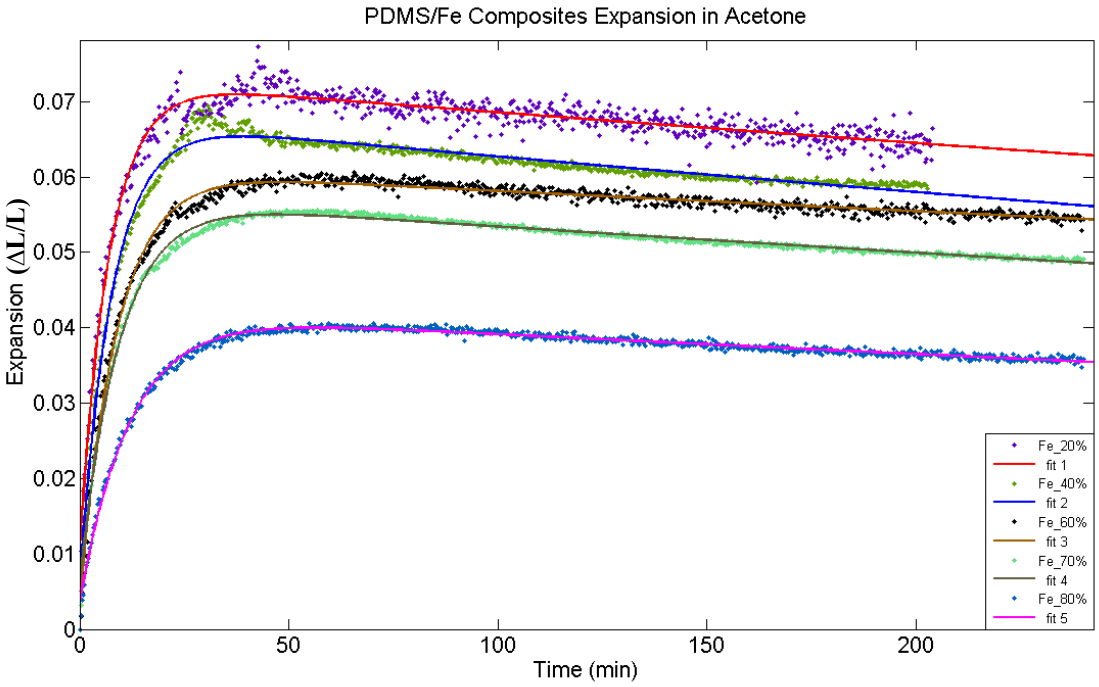

Figure 71 Iron composite expansion kinetics in Acetone

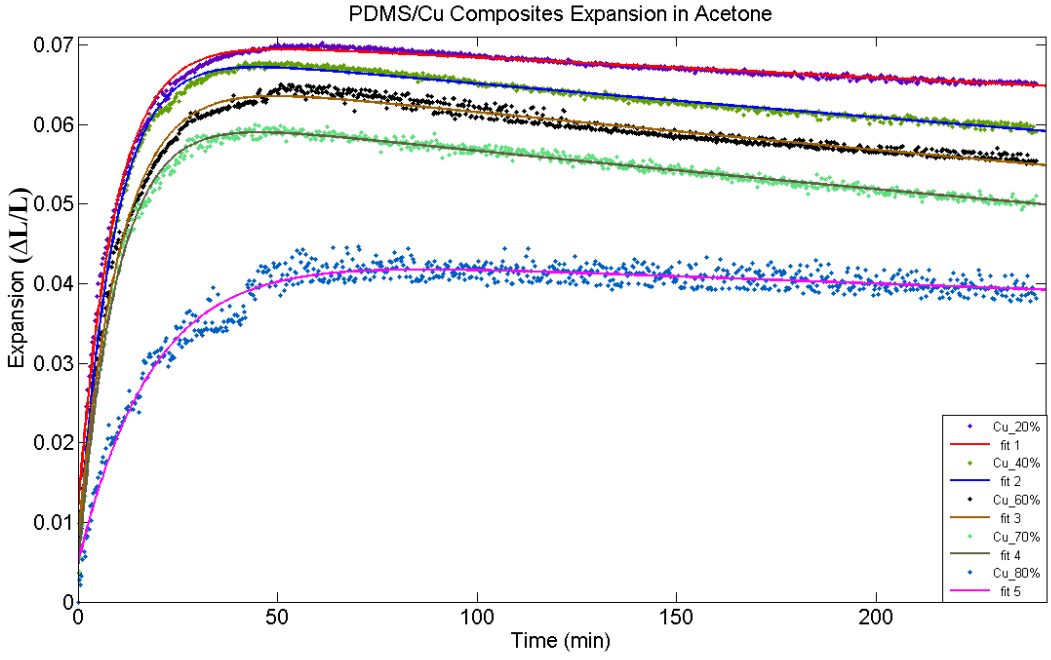

Figure 72 Copper composite expansion kinetics in Acetone

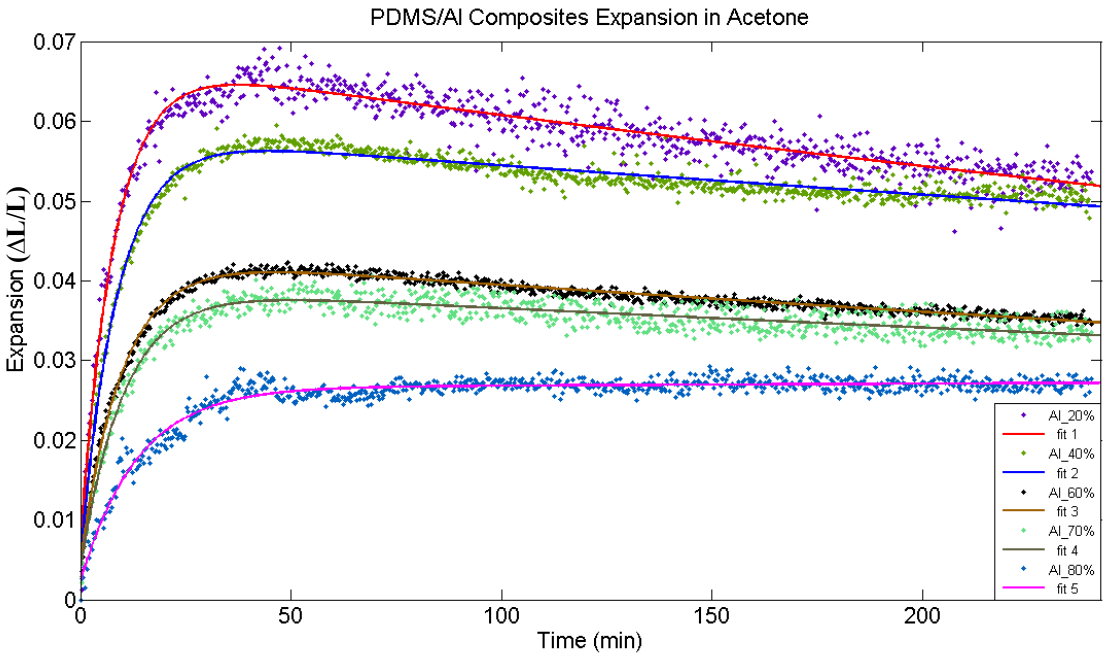

Figure 73 Aluminum composite expansion kinetics in Acetone

	Acetone				
	R-square	**a**	**b**	**c**	**d**
Stainless steel					
20%	0.9851	0.08359	1675	-0.07576	9.326
40%	0.996	0.07089	1200	-0.06467	9.666
60%	0.9995	0.06256	1448	-0.05683	9.74
70%	0.9918	0.05185	1524	-0.04917	10.29
80%	0.9594	0.03342	1610	-0.02975	10.35
Ni					
20%	0.9944	0.07051	1272	-0.06465	9.163
40%	0.9851	0.06647	1307	-0.06217	9.601
60%	0.9961	0.06097	1581	-0.05468	10.36
70%	0.999	0.04779	926.2	-0.04697	13.61
80%	0.9495	0.02721	326.4	-0.02966	2.833
Fe					
20%	0.9624	0.07288	1636	-0.06266	7.022
40%	0.9852	0.06093	2121	-0.05737	8.917
60%	0.9885	0.06309	2121	-0.0594	8.918
70%	0.9931	0.05713	1487	-0.05132	9.982
80%	0.9934	0.04196	1436	-0.03854	11.96
Cu					
20%	0.9917	0.071	2674	-0.05994	9.154

40%	0.9949	0.06966	1482	-0.06436	9.564
60%	0.9867	0.06669	1242	-0.05933	9.84
70%	0.9941	0.06196	1123	-0.05815	10.58
80%	0.9621	0.0438	2198	-0.03902	18.45
Al					
20%	0.9362	0.06795	900	-0.06133	8.022
40%	0.9725	0.05843	1433	-0.05358	8.815
60%	0.9869	0.04319	1119	-0.03865	9.918
70%	0.9304	0.03916	1460	-0.0355	10.28
80%	0.9429	0.02695	73170	-0.0255	12.87

Table 8 The R-Square and a, b, c, d values for composites in Acetone

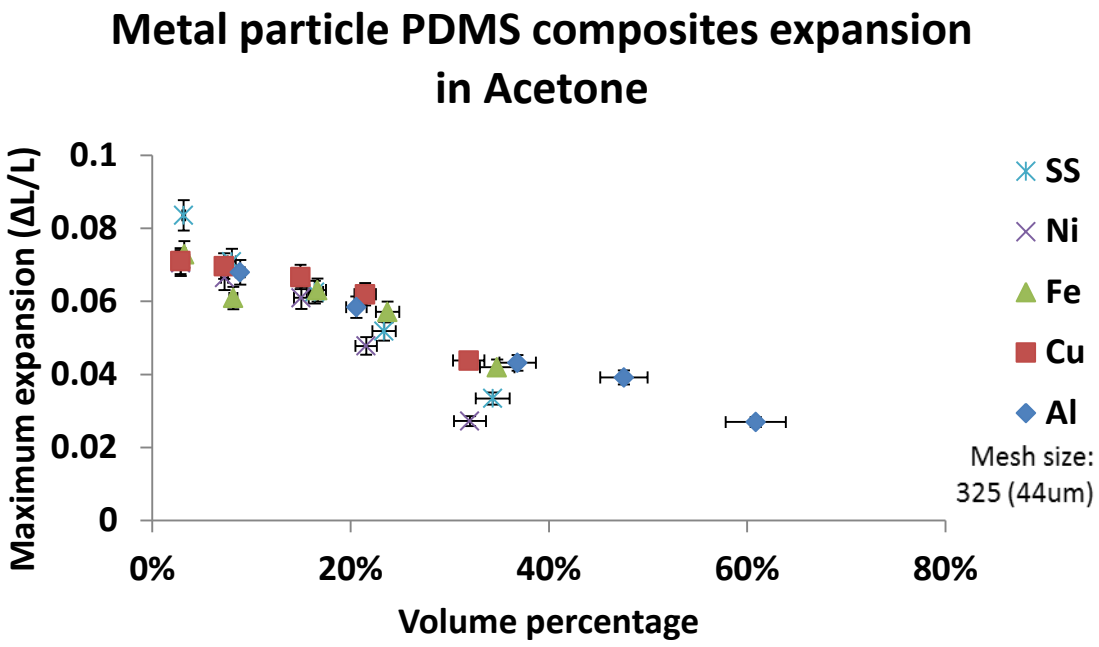

Figure 74 Volume percentages of all five types of composites versus their the maximum expansion in Acetone

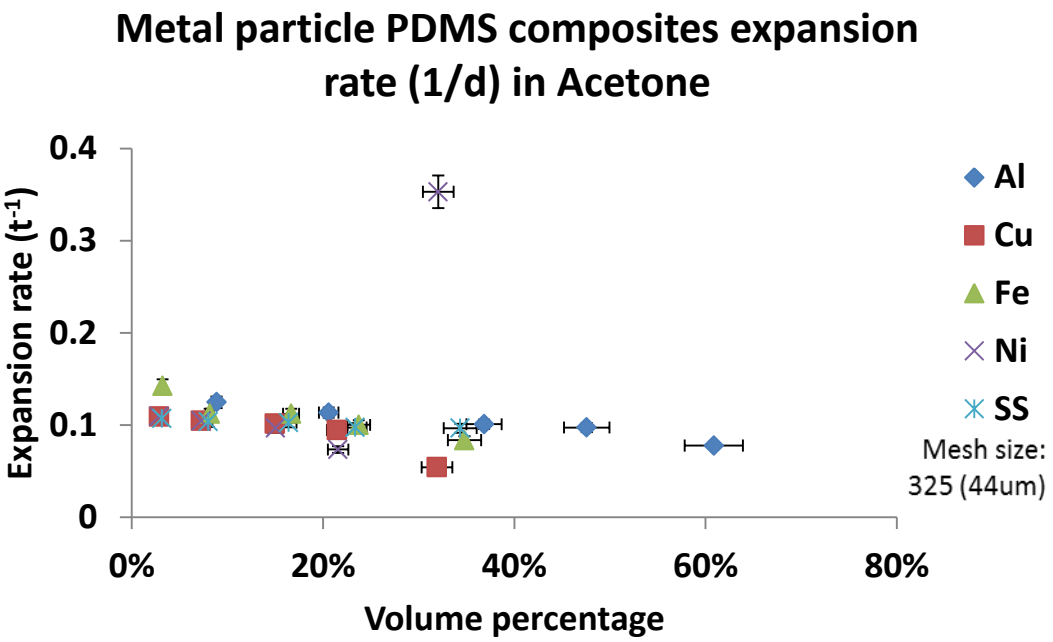

Figure 75 Plot of volume percentages of five metal particle composites versus the inverse of the value d in Acetone

The swelling kinetics of the metal composites in Acetone is very interesting; its swelling behaviors perform differently with the swelling of the composites in other solvents. Not only the swelling behavior of composites; even the swelling of pure cross-linked PDMS still deserves to be study. For example, why is our measurement of the linear expansion of puree PDMS a little bit higher than the measurement from Whitesdes? To better understand the swelling behavior in Acetone, an extra experiment has been completed to test the linear expansion of pure PDMS, which extends the swelling time to 24 hours instead of 4 hours. The sample and procedure are employed are the same as described before in the pure PDMS measurement for 4 hours, As shown in Figure 75, pure PDMS swells to the maximum 9% in 36 minutes, and then gradually shrinks in the rest time. At the end of 24 hour, the linear expansion reaches 6.5%, close to Whitesides' measurement 6% after 24 hours. In addition, from figure 76, it can be observed that in the first 4 hours, the bulk shrinks faster once it achieves maximum expansion. That is due to at

the initial swelling process, the amount of PDMS oligomers and the amount of low molecular weight PDMS oligomers incorporated in the bulk are high. They diffuse out first in the initial swelling and thus the sample diameter reduces faster. After 4 fours, these oligomers have moved out into Acetone solvent, the shrinkage slows down. After 24 hours, the expansion reaches to the value 6.5%.

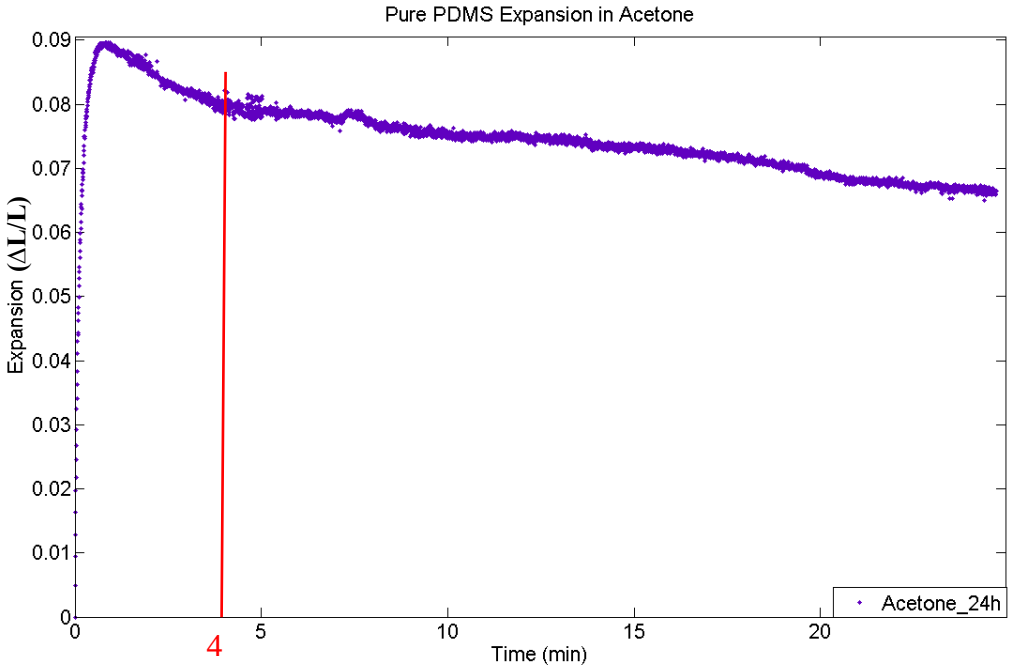

Figure 76 Pure PDMS expansion kinetics in Acetone for 24 hours

4.2.4 Diffusion Coefficients of the Metal Particle Composites in Solvents

From above experiments and analysis, we can see that the expansion degree and swelling rate vary with different composites, different mass ratio and with different solvents. The swelling rate is tightly related to the diffusion process that the solvent species penetrate into the composites. Indeed, the relation between swelling kinetics and diffusion have been developed by Tanaka [120], who studied the swelling kinetics of cross-linked gel by considering both bulk energy and shear energy in the gel. The bulk energy of the system is related to the volume change of the

system, which is controlled by diffusion. The shear energy is related to keeping the shape of the system and to minimize the total shear energy. Tanaka's theory is based on the assumption that the cross-linked gel swelling process is not a pure diffusion process and the friction between network and the solvent is not considered. The shear modulus plays an important role in keeping the geometry of the system. Therefore, the equation for swelling of a gel disk is expressed as [121]:

$$\frac{u(a,t)}{u(r,t)} = \sum_n B_n \exp(-t/\tau_n) \quad (39)$$

where t denotes the swelling time, u(r,t) represents the displacement vector of a point in the network from its final expansion where the gel is completely swollen (u=0, t=∞). The displacement term is expressed as components, each decomposition decaying exponentially with time constant τ_n. B_n is only a function of the ratio of the shear modulus to het longitudinal modulus of the network. This exponential series is convergent exponentially. So the first term is dominant. r is the radius of gel disk in its maximum expansion. Equation 39 can be rewritten as a function that only includes the first term of the exponential series as shown in equation 40:

$$\frac{u(a,t)}{u(r,t)} = B_1 \exp(-\frac{t}{\tau_1}) \quad (40)$$

where $\tau_1 = r^2/D_0$, $\tau_1$is proportional to the square of the gel radius for the spherical gel with zero shear modulus, D_0 is the diffusion coefficient. Since shear energy should be considered in the swelling process, later Li and Tanaka modified τ_1 by inducing the shear modulus r_1^2 :

$$\tau_1 = r^2/3(D_0 r_1^2) \quad (41)$$

and calculated r_1, equal to 2.29 for the gel disk by the elasticity theory [121]. The constant 3 in this equation is to indicate that the diffusion coefficient of gel disk is only one third of the diffusion coefficient of the gel sphere with the same radius. Tanaka had successfully described the swelling kinetics of Acrylamide gel disk in water by using this model. Zrinyi and Horkay

applied Tanaka's theory to describe the swelling behavior of cross-linked Poly(vibyl acetate) (PVAc) in i-PrOH solvent and the theory fitted very well with the experiment results [122].

In our exponential function, the parameter a is the maximum expansion rate. The diameter of the composite disk is L=6.35mm. Therefore, L(1+a)/2 is equivalent to r in equation 45; and the parameter d is essentially the time constant, equivalent to the product of D_0 and r_1. Therefore, equation 45 can be rewritten to derive the diffusion coefficient D_0 if τ_1(d) is known (d can be obtained from the curve fitting). Equation 41 is the rewritten function using parameters a and d to derive D_0:

$$D_0 = \frac{[L(1+a)]^2}{12dr_1^2} \tag{42}$$

hereby, we use r_1=2.29 from the reference [121], since the PDMS network volume percentage is dominant for most composites and the friction between the fluid and network has not been considered in developing the theory. Table 9 lists the diffusion coefficients for all metal composites with different mass ratio in different solvents.

	Diffusion Co. (cm^2/s)				
	Toluene	**SU-8 Developer**	**Methanol**	**IPA**	**Acetone**
Pure PDMS	6.28E-05	1.91E-05	2.96E-05	6.26E-06	4.99E-05
Stainless steel					
20%	5.25E-05	1.61E-05	2.61E-05	4.95E-06	3.08E-05
40%	4.17E-05	1.34E-05	2.59E-05	4.89E-06	2.90E-05
60%	3.37E-05	1.19E-05	1.73E-05	4.80E-06	2.83E-05
70%	2.97E-05	1.14E-05	1.69E-05	4.59E-06	2.63E-05
80%	2.48E-05	1.03E-05	1.67E-05	4.49E-06	2.52E-05
Ni					
20%	4.23E-05	1.40E-05	2.20E-05	4.95E-06	3.06E-05
40%	3.88E-05	1.28E-05	2.21E-05	4.55E-06	2.90E-05
60%	3.10E-05	1.18E-05	1.95E-05	3.88E-06	2.66E-05
70%	2.85E-05	1.13E-05	1.67E-05	3.79E-06	1.97E-05
80%	4.18E-05	2.65E-05	1.67E-05	1.51E-05	9.11E-05
Fe					

20%	4.36E-05	1.27E-05	2.30E-05	5.12E-06	4.01E-05
40%	3.98E-05	1.24E-05	2.25E-05	4.77E-06	3.09E-05
60%	3.72E-05	1.14E-05	2.03E-05	4.70E-06	3.10E-05
70%	3.31E-05	1.06E-05	1.58E-05	4.63E-06	2.74E-05
80%	1.47E-05	6.79E-06	1.33E-05	5.64E-06	2.22E-05
Cu					
20%	3.95E-05	1.23E-05	4.85E-05	5.78E-06	3.06E-05
40%	3.30E-05	1.21E-05	2.35E-05	5.01E-06	2.93E-05
60%	2.95E-05	1.18E-05	2.10E-05	4.62E-06	2.83E-05
70%	2.57E-05	1.07E-05	2.06E-05	4.44E-06	2.61E-05
80%	1.37E-05	6.08E-06	1.39E-05	3.63E-06	1.44E-05
Al					
20%	3.25E-05	1.34E-05	8.55E-05	5.75E-06	3.48E-05
40%	2.57E-05	1.28E-05	5.77E-05	5.11E-06	3.11E-05
60%	1.85E-05	1.16E-05	2.74E-05	3.61E-06	2.68E-05
70%	1.71E-05	1.05E-05	2.66E-05	3.40E-06	2.57E-05
80%	1.53E-05	5.90E-06	1.99E-05	2.33E-06	2.00E-05

Table 9 Diffusion coefficients of metal composites in different solvents

From table 8, it can be observed that for all types of metal composites, the diffusion coefficients decrease with the increase of the volume ratio, except for the case of nickel particle composite at 80%. This observation is consistent with Spearot's study [116], which indicates that the particles in the composite obstacle the diffusion solvent penetrants through the composite. In addition, Spearot's research indicated that the diffusion coefficient of oxygen for the uncross-linked PDMS copper composites at 20% volume percentage is in the range $1\sim2\text{x}10^{-5}\text{cm}^2/\text{s}$ by using Williams-Landel-Ferry model. This number is similar to our study for the cross-linked PDMS copper particle composites at the same volume ratio in SU-8 Developer and Methanol solvents, whose values are $1.1\text{x}10^{-5}\text{cm}^2/\text{s}$ and $2.07\text{x}10^{-5}\text{cm}^2/\text{s}$, respectively. This is probably true, considering the balance between the size and concentration of penetrants. The size of molecule of 1-Methoxy-2-Propanol Acetate (SU-8 Developer) and Methanol is larger than oxygen molecule, which decreases the diffusion. However, the concentration of the solvent is larger that of oxygen (100 oxygen penetrants are introduced). It has to be mentioned that the diffusion

coefficient 1~2x10^{-5}cm^2/s from Spearot's study is very similar to the diffusion coefficient of cross-linked PDMS zeolite composites at 20% volume ratio, which number is 1.18~1.26x10^{-5}cm^2/s that is measured by Chowdhury using Fluorescence Microscopy [123].

Table 9 also shows that the smallest diffusion coefficients among the five solvents are for the IPA solvent, which is a magnitude order smaller than that for other solvents. That is true because the time constants for IPA are much larger than these for other solvents, which refers that it takes longer time for the composites to reach its steady state in the swelling process. An interesting point has to be noted that the diffusion coefficients derived from our experimental data series (~x10^{-5}cm^2/s) are two magnitude order larger than the diffusion coefficient derived from Tanaka's research for the case of Acrylamide gel which value is 2.9x10^{-7}cm^2/s. This is reasonable since the time constant from Acrylamide swelling is quite lager than our case, as shown in Figure 76 (Ref. 121). It takes about 200 minutes (in some case even longer) for Acrylamide gel to expand to its steady state. But in our case this settling time is in less than 50 minutes.

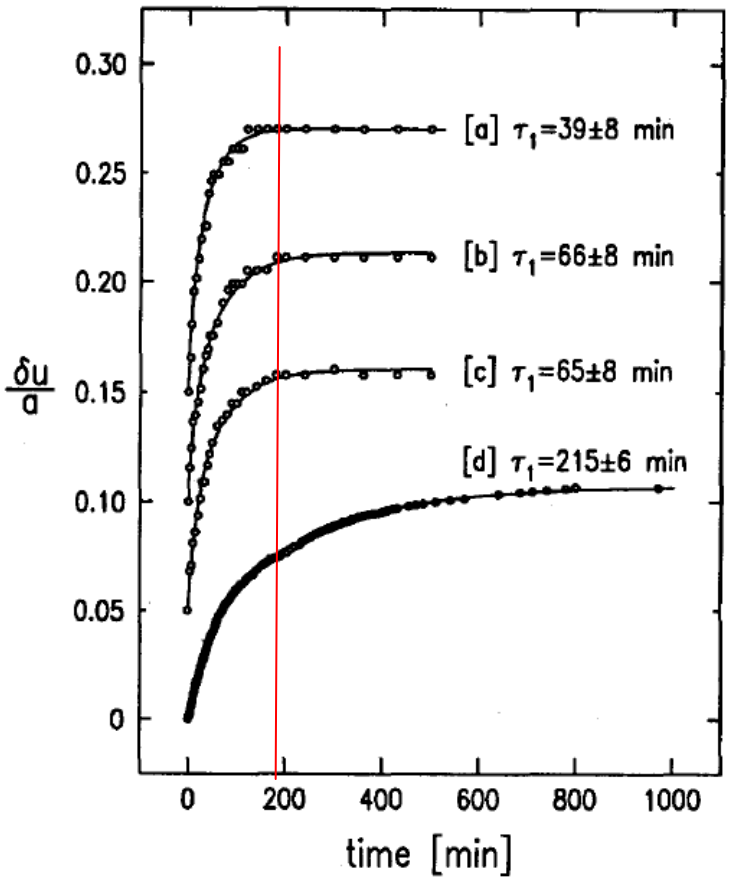

Figure 77 This figure is taken from Ref. 121. It demonstrated the measurements of the swelling process of Acrylamide gels in different shapes. (a) short cylinder with equal length and diameter. (b) long cylinder with length rougly 30 times the diameter (c) the length of the long cylinder of (b). (d) the disk. Each of the top three curves has been shifted from the one below it by 0.05 for clearness.

4.2.5 Summary

The work of this chapter is to study the diffusion of solvents through metal particle PDMS composite. The first section studies the acetic acid penetration in the copper particle composite using image scanning approach. Another purpose is to investigate the oxide removal into the mixed composites, without etching particles in advance. The diffusion can be characterized by the color intensity, which indicates the penetrating front arriving locations in the composite.

Within long time, the acid molecules can diffuse into the composite. However, it has been shown that this diffusion is a slow process. It is difficult for acetic acid to penetrate into PDMS matrix, since the polarity of the acid solvent.

Therefore, one of the purposes of the second section is to expand the composite by organic solvent to ease the penetration of acidic solvents. In addition, the diffusion mechanism of the composite PDMS has been thoroughly studied. Diffusion is studied through swelling the composite in different organic solvents. It indicates that the swelling ratio decreases with increasing particle's volume ratio. This refers that particles in the matrix obstacle the diffusion process. Accordingly, the diffusion coefficient of each composite at certain mass ratio for different penetrants has been found by using Tanaka's theory.

Chapter 5 Characterization of Electrical Properties of Metal Particles and PDMS Composites

5.1 Introduction

To measure the corrosion rate of inspected metal material, it is necessary to correlate the corrosion rate to the conductivity of the sensor elements based on the working principle of corrosion sensor. The conductivity of the composite is quite sensitive to corrosion rate. Small increase of corrosion of the metal particle indicates the conductivity decrease. This output signal can be detected by peripheral electrical device. This demonstrates the high-sensitivity of the corrosion sensor.

The mechanism of the corrosion sensor is based on the mass transport of corrosive species through the sensor matrix. As illustrated in Figure 77, when the metal particles in the matrix corrode, the electrical resistivity of the material increases due to increasing particle resistances or reduction of conducting surfaces.

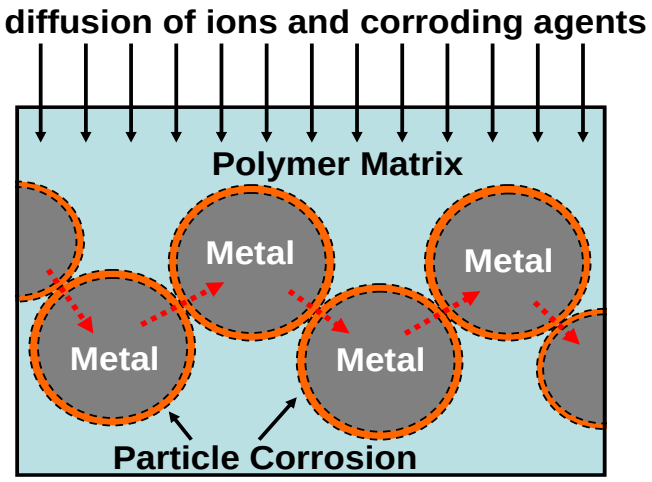

Figure 78 The corrosion mechanism of the sensor

Because the electrical path is formed by the contact of metal particles between each other in the matrix, the conductivity of the composite also depends on the mass percentage of the metal

particles (or more correctly the volume percentage). For the purpose of engineering the sensor performance, studies of mass and volume percentage of particles in PDMS versus resistivity have been conducted. The sample particles chosen in the test are carbon-black, silver-coated aluminum, and nickel particles. Carbon-black and silver-coated aluminum particles are less susceptible to oxidization and corrosion in natural environment. Therefore both can be used as the reference sensor to subtract inherent but undesired sensitivities, such as temperature and pressure. The nickel particles are then used as the target material for corrosion sensing. The particle-composite fabrication procedure encountered complications when the particle material density becomes much larger than the PDMS or when the size of the particle is on the micron-level or larger. The particles will sink to the bottom due to the gravity force acting on it, thereby cause a non-homogenous mixture. To solve this problem, a two-step curing approach to treat PDMS has been described in this section.

Another design characteristic of the MEMS corrosion sensor being developed is the inert matrix material in the form of the PDMS polymer. Since the sensor design is itself in micro-scale, the proportion of corrosive material loss of a directly exposed sensing element will be invariably fast, resulting in a reduced sensor life. Thus, the PDMS matrix material for the corrosion sensor will slow down the metal particle corrosion rate, resulting in prolonged sensor life. Furthermore, the large increase in electrical resistivity due to a small increase in particle spatial separation (or due to insulation from oxidation) provides inherent sensor amplification, counterbalancing the reduced sensor sensitivity due to the inert PDMS coating. The sensor sensitivity is also inherently increased due to the relatively large surface area of the sensing element, when compared to the traditional analogs.

5.2 Experiment and Data Analysis

In the experiment, the carbon black particle (Carbon black, acetylene, 100% compressed, diameter 45nm, 500g) and silver-coated aluminum particle (-200mesh, Ag 19-21 wt/%, diameter 74μm, 100g) particles, nickel particle (-325mesh, diameter 44mm) are purchased from Alfa Aesar® Inc. The silicone base and curing agent are purchased from Dow Corning Company. As mixing the PDMS, typically, the mixture ratio of PDMS monomer and curing agent is 10:1. After the PDMS is mixed, it is preparing to blend with particle materials. The mixed composite are squeegeed in a plastic mold using to hold the gel-like composite and to measure the resistivity. As it is shown in Fig. 78, two gold coated metal pins are inserted through two holes in the groove in the center; and the pins are used to contect with peripheral electrical circuit to measure the sample resistance. Two pins for each sample are glued on the back of the mold by using insulative epoxy glue to ensure the stable of two pins, not cause resistance measurement error. The size of the groove is 6.35x2.54x2.032mm (Length x Depth x Width). After that, the sample is cured in a temperature chamber (CSZ® Inc. MCBH) at setting temperature and time. The sample is ready to be measured. Fig. 79 shows two different samples with carbon black composite and silver-coated aluminum composite filled up, respectively.

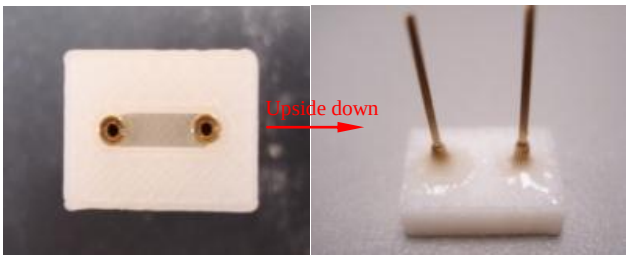

Figure 79 The first step curing time versus temperature

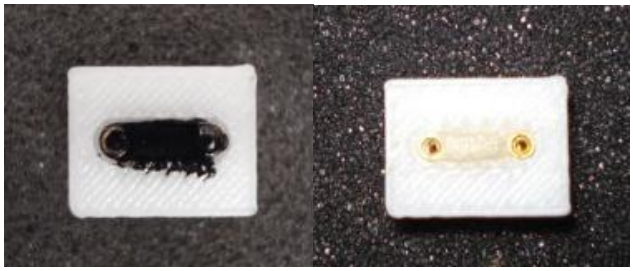

Figure 80 Sample with carbon black particles (Left). Sample with silver-coated aluminum particles (Right)

The density of carbon is 2.267g/cm^3, the density of silver-coated aluminum is 4.258g/cm^3 and the density of nickel is 8.908g/ cm^3. Each of particles is higher than the density of PDMS (1.03g/cm^3). These particles will settle down at the bottom when mixing without homogenization, which cause inaccuracy of resistance measurement. The particle's sedimentation time can be calculated by Newton's second law and Stokes' law. As shown in Fig. 3, the single particle in aqueous PDMS is sustained gravity force, buoyant force and friction force caused by the movement of particle downwards. According to the Newton's second law,

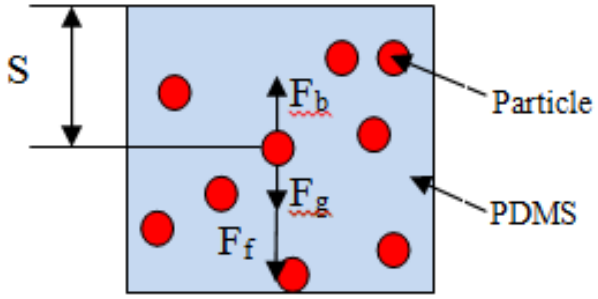

Figure 81 Particle settles down in the aquous PDMS when mixing up

$$ma = F_g - F_b - F_f \tag{43}$$

where, $F_g, F_b and F_f$ are gravity force, buoyant force and friction force, respectively. Because,

$$ma = \rho_{particle} \times V_{particle} \times \frac{d^2 s}{dt^2} \tag{44}$$

$$F_g = \rho_{particle} \times g \times V_{particle} \tag{45}$$

$$F_b = \rho_{PDMS} \times g \times V_{particle} \tag{46}$$

$$F_f = 6 \times \pi \times \mu_{PDMS} \times R_{particle} \times V = 6 \times \pi \times \mu_{PDMS} \times R_{particle} \times \frac{ds}{dt} \tag{47}$$

and Stokes' Law

Where, *m* is the mass of single particle; *a* is the acceleration of the particle; g is the gravity acceleration; $\rho_{particle}$ is the density of the particle; ρ_{PDMS} is the density of PDMS; $V_{particle}$is the volume of single particle; μ_{PDMS} is the viscosity of PDMS; $R_{particle}$is the radius of a particle and V is the sedimentation velocity of particle. Combine the five equations above, equation (43) can be written as:

$$\rho_{particle} V_{particle} \frac{d^2 s}{dt^2} = \rho_{particle} g V_{particle} - \rho_{PDMS} g V_{particle} - 6\pi\mu_{PDMS} R_{particle} \frac{ds}{dt} \tag{48}$$

Solving this second order linear derivative equation, the general solution is,

$$\frac{1}{6\pi\mu_{PDMS} R_{particle}} [-C_1 \rho_{particle} V_{particle} e^{-\frac{6\pi\mu_{PDMS} R_{particle}}{\rho_{particle} V_{particle}} t} + g V_{particle} (\rho_{particle} - \rho_{PDMS}) t + 6\pi\mu_{PDMS} R_{particle} C_2] \tag{49}$$

For this case, the initial displacement is 0 and the initial velocity is 0 as well. The boundary condition is listed as S(0)=0; S'(0)=0. According to the initial conditions constant C1&C2 can be solved so that every type of particles' sedimentation time can be calculated by equation (49). For instance, the silver-coated aluminum, the diameter is 74 μm; the density is 4.258g/cm^3, which is calculated by Ag 20 wt/ %, the density of silver is 10.49g/cm^3 and the density of aluminum is 2.70g/cm^3, respectively. μ_{PDMS} is the viscosity of PDMS (4.575Pa•s). Using the known parameters and two boundary conditions, the sedimentation time versus distance can be plot as shown in fig. 81. The depth of the sample holder in the experiment is S=2.54mm, from the graph, it indicates that the silver coated aluminum particle will take 1206s (20.1min) to sediment onto

the bottom completely, which means the sample cannot be homogenously mixed up in making serial different mass percentage samples of which the process will take more than 2 hours.

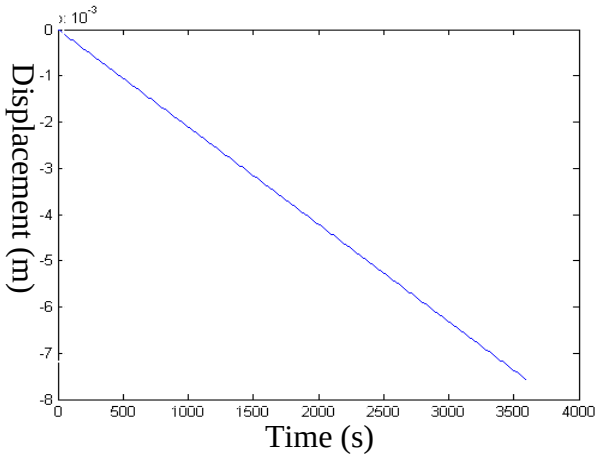

Figure 82 Sedimentation time versus displacement

To prevent particle settle-down, a two-step curing approach is used to process PDMS. The first curing step generates crosslink in PDMS matrix to increase the viscosity of PDMS. Then particles are well mixed with PDMS easily without the settle-down problem. Because of the high viscosity resulting particles hardly settle-down, the homogenous composite can be formed. The formation of cross-link in the matrix is not reversible, which will not increase the total curing time of PDMS. The time of the first curing step and the time of complete curing by different temperature are shown in Fig. 82 (the weight of PDMS in the test is 2.0g).

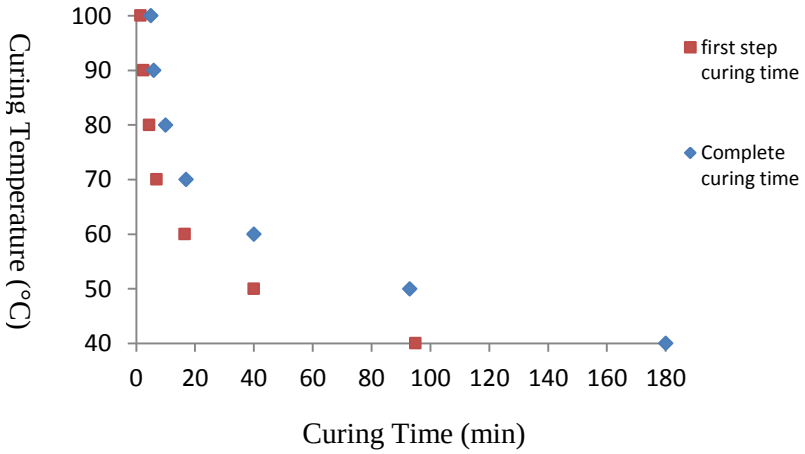

Figure 83 The first step curing time versus temperature

A simple calculation by applying the equation (49) indicates the change of viscosity tremendouly affects the length of sedimentation time. We increase the viscosity 50% each time and plot the serial graphs in Fig. 83. It shows that the viscosity is an important parameter to affect the sedimentation time. In further work, an experiment will be done to measure the viscosity of PDMS by different curing time for quantifying the results.

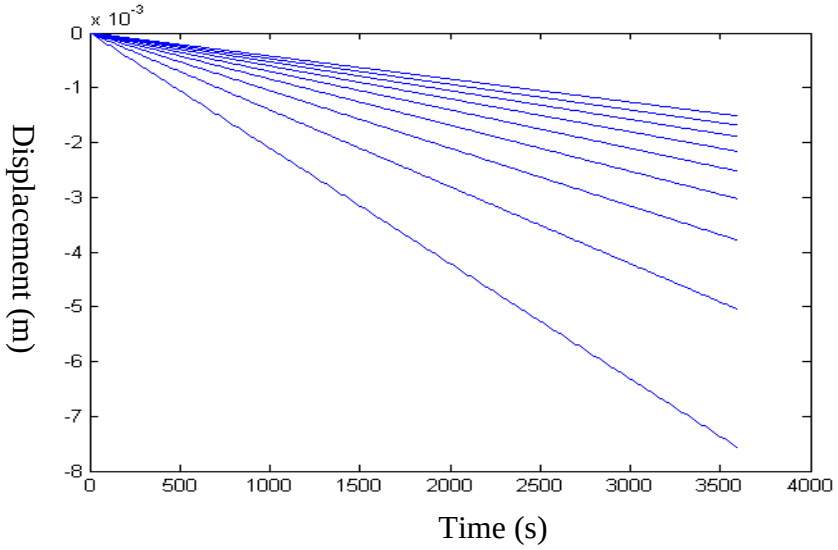

Viscos
4.575
6.8625
9.15
11.437
13.725
16.012
18.3
20.587
22.875

Figure 84 Sedimentation time versus displacement

For the sample holder used in this experiment, the depth of which is 2.54mm. For this constant displacement, increasing viscosity of PDMS will significantly improve the sedimentation problem. Fig. 84 displays the graph of displacement versus sedimentation time. The sedimentation time increases almost linearly accompany with the increase of the viscosity of PDMS. The graph also proves that the two-step curing approach do help solve the sedimentation so as to obtain homogenous mixing sample.

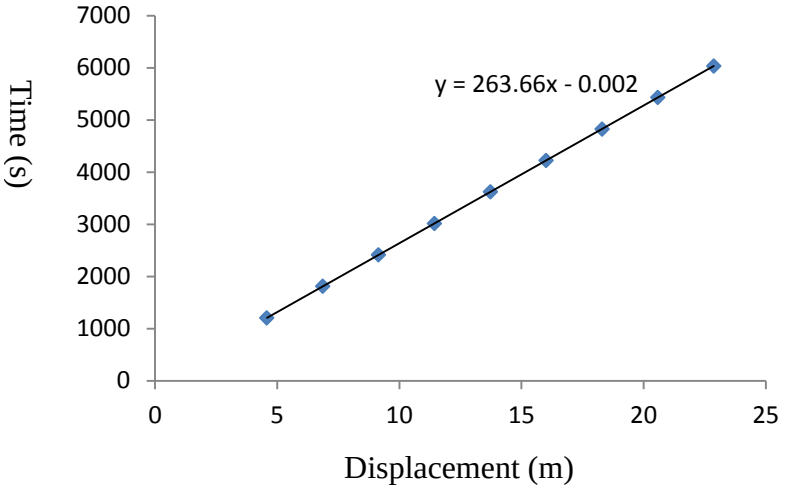

Viscosity(Pa.s)	Time (s)
4.575	1206.23
6.8625	1809.35
9.15	2412.47
11.4375	3015.58
13.725	3618.70
16.0125	4221.82
18.3	4824.93
20.5875	5428.05
22.875	6031.17

Figure 85 Displacement (m)

5.3 Resistivity Measurement

Using the two-step curing process, the resistivities of three different metal particles are experimentally derived as a function of mass and volume percentages. The formulas below are used to calculate the mass and volume percentages, respectively.

$$\boldsymbol{Mass\ percentage} = \frac{\boldsymbol{Mass\ of\ particles}}{\boldsymbol{Mass\ of\ particles + Mass\ of\ PDMS}} \quad (50)$$

$$Volume\ percentage = \frac{Volume\ of\ particles}{Volume\ of\ particles + Volume\ of\ PDMS} \quad (51)$$

According to the dimension of the groove and the measured resistances, the electrical resistivity ρ can be calculated by,

$$\rho = R\frac{A}{l} \quad (52)$$

Where ρ is the electrical resistivity (measured in ohm-meters, Ω cm); R is the electrical resistance of the sample (measured in ohms, Ω); l is the length of the groove (measured in meters, cm); A is the cross-sectional area of the groove (measured in square meters, cm^2).

For the carbon black particle samples, the resistivity versus mass percentage and the resistivity versus volume percentage are plotted in Figure 85 and Figure 86, respectively. Figure 18 shows that for the mass percentage 11%-20%, the resistivity decreases when the carbon particle mass percentage rises. Once the mass percentage is below 11%, the resistance becomes too high to be measured by our instrument (>20MΩ). On Figure 86, the same data as those in Figure 85 is converted to volume percentage using the nominal diameters of the particles given by the manufacturer. The trend of data points obeys the power law as usually observed in percolation phenomenon [110], which means a small change of mass (volume) percentage will cause a large change of resistivity. For example, when carbon particle mass percentage increases from 12% to 13%, the resistivity will increase 7.25×10^4 Ω.cm. That indicates the sensor sensitivity can be guaranteed even with the PDMS barrier.

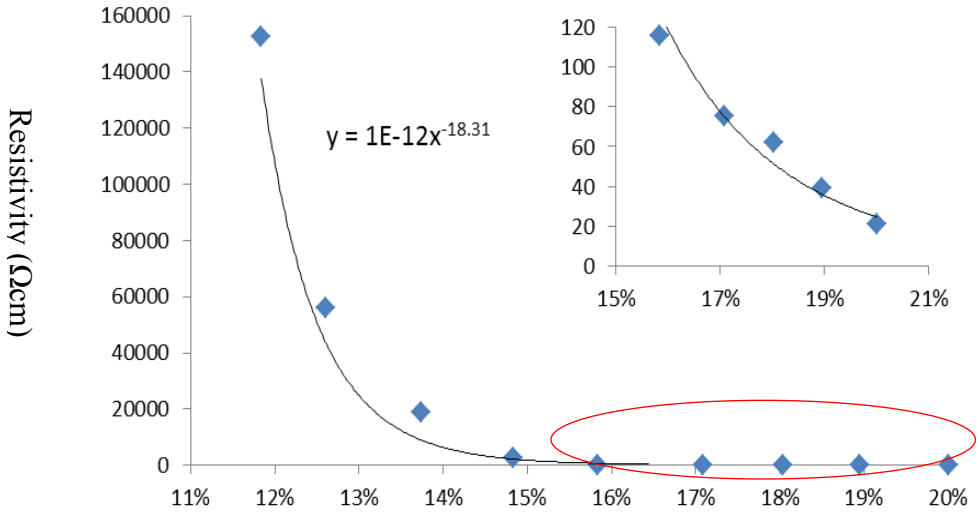

Figure 86 Resistivity versus mass percentage of carbon black particle

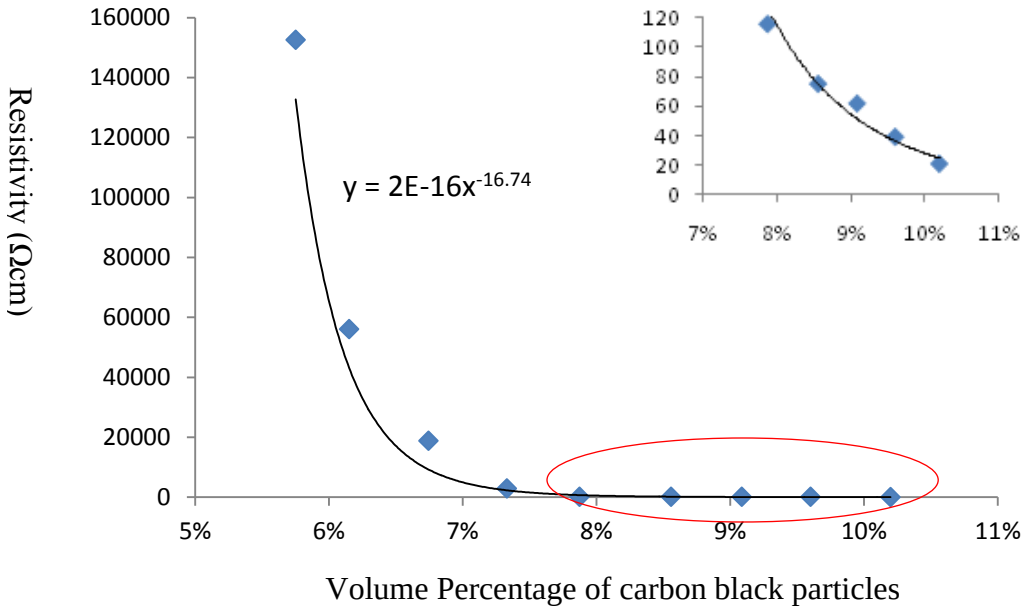

Figure 87 Resistivity versus volume percentage of carbon black particle

Figure 87 and Figure 88 show the resistivity versus mass percentage and the resistivity versus volume percentage of silver-coated aluminum particle samples, respectively. The mass percentage is from 50% to 70%, and the interval is 5%. Figure 87 indicates that there are no measurable resistivity values below 60% percentage. However, once the mass percentage reach above 60%, the resistivity suddenly becomes extremely low. After reaching 65%, the resistivity stays nearly constant. The power law fit here is not as good as the carbon black particles, which warrants more detailed investigations in the future.

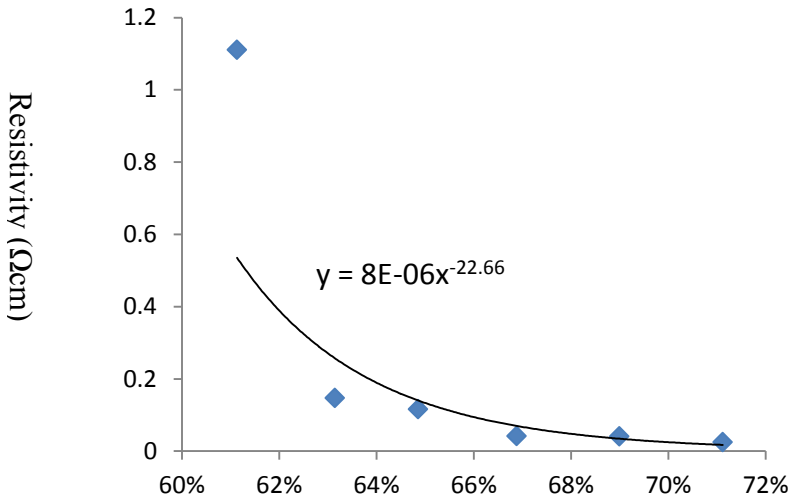

Figure 88 Resistivity versus mass percentage of silver-coated aluminum particle

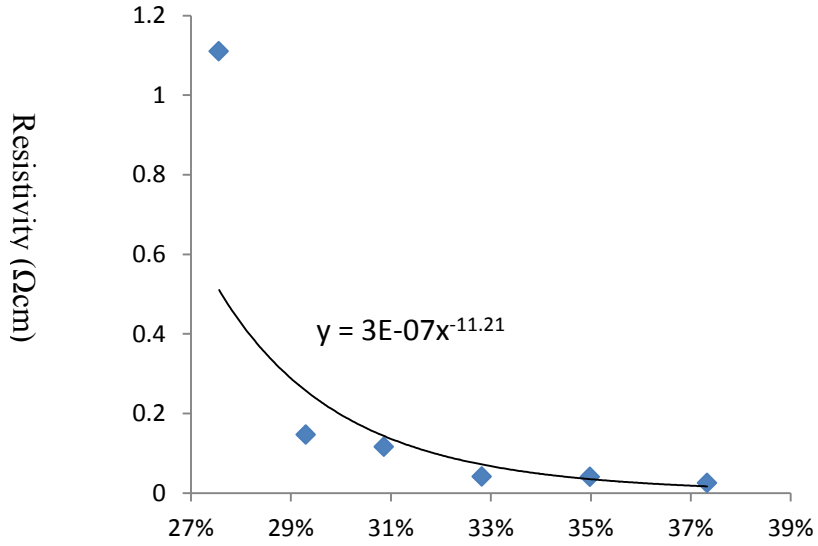

Figure 89 Resistivity versus volume percentage of silver-coated aluminum particle

Figure 89 and Figure 90 are graphs of nickel particle composite resistivity versus mass and volume percentage. The mass percentage is from 60% to 80%, and the interval is 5%. Figure 89 indicates that there is no measurable resistivity below 60% percentage. However, as the mass percentage reach to 60%, the resistivity value is larger than silver-coated aluminum sample at the

same mass percentage. The data points also obey power law thus a large sensor sensitivity value can be expected.

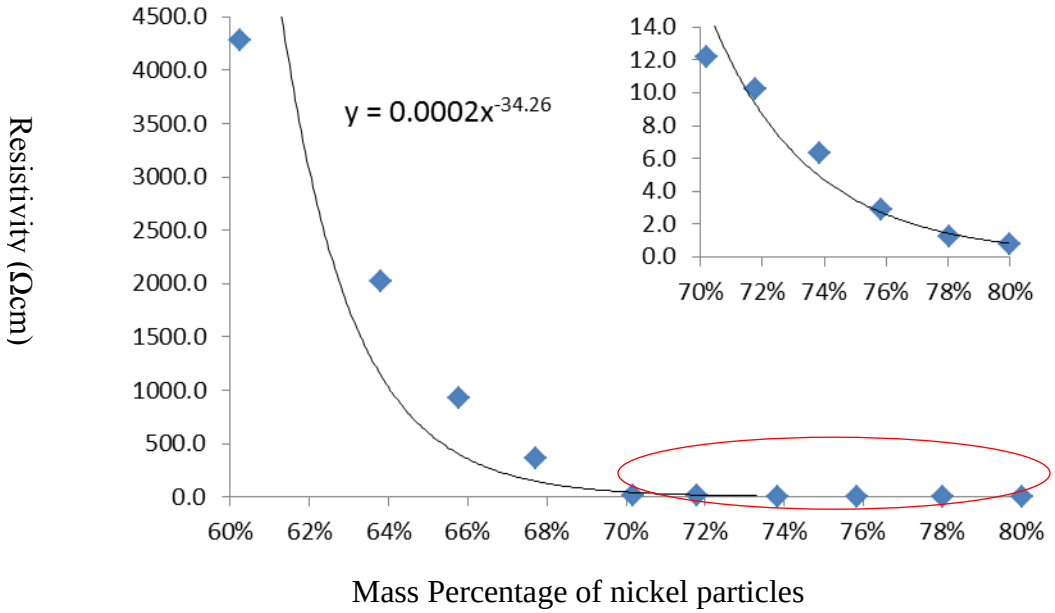

Figure 90 Resistivity versus mass percentage of nickel particle sample

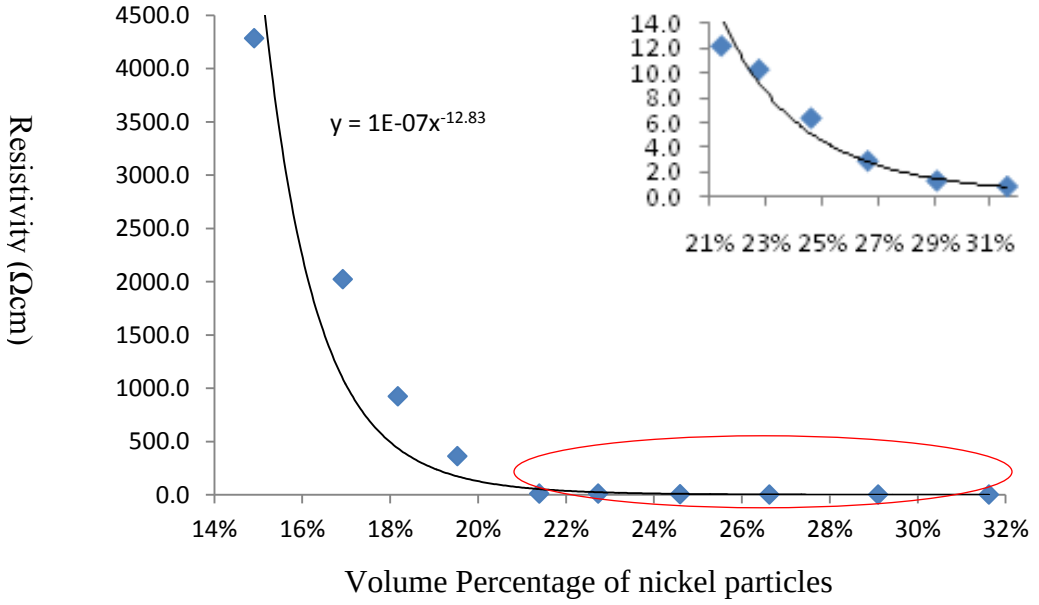

Figure 91 Resistivity versus volume percentage of nickel particle sample

The above experiments show the electrical resistivity of the sensor element relative to metal particles' mass and volume percentages to Polydimethylsiloxane (PDMS) matrix. Three types of

particles carbon black, silver-coated aluminum and nickel were tested. The graphs of resistivity versus mass and volume percentage of each of three type particles are shown. The reason of investigating the resistivity by different mass or volume percentage of metal particle is to provide engineering guidelines in future corrosion sensor development. It also presents the solution to the sedimentation problem of metal particles in liquid PDMS in mixture and curing process. It was shown that manipulating the viscosity of the PDMS is a practical method in eliminating sedimentation.

5.4 Removal of Oxide on Metal Particles

To make the corrosion sensor work, the embedded metal particles should form current paths through insulated polymer matrix so that the resistance change due to corrosion can be detected by ER technique. However, since the micro/nano size of metallic particles and thus its large surface to volume ratio, these non-noble metallic particles are easy to be oxidized as exposure to ambient environment. The oxide of metal particles is often disadvantageous for the electrical conductivity and sensitivity of the corrosion sensor. Due to the relatively large surface area to volume ratio of nano- and micron-sized particles, any changes in the surface property will dominate the electrical characteristics of the metal particle polymer composite.

An oxide removal approach based on the wet etching process is provided. Diluted hydrochloric acid is applied to react with the oxidized coating of the metal particles (e.g. nickel). The resulting chemical reaction is a soluble metal chloride solution that is repeatedly diluted and dumped by IPA (Isopropyl alcohol) solvent, which prevents re-oxidization of the metal particle while immersed in the solution. The remaining pure metal particles are then collected and baked and then used in the sensor fabrication.

5.4.1 Experiment

In this experiment, nickel particle is used to do the preliminary test. Nickel oxide reacts with hydrochloric acid easily. The generated nickel chloride is soluble in water. Moreover, nickel chloride does not react with IPA solvent, which means the nickel chloride is rinsed out without further reaction to the bare metal particles. Nickel particles (-325mesh, typically 99.8% <metals basis>) used in the experiment are sourced from Alfa Aesar® Inc.

The first step is to dilute the hydrochloric acid (wt 36.5%; EMD Chemicals, Inc.) to a 100mL solution of 0.01mol/L concentration with de-ionized water. Then, 0.5g of the nickel particles are added in the solvent. The nickel oxide reacts with hydrochloric acid, which has the following chemical equation (24):

$$NiO + 2HCl \rightarrow NiCl_2\,(\text{soluble}) + H_2O \quad (53)$$

$$Ni + \ 2HCl \rightarrow NiCl_2\,(\text{soluble}) + H_2\,(\text{gas}) \quad (54)$$

Initially, the color of solution will change to green gradually, which is the color of $NiCl_2$. After 15minutes, there are bubbles coming out from the bottom, which means the hydrochloric acid starts reacting with the pure nickel and the gas is hydrogen molecules, as indicated in equation (53). The reaction is sustained for 90min in order to be sure of removing all nickel oxides. Then the nickel particles are prepared for rinsing, drying, and collection.

The key to success in this experiment is to prevent the pure nickel particles to be exposed in the air and be oxidized again. A glove box is set up to achieve the necessary protective environment. A sealed glove box with bleeding valve is filled up with nitrogen gas (concentration 99.5%, welder's grade). The dumping and rinsing of the residual solution by using IPA solvent 4 times is used to dilute and remove the nickel chloride solution. Then the particles are poured on a filter paper and baked on the hotplate at 80°C for 1 hour in the glove

box to vaporize the residual IPA mixure with nickel particles. The mass of collected nickel particles is about 0.22-0.31g, representing roughly 50% mass loss. Because the process is operated in a nitrogen gas environment, these nickel particles cannot be re-oxidized. The deoxidized particles are then mixed with PDMS at varying mass percentages to measure the resistivity of the samples and compare to the same mass percent nickel particle samples to investigate the quality of the de-oxidizing experiment.

For the deoxidized nickel particle sample, the resistivity versus etching time is plotted in Figure 91, which shows that, at mass percentage of 70%, with the etching time 15-90min, the resistivity decreases when the etching time increases. Once the etching time is above 90min, the resistance becomes fairly constant. When the etching time reaches to 90min, sample resistivity decreases to 0.66Ωcm.

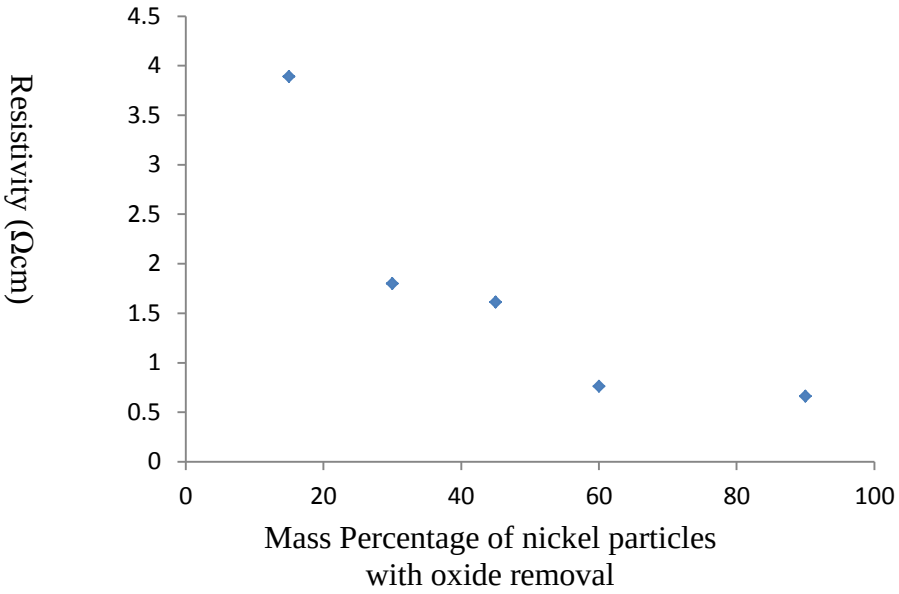

Figure 92Resistivity versus mass percentage of nickel particles with oxide removal process

Figure 92 shows the resistivity versus mass percentage and the resistivity versus volume percentage of nickel particle without de-oxidation, respectively. For Figure 92, the mass percentages are in the range from 60% to 80%, and the interval is 2%. Figure 92 indicates that

there is no measurable resistivity below 60% percentage. However, for the samples with oxide removal, at 70% (etched by only 15min) the resistivity decreases down to 3.89Ωcm. On the other hand, at 70% for particles that was not 151ransg, the resistivity value is 11.9Ωcm, which is much higher comparing to the resistivity of the sample with oxide removal process at the same percentage, 3.89Ωcm. This result demonstrates that oxide removal process do improve the electrical transduction of the composite.

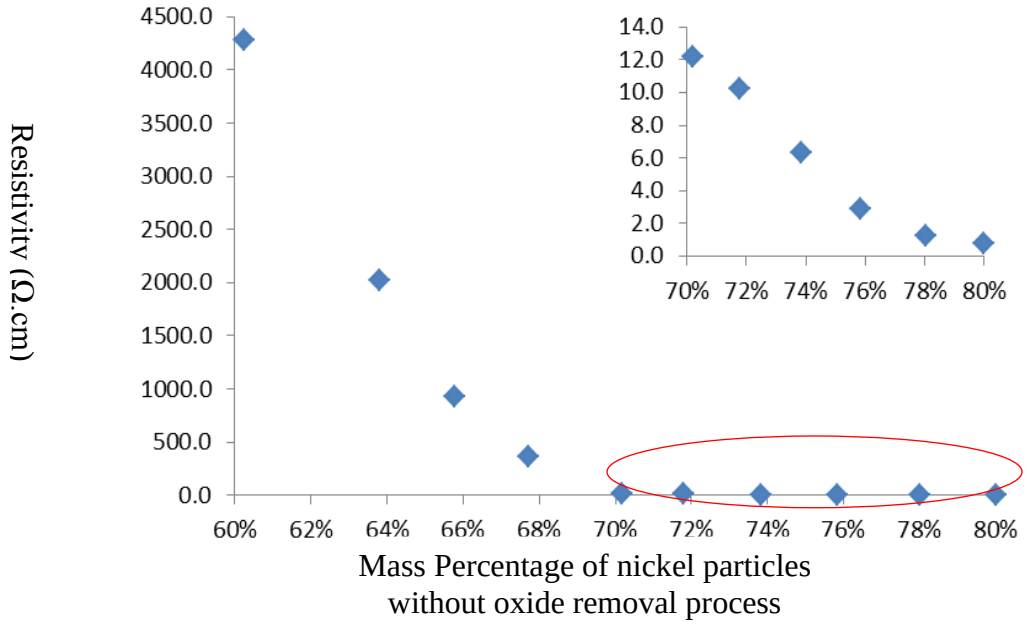

Figure 93 Resistivity versus mass percentage of nickel particles without oxide removal process

This section provides an approach to solve the oxidation problem of metal particles. Chemical wet etching is the main process applied in this approach. After de-oxidization, these fresh metal particles are rinsed and baked in nitrogen gas environment to prevent oxidizing again. Then the conductivity of nickel composite sample is investigated. The comparison to nickel particle sample without de-oxidation are presented, demonstrating that the deoxidized nickel performs better in terms of lower conductivity.

Based on the prior experiment, the most difficult part of this project to incorporate into PDMS matrix with native metallic particles from which all metal oxide has been removed, but

preventing oxidization again. There are various approaches to remove oxide by using wet or dry etching. However, it is quite hard to achieve the goal that prevent metal particle to be oxidized again, especially in common laboratories. In the following experiment, the investigation of using supercritical carbon dioxide to swell PDMS and particle composites will be study. The supercritical carbon dioxide can expend the volume of PDMS and make acidic species readily flow in the matrix and access to the oxide layers of embedded metal particles. After reaction, metallic irons will be taken out by the species flow. And then expelling carbon dioxide, PDMS will contract to its original size. The advantages of the approach are as follows. First, the experiment is operated in oxygen insulated environment; second, PDMS will work as a barrier to keep oxygen out of touching metal particle after carbon dioxide expelling. The details of swelling PDMS using supercritical carbon dioxide will be discussed later in the proposal.

5.5 Resistance Measurement of Composite Disk after Swelling and Etching

To reduce the resistance of the composite, there is another approach that is to mix the oxidized particles with PDMS and then reduce the resistance of the total composite by swelling it and react with oxides by using solution that is combined organic and acidic solvents. From chapter 4, it has been known that Toluene has the highest solubility to PDMS and soluble to acetic acid; IPA has modest solubility to PDMS and is soluble to HCl. Therefore we use Toluene and IPA as the swelling agent. From this chapter, it has been known that only composites in high mass ratio have measurable resistance. We perform the diffusion-reaction in the same settling as that has done in diffusion investigation. Figure 93 is a typical expansion graph of the diffusion-reaction process. The example illustrates the 70% w/w copper particle PDMS composite linear expansion in Toluene and acetic acid. First the sample disk is immersed in Toluene solvent only, for 40 minutes. Then add acetic acid into the solution for 540 minutes to remove copper oxide.

Figure 94 shows the cross section of the composite disk after 540min etching. Note while acetic acid is added in, two images taken are interrupted and not plotted in the graph. For this test, 20ml Toluene and 20 ml acetic acid are used. From figure 93, it can be seen that after acetic acid is added the expansion reduces suddenly from its maximum, 16%, in 20 min to reach to the bottom 6%. Then gradually rise up to 11%. Since the density of acetic acid (1.05g/cm^3) is larger than the density of Toluene (0.866g/cm^3), once acetic acid is poured in the beaker, it expels Toluene and surrounds the composite at the bottom, which results in the shrinking of the sample. Later, Toluene and acetic start to penetrate with each other, so the expansion gradually grows. The purpose here is not to investigate the expansion of the combined solution. The purpose is to swell the composite and removal metal oxides.

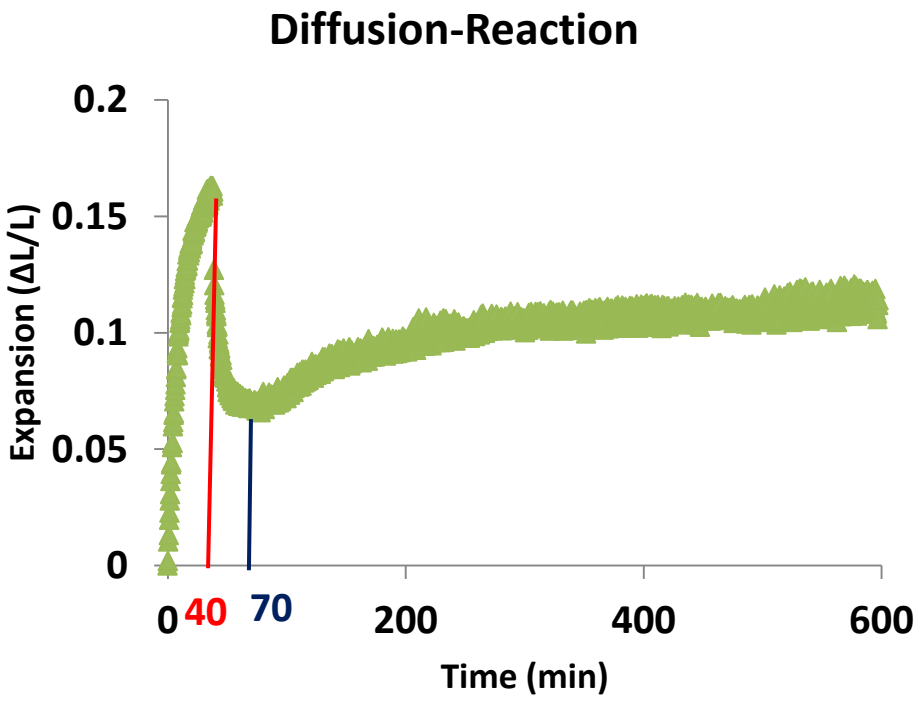

Figure 94 Diffusion-Reaction process in 70% w/w copper PDMS composite

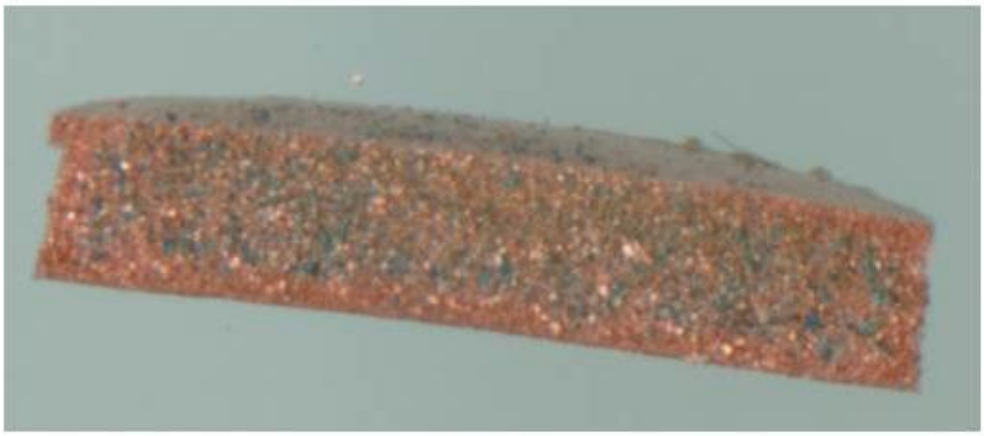

Figure 95 Cross section of the disk composite (70% w/w copper PDMS)

The resistances of samples with different metal particles and different mass percentages have been measured. The samples were expanded and etched by the time periods of 1hour, 8 hours and 18 hours. Then these samples were dried by vacuum process, up to 25 militorr for four hours and then use four-point measurement to measure the surface resistance in 3mm distance. It should be mentioned that there is no measurable resistance for all samples before they are processed in expansion and etching.

The expansion solvent employed is IPA (25ml) for the reason that it can be soluble with either HCl (10ml) or Acetic acid (10ml) solvents. HCl solvent is used to remove the oxides of aluminum, nickel, iron and stainless steel particles. Acetic acid solvent is applied to etch copper oxide.

Different metal particle samples presented different resistances. For aluminum composites, there exits measurable resistance as the particle/PDMS mass percentage is higher than 60%. For the three types of samples with mass percentages 60%, 70% and 80%, their resistances are in the range of 11MΩ, 5MΩ and 1MΩ according to the three etching time periods. For copper composites, only 80% has measurable resistance, the value is in the range of 1100K. For iron particle-PDMS composites, two types of samples, 70% and 80%, have measurable resistances in the range of 7MΩ and 1MΩ respectively. For nickel composites, four different sample

resistances (40%, 60%, 70% and 80%) can be measured. The resistance values are falling in the range of 15MΩ, 5MΩ, 0.8MΩ and 31kKΩ, respectively. For stainless steel composites, the three samples with mass percentages of 60%, 70% and 80%, their resistances range within 26MΩ, 1MΩ and 300KΩ.

It can be seen that the resistances of samples vary from hundreds of thousands ohms to tens of mega ohms by reducing mass ratio of metal particles.

5.6 Summary

In this chapter, we discuss mainly three portions in electrical property investigation. First, the sedimentation of metal particles in the uncross-linked PDMS has been modeled and the problem has been solved experimentally by adding a pre-cure procedure before mixing particles with PDMS in order to increase the viscosity of the PDMS bulk. Second, the resistivity of different metal composites has been studied. Two approaches can be used to remove metal oxides. Etch particles first and then mix with PDMS; or vice versa. The corresponding resistivity or resistance change with mass percentage has been demonstrated.

Chapter 6 Conclusion and Future Work

6.1 Conclusion

This dissertation described three key objectives in the development of MEMS based corrosion sensor: Microfabrication technology, Diffusion mechanism and Electrical properties of the sensing material.

DPPOST approach is established to fabricate the PDMS based sensor. This approach solves the difficulty to directly pattern PDMS polymer, which is un-photo-patternable polymer. In addition, its modified approach is also presented to improve the yield toward 100%. This modification employs double layer of Omnicoat™ to serve as barriers to reduce the stiction between the deposited PDMS and the SU-8 mold. To optimize the modified approach and control the thickness of the barriers, oxygen etching rate has been tested. Also the vapor priming used to deposit thin Omnicoat™ coating has been investigated. The thickness obtained by this approach can be in nanometers.

The diffusion mechanism is the basis of corrosion and sensing monitoring, which is the key aspect of the research project. We investigate the solvent diffusion through the composites by using image scanning approach. It shows that by detecting the color intensity of the scanned image of the sample, the diffusion rate can be found. The diffusion front can be observed clearly by using this method. The penetrants diffuse into the composite by increasing the diffusion time. The reaction after the diffusion has also been detected.

The diffusion mechanism can also be studied by the expansion of the metal particle and PDMS composites. The swelling kinetics of five different metal composites with different mass ratio in organic solvents has been described. It has been found that with the increase of metal particle mass ratio, the expansion degree decreases. The expansion degree is affected by the

volume ratio of metal particles in the composite. Larger volume ratio of metal particles provides smaller expansion. Different solvents provide different solubility to the PDMS. Toluene swells the composite to the maximum degree among the five solvents and methnol swells it to the minimum degree. The swelling behavior in Acetone is different with others. The composites shrink after reaching the maximum expansion due to the extraction effect. The swelling rate is also related to the metal particle volume ratio: high volume ratio, less swelling rate. The only exception is for the case of nickel particle composite at w/w 80%, where the swelling rate is very high due to the free space created in the bulk. Based on the swelling rate, the diffusion coefficients of all types of composites in the five solvents have been calculated by using Tanaka's theory. This is the first work that has been done to investigate the diffusion coefficients of metal particle PDMS composites in organic solvents.

To characterize sensing materials, the electrical properties of the metal particle PDMS composites have been investigated. The resistivity of the composites decreases with the increase of particle mass ratio. The trend of resistivity decrease obeys well the percolation theory. To reduce the resistance of the initial sensing material, oxide removal has been performed and investigated. By etching the particles before mixing with PDMS, the resistivity largely decreases. To prevent re-oxidation of particles, these metal particles can be mixed with PDMS to form the bulk of sensing structure and then remove the oxides layers on the particles which have been embedded in the PDMS matrix. The resistance decreases with long soaking time. This process can be well controlled by the expansion and diffusion mechanism that is discussed in chapter4. In addition, the sedimentation of metal particles in the PDMS liquid has been solved by theoretical and experimental approaches.

6.2 Future Work

After completing fabrication of the micro corrosion sensor, the nest task is to test its performance, such as sensitivity and life-span, under various environments based on laboratory test conditions. Also, it is necessary to correlate corrosion rate to sensor resistivity change with the assistance of reference coupons. The sensor test can be operated in atmosphere condition with adjustable temperature and humidity. To extensively simulating the temperature and humidity in field, the test would be performed in temperature range from -30°C to 80°C and humidity range covering 45~85%. Since this sensor is expected to monitor corrosion in long life span and it may take too long time to finish the whole test in atmosphere condition, its performance test also will be run in salt spray chamber following the ASTM B117 of the standard salt fog practice. This standard practice requires the formation of frog in such a way that for each 80cm^2 of horizontal area there are collected from 1.0 to 2.0ml of solution in at least 16 h from the 5% m/m salt solution. The ascot® salt spray test chamber in our lab provides excellent salt frog conditions to satisfy the ASTM B117 standard. In addition, sensor corrosion test in slat fog environment can be run with complementary coupons having exactly the same metal material as that in the sensing element to correlate the function of sensor to the corrosion rate of the infrastructure material and thus correlate the advanced lab-made micro corrosion sensor to the practical field monitoring. All the tests can be operated in the way of online or offline monitor. It has to be noted that when testing sensor in salt spray, the exposed metallic layers on the sensor chips should be coated with protective film to prevent its corrosion and malfunction in the corrosive environment.

References

[1] G. Schmitt, M. Schütze, G. F. Hays, W Burns, En-Hou Han, A. Pourbaix, G. Jacobson, World Corrosion Organization, White Paper, 2009

[2] Nowlan FS., Heap HF. AD-A066-579. U.S. Department of Commerce, National Technical Information Service. 1978.

[3] Revie RW., Corrosion Inspection and Monitoring. John Wiley&Sons Inc. New York, 2007

[4] 4X-AXG Boeing 747-258F El Al 04.10.92 Bijlmermeer. Accident report 92-11. 1992. Amsterdam, the Netherlands, Netherland Aviation Safety Board.

[5] HAMER M. Clampdown on the Rust Buckets. New Scientist 1991; 146: 5.

[6] Schueller R. SMTA int'l Proceedings, Orlando, FL Oct. 2007

[7] Veale R. SMTA 2005

[8] STAEHLE RW. Lifetime Prediction of Materials in Environments. In: Revie RW, ed. Uhlig's Corrosion Handbook. New York: Wiley-Interscience, 2000

[9] ROBERGE PR. Handbook of Corrosion Engineering. New York: McGraw-Hill, 2000

[10] Fontana M.G. Corrosion Engineering, New Delhi McGraw, 2005

[11] Bockris J O'M, Reddy A.K.N., Modern Electrochemistry, New York, Plenum Press, 1970.

[12] Haney E.G., Materials Performance, 1982;21:44.

[13] Schafer G.J., Foster P.K., J. Electrochem. Soc., 1959;106:468.

[14] Riggs O.L., Hutchinson M., Corrosion, 1960;16:94.

[15] Honnaker L.R., Chem. Eng. Progra., 1958;54:79.

[16] Nelson G.A., NACE 1967.

[17] Bakish R., Kern F., Corrosion, 1960;16:89.

[18] Hudak S.J., Page R.A., 1983;285.

[19] Johnson H.H., Schneider E. J., Troiano A.R., Trans. AIME 1958;212:526.

[20] Turn J.C., Wilde B.E., Troiano C.A., Corrosion, 1983;39:364.

[21] Bullard, S. J., Corrosion, 2003; No. 03371. NACE International, Houston, Tex.

[22] Covino, Jr., B. S., Corrosion, 2004; No. 04157. NACE International, Houston Tex.

[23] Kane, R. D., Hydrocarbon Processing. 2006; 99

[24] Alawalia, H., Report Prepared for the NACE Technical and Research Committee (TRAC) and Technical Coordinating Committee (TCC), 2006; NACE International, Houston, Tex.

[25] Kane, R. D., Corrosion, 2003; No.03175. NACE International, Houston, Tex.

[26] Kane, R. D. and Trillo, E., 2004; Corrosion, 2003; No. 04656, NACE International, Houston Tex.

[27] Eden D. A. and Srinivasan, S., Corrosion, 2004; No.04059, NACE International, Houston Tex.

[28] Kane, R. D. and Campbell, S., Corrosion, 2004; No.04579, NACE International, Houston Tex.

[29] Covino, Jr., B. S., Corrosion, 2006; No.06472, NACE International.

[30] Eden, D. C. and Kintz, J. D., Corrosion, 2004; No. 04238, NACE International, Houston Tex.

[31] Yamamoto, K., Corrosoin, 2006; No.06211, NACE International.

[32] Apel, U. et al. IEEE Trans. Electron Devices,1991, 38, 1655.

[33] Bong, A., J. Electrochem. Soc., 1971; 118, 401.

[34] Choi, W-S., Smits, J. G., J. Microelectromech. Syst.,1993; 2, 82.

[35] Greenwood, J. C., J. Electrochem. Soc.,1969; 116, 1325

[36] Han, H., Weiss, L. E., Reed, M. L., J. Microelectromech. 1992; Syst., 1, 37

[37] Hanneborg, A., Nese, M., Jakobsen, H., Holm, R., J. micromech. Microeng., 1992; 2, 117.

[38] Farooqui, M. M., Evans, A. G. R., J. Microelectromech. Syst., 1992; 1, 86.

[39] Gardner, J. W., Microsensors: Principles and Applications, John Wiley & Sons, Chichester. 1994

[40] Guckel, H., Sniegowski, J. J., Christenson, T. R., Raissi, F., Sensors and Actuators A, 1990; 346, 21.

[41] Hirano, T., Furuhata, T., Gabriel, K. J., Fujita, H., Technical Digest of 6th Int. Conf. Solid-State Sensors and Actuators, 1991; 63.

[42] Hirano, T., Furuhata, T., Gabriel, K. J., Fujita, H., J, Microelectromech. Syst., 1992; 1, 52.

[43] Billmeyer F. W. Textbook of polymer Science. John Wiley & Sons Inc. New York. 1984.

[44] Moretto H. H., Schulze, M., Wanger, G., Ind. Polym. Handbook, 2001.

[45] Centre Europeen des Silicone, 2002; http://www.silicone-europe.com

[46] Voronkov M.G., Mileshkevich V.P., Yuzhelevskii Y. A., Studies in Soviet Science. The Siloxane Bond. Plenum Press, New York 1978.

[47] Hurd C.B., J. Am. Chem. Soc. 1946; 68:364

[48] Rochow E.G., Leclair H.G., J. Inorg. Nucl. Chem. 1955; 1:92.

[49] Eaborn C., Organosilicon Compounds, Academic Press, New York. 1978

[50] Smith A. L., In the Analytical Chemistry of Silicones. Wiley Interscience, New York. 1991

[51] Noll W., Chemistry and Technology of Silicones, Academic Press, New York, 1968.

[52] Graiver D., Farminer K. W., Narayan R. J., poly. Environ. 2003; 11:29.

[53] Bruins P.F., Silicone Technology, Interscience Publisher, New York, 1970.

[54] Crank J. The mathematics of diffusion, 2nd ed. Oxford: Clarendon Press, 1975.

[55] Cussler EL. Diffusion, mass transfer in fluids systems, 2nd ed. Cambridge: Cambridge University Press, 1997.

[56] Fick A. Ann Phys 1855;170:59.

[57] Qin W, Shen Y, Fei L. Chin J Polym Sci 1993;11:358.

[58] Crank J, Park GS. Diffusion in polymers, London: Academic Press, 1968.

[59] Auerbach J, Miller W.R., Kuryla W. C., Gehman S.D., J Polym Sci 1958; 28:129.

[60] Barrer R.M.， Skirrow G., J Polym Sci 1948;3:549.

[61] Stern S.A.， Shah V.M.， Hardy B.J., J Polym Sci， Polym Phys Ed 1987;25:1293.

[62] Nakagawa T.， Fujiwara Y.， Minoura N. J Membr Sci 1984;18:111.

[63] Lee C.L.， Lee C.H.， Chapman H.L.， Cifuentes M.E.， Lee K.M.， Merill L.O.， Ulman K.C.， Venkataraman K., Proceedings of the Fourth BOC Priestley Conference， Leeds，1986. London: The Royal Society ofChemistry， 1986; 364.

[64] Berens A.R.， Hopfenberg H.B., J Membr Sci 1982;10:283.

[65] BrownW. R.， Park G.S., J Paint Technol 1970;42:16.

[66] Steingiser S.， Nemphos S.P.， Salame M., Encyclopedia of chemicaltechnology，vol. 3. New York, Wiley Interscience， 1978.

[67] Fujita H.， Kishimoto A.， Matsumoto K., Trans Faraday Soc 1967;56:424.

[68] Prager S.， Bagley E.， Long F.A., J Am Chem Soc 1953;75:1255.

[69] Kim D.， Caruthers J.M.， Peppas N.A., Macromolecules 1993;26:1841.

[70] Yi-Yan N., FelderRM， Koros WJ. J Appl Polym Sci 1980;25:1755.

[71] Crank J.， Park G.S., Diffusion in polymers. New York: Academic Press， 1968.

[72] Coran A.Y.， Boustany K.， Hamed P., J Appl Polym Sci 1971;5:2471.

[73] Waggoner A.R., Blum F.D., MacElroy J.M.D., Macromolecules 1993;26:6841.

[74] Cheever E, Blum F.D., Foster K.R., Mackay R.A., J Colloid Interf Sci 1985;104:121

[75] Mackie J.S., Meares P., Proc R Soc London A 1955;232:498.

[76] Pickup S, Blum F.D., Macromolecules 1989;22:3961.

[77] Ogston A.G, Preston B.N., Wells J.D., Proc R Soc London A 1973;333:297.

[78] Laurent T.C., Pietruszkiewicz A., Persson H., Biochim Biophys Acta 1963;78:351.

[79] Lofroth J.E, Elvingson C., Johansson L., Proc Int Symp Control Rel Bioact Mater 1991;18:146.

[80] Johansson L., Lofroth J.E., J Phys Chem 1993;98:7471.

[81] Cukier R.I., Macromolecules 1984;17:252.

[82] Mel'nichenko Y.B., Klepko V.V., Shilov V.V., Polymer 1993;34:1019.

[83] Klepko V., Mel'nichenko Y., Shilov V., Polym Gels Networks 1996;4:351.

[84] Park I.H., Johnson Jr. C. S, Gabriel D.A., Macromolecules 1990;23:1548.

[85] Rotstein N.A., Lodge T.P., Macromolecules 1992;25:1316.

[86] Won J., Lodge T.P., J Polym Sci: Part B 1993;31:1897.

[87] Jonsson B., Wennerstrom H., Nilsson P.G., Linse P., Colloid Polym Sci 1986;264:77.

[88] Altenberger A.R., Tirrell M., Dahler J.S., J Chem Phys 1986;84:5122.

[89] Phillies G.D.J., Macromolecules 1987;20:558.

[90] Furukawa R., Arauz-Lara J.L., Ware B.R., Macromolecules 1991;24:599.

[91] Uemura Y., McNulty J., Macdonald P.M., Macromolecules 1995;28:4150.

[92] Wheeler L.M., Lodge T.P., Macromolecules 1989;22:3399.

[93] Won J., Oryenemezu C., Miller W., Lodge T.P., Macromolecules 1994;27:7389.

[94] Gao P, Fagerness P.E., Pharm Res 1995;12:955.

[95] Fujita H., Adv Polym Sci 1961;3:1.

[96] Stern S.A., Sampat SR, Kulkarni S.S., J Polym Sci: Polym Phys Ed 1986;24:2149.

[97] Zhu X.X., Wang F., Nivaggioli T., Winnik M.A., Macdonald P.M., Macromolecules 1993;26:6397.

[98] Zhu X.X., Macdonald P.M., Macromolecules 1992;25:4345.

[99] Faldi A., Tirrell M., Lodge T.P., von Meerwall E.D., Macromolecules 1994;27:4184.

[100] Lodge T.P., Lee J.A., Frick T.S., J Polym Sci: Polym Phys Ed 1990;28:2607.

[101] Zielinski J.M., Sillescu H., Romdhane I.H., J Polym Sci: Polym Phys Ed 1996;34:121.

[102] Hang S.U., Duda J.L., J Appl Polym Sci 1997;65:51.

[103] Peppas N.A., Lustig S.R., Hydrogels in medicine and pharmacy, CRC Press, 1987; 57.

[104] Peppas N.A., Reinhart C.T., J Membr Sci 1983;15:275.

[105] Bell C.L., Peppas N.A., Adv Polym Sci: Biopolymers II 1995;122:125.

[106] Mallapragada S.K., Peppas N.A., J Contr Release 1997;45:87.

[107] Am Ende M.T., Peppas N.A., J Contr Release 1997;48:47.

[108] House J. E., Principles of Chemical Kinetics Academci Press. 2007

[109] Grzybowski B.A., Chemistry in Motion, John Wiley & Sons Ltd. 2008.

[110] Ruschau G.R., Yoshikawa S., Newnham R.E. IEEE Electronic Components and Technology Conference, 1992

[111] Du Y., Xue Y., Frisch H.L. Physical Properties of Polymers Handbook, AIP Press, NY 1996

[112] Abboud J.L., Notario R. Pure Appl. Chem. 1999; 71, 645:718.

[113] Ernest W.F., Industrial Solvents Handbook, Noyes Data Corporation, NY 1998

[114] Lee J. Ng., Park C., Whitesides G., Anal. Chem. 2003; 75, 6544-6554

[115] Yang T., Master Thesis, University of Arkansas, 2012

[116] Spearot D., Sudibjo A., Ullal V., Huang A. J. of Eng. Materials and Tech. 2012; 134

[117] Li Y., Tanaka T., J.Chem. Phys. 1990; 92(2), 1365-1371

[118] Colas A., Malczewski R., Ulman K.,http://www.dowcorning.com/content/publishedlit/52-1067-01

[119] Malczewski R., Inman W., http://www.dowcorning.com/content/publishedlit/52-1046-01

[120] Tanaka T., Fillmore J. Chem. Phys. 1979; 70, 3

[121] Li Y., Tanaka T., J. Chem. Phys. 1990; 92, 5

[122] Zrinyi M., Rosta J., Horkay F., Macromolecules 1993; 26, 3097-3102

[123] Chowdhury S., Bhethanaboltla V., Sen R., Microsc. Microanal. 2010; 16, 725-734

Appendix A

Microsoft Lifecam Cinema® digital camera parameters setting

Camera Attributes	Model: Manual
Backlight Compensation	True
Brightness	75
Exposure	0.004
Contrast	0.1
Focus	38
Pan	0
Saturation	0
Sharpness	50
Tile	0
White Balance	3217
Zoom	0

Appendix B

Labview program diagram and interface to automatically capture images of swelling kinetics

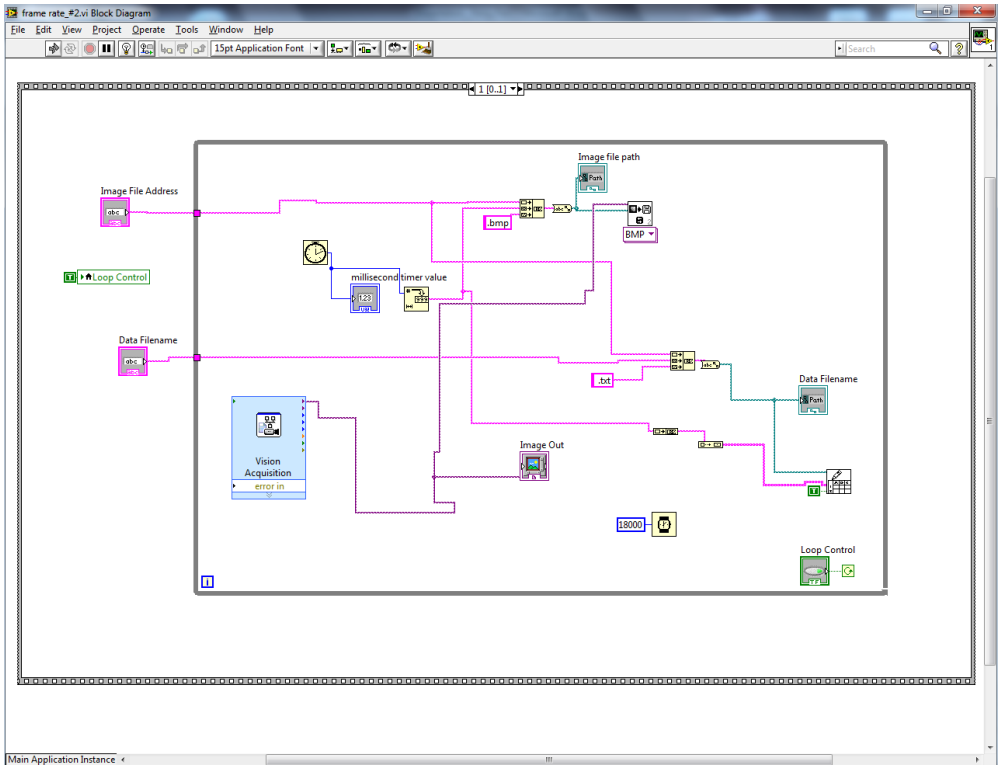

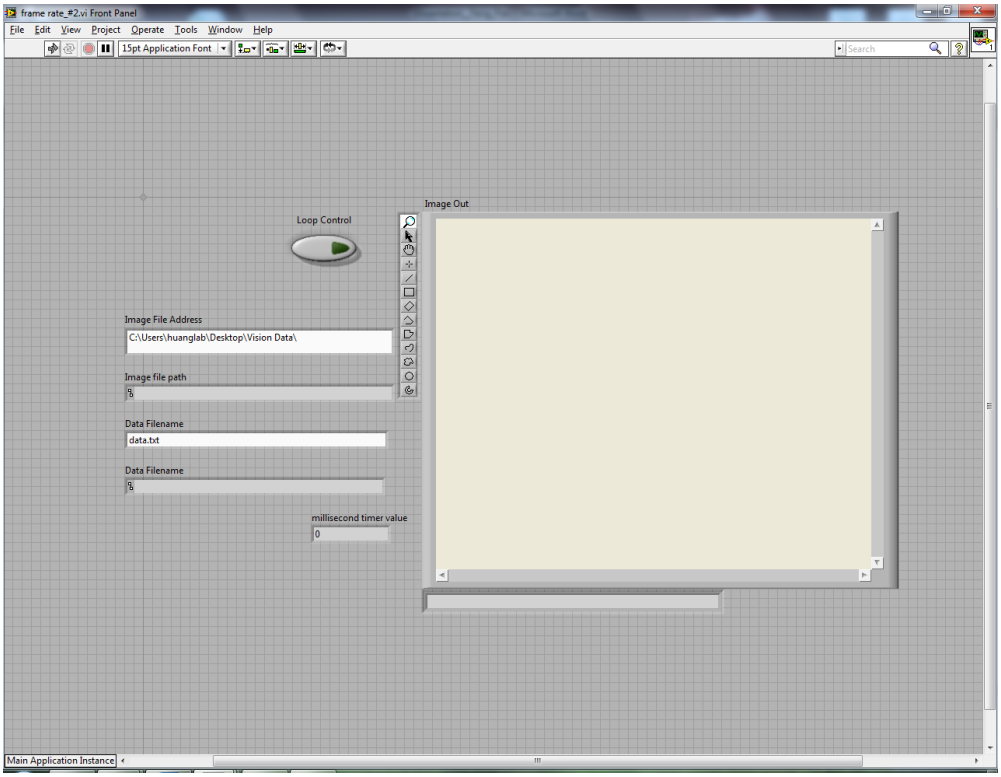

Appendix C

Labview Vision® algorithm and its interface to implement circular edge detection and the measurement of the diameter

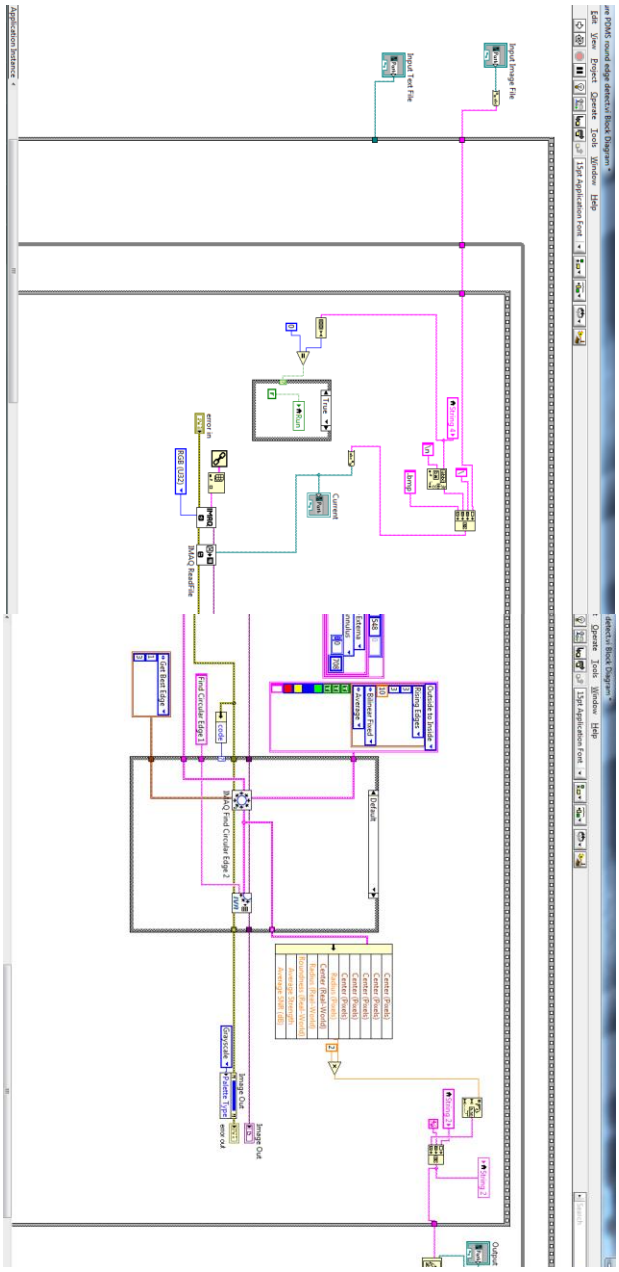

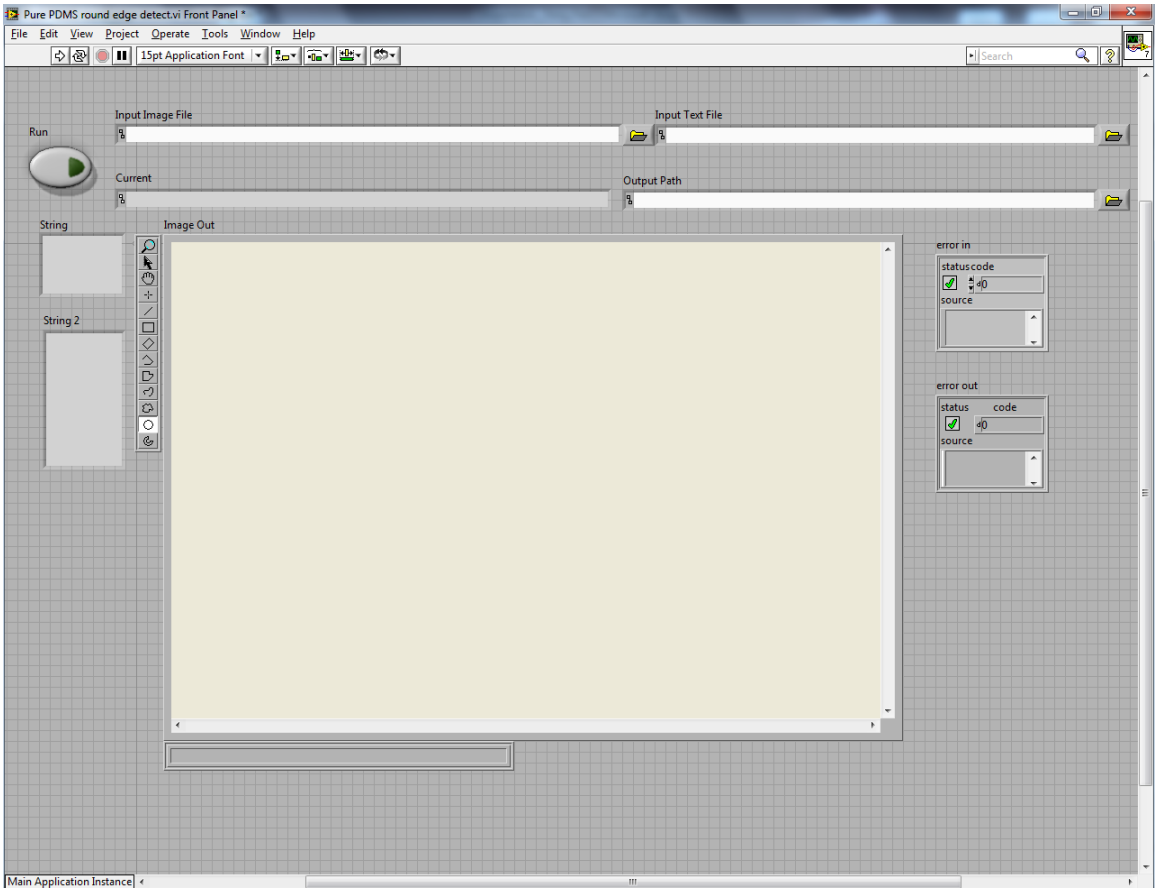
Pure PDMS round edge detect.vi Front Panel *
File Edit View Project Operate Tools Window Help
15pt Application Font
Search
Run
Input Image File
Input Text File
Current
Output Path
String
Image Out
String 2
error in
status code
source
error out
status code
source
Main Application Instance

Appendix D

Metal particle mass percent ratio conversion to volume percent ratio

Particle Mass percent	Mass of PDMS	Mass of Metal	Density ofPDMS	Density of Al	Volume Percent of Al	Density of Cu	Volume Percent of Cu	Density of Fe	Volume Percent of Fe	Density of Ni	Volume Percent of Ni	Density of Staniless steel	Volume Percent of Stainless steel
20%	22	5.5	1.05	2.7	8.86%	8.96	2.85%	7.87	3.23%	8.908	2.86%	8.03	3.17%
40%	22	14.667	1.05	2.7	20.59%	8.96	7.25%	7.87	8.16%	8.908	7.29%	8.03	8.02%
60%	22	33	1.05	2.7	36.84%	8.96	14.95%	7.87	16.67%	8.908	15.02%	8.03	16.40%
70%	22	51.333	1.05	2.7	47.57%	8.96	21.47%	7.87	23.73%	8.908	21.57%	8.03	23.38%
80%	22	88	1.05	2.7	60.87%	8.96	31.91%	7.87	34.79%	8.908	32.04%	8.03	34.34%

Appendix E

Published papers

Feng Pan, Alex Sudibjo, Douglas Spearot and Adam Huang, "*Metal Nano-particle Polymer Composites for MEMS Corrosion Sensing,*" The 6th IEEE International Conference on Nano/Micro Engineered and Molecular Systems, Kaohsiung, Taiwan, February 20-23, 2011

Feng Pan, Adam Huang "*Investigation of Electrochemical Transduction Mechanism of Metal Particle Polymer Composites for the Development of MEMS-based Corrosion Sensor,*" 2009 ASME International Mechanical Engineering Congress and Exposition, Orlando FL, November 13-19, 2009

Feng Pan, Adam Huang, "*Investigation of Oxide-Removal of Nickel and Copper Particles for Fabricating MEMS-Based Corrosion Sensor,*" 2009 ASME International Mechanical Engineering Congress and Exposition, Orlando, FL, November 13-19, 2009

Adam Huang, Feng Pan, Alex Sudibjo and Douglas Spearot, "*Design and Fabrication of the Nano-Particle Composite MEMS Corrosion Sensor,*" 2009 NSF CMMI Research and Innovation Conference, Honolulu, HI, June 22-26, 2009

Feng Pan, Adam Huang, "*Preliminary Investigation of Electrochemical Transduction Mechanism of Metal Particle Polymer Composites for the Development of MEMS-based Corrosion Sensor,*" The fifth international workshop on Advanced Smart Materials and Smart Structures Technology (ANCRiSST), Boston, MA, July 29-August 1, 2009

Feng Pan, John Lee, Alex Di Sciullo Jones and Adam Huang, "*Improved Micro-patterning of Soft-polymers and Elastomers Using Conformally Coated Omni-Coat Nano-films,*" 2008 ASME International Mechanical Engineering Congress and Exposition, Boston, MA, October 31-November 6, 2008